DEVELOPMENT OF A HYDROPHOBICITY CONTROLLED MICROFLUIDIC DISPENSER

LIU HONG

NATIONAL UNIVERSITY OF SINGAPORE

2007

DEVELOPMENT OF A HYDROPHOBICITY CONTROLLED MICROFLUIDIC DISPENSER

LIU HONG
(B.Eng., NEU; M.Eng., NUS)

A THESIS SUBMITTED

FOR THE DEGREE OF DOCTOR OF PHILOSOPHY

DEPARTMENT OF MECHANICAL ENGINEERING

NATIONAL UNIVERSITY OF SINGAPORE

2007

ACKNOWLEDGEMENT

I would like to express my deepest thanks to the following people, without whom this research work and thesis could not have been complete.

First, I would like to thank my supervisor, Professor Andrew Tay A. O. from the Department of Mechanical Engineering, National University of Singapore for his supervision, guidance, encouragement and support throughout this project with his profession skills. I am indebted to Professor Andrew Tay for his valuable comments, suggestions and discussions on research. My appreciation extends to Professor Lim Siak Piang and Professor Shu Chang both from the Department of Mechanical Engineering, National University of Singapore for serving in my thesis committee, giving valuable advices in my qualifying exam and reading the manuscript.

I show my sincere gratitude to my co-supervisor, Dr. Saman Dharmatilleke from the Institute of Materials Research and Engineering who recruited, trained, guided and supported me with his rich research experiences. He is an outstanding example of a research scientist who always takes a new exploration for innovation with enthusiasm. He has always challenged me to be creative and earnest since I joined the institute.

In addition, I would like to acknowledge the contribution of my colleague Mr. Devendra Kumar Maurya for his help on device fabricating and testing, and valuable technical discussions. I also thank Institute of Materials Research and Engineering for offering world-class facilities and working environment for me to carry out this project.

Finally, but not least, I would like to thank my family members for their great patience and encouragement through this process. The births of my sons, Chuyue and Chufang, have given me a lot of joys and energized me to complete this project.

TABLE OF CONTENTS

SUMMARY

The traditional micropumps faced limitations like high power consumption and high driving force in the attempt for implementation as remote environmental monitoring systems, implantable medical devices or chemical analysis systems. This project aimed to develop a product-oriented microfluidic device with the possible commercialization in mind and can be integrated into a lab-on-a-chip performing specific chemical analysis, clinical diagnostic and environmental morning.

In this project, a novel microfluidic dispensing device based on electrowetting-on-dielectric (EWOD) was proposed and implemented. The physics of this EWOD device was based on the fluid dynamics illustrated by Navier-Stokes equation. Its performance heavily depends on dielectric or insulation layer properties rather than that of fluid or electrode. Theoretically, there are no dielectric materials of both high dielectric strength and high dielectric constant, and compromise is often necessary to meet the practical requirements. The dielectric breakdown analysis demonstrated that $35°$ of contact angle variation of Cytop™ could be achieved at as low as 65 V to actuate EWOD, which is reported to be the most suitable material for EWOD. Good reversibility of Cytop™ based on the contact angle measurement result indicated that EWOD performance can be greatly improved by incorporating it in the device. The results of contact angle measurement are in good agreement with the theoretical prediction by Young-Lippmann equation and the results from other researchers.

The governing equation with respect to the redistribution of the surface charge density is presented to demonstrate the hydrodynamics of liquid-solid interfacial tension. Upon applying the voltage potentials, a free charge distribution is built-up at the liquid-solid interface to generate an electrostatic force to pull the liquid column

forward. The interfacial charge density accounts for the generation of the non-uniform electric field and potential distribution. The surface charge and electric field distribution models were modeled and simulated using FlexPDE 5.

Consequently, the electrostatic force resulted from the redistribution of the free surface charges induced by the non-uniform electrical field was modeled to show its dependence of the magnitude and direction on the electric field distribution as a geometrical function of the liquid. It can be decomposed into a horizontal component and a vertical component. The horizontal electrostatic force was independent of contact angle while the vertical component increased inversely with contact angle. It potentially provides a new contribution to explain contact angle saturation phenomenon. The obtained expression of horizontal force is identical to the results achieved by other researchers using different methods.

Based on the above analysis, a new hydrodynamic mathematical model of the time-averaged liquid column velocity governed by the Navier-Stokes equation was developed, which agreed well with the experimental data. The electrostatic force, which affected the dependence factor $f\ (\cos\theta)$, was considered as a function of the average flow rate. The conceptual design and working principle of the microfluidic dispenser were demonstrated and successfully verified by a proof-of-concept device. The proposed hydrophobicity-controlled microfluidic dispenser was fabricated using MEMS technology and tested to evaluate its feasibility and applicability in environmental morning and biomedical systems. The fluid flow can be electrically actuated to propagate at a flow rate of 18 nl/min under a voltage of as low as 20 V. A proper device design significantly minimized the evaporation effect. It has an inbuilt metering feature to dispense a measured volume of liquid in the range of sub nano liters without a dedicated sensor. The low power consumption and the low voltage

made it very attractive for applications which required an ultra miniature metering microfluidic device.

A PCT patent application with respect to this technology was filed and published on November 2, 2006 with an international publication no. WO 2006/115464 A1.

LIST OF TABLES

LIST OF FIGURES

NOMENCLATURE

Symbols	Interpretation
γ	- surface tension
γ_{lv}, γ_{sl} and γ_{sv}	- surface tension at liquid-vapor, solid-liquid and solid-vapor interface
γ_{sl}^{el}, γ_{sl}^{ch}	- electrical and chemical component of γ_{sl}
θ	- contact angle
θ_0	- contact angle without applying voltage
$\Delta\theta$	- contact angle variation
Δp	- the pressure difference across the interface
R_1, R_2	- the two principle radii of curvature of sessile drop
R	- droplet radius
Ra	- the surface roughness of substrate
Re	- Reynolds number
Ca	- Capillary number
Bo	- Bond number
We	- Weber number
ρ	- fluid density
v	- fluid mean velocity
μ	- dynamic fluid viscosity
L	- characteristic length of fluid field
D_h	- hydraulic diameter

g	- acceleration due to gravity
C	- capacitance of the solid-liquid interface
d	- thickness of dielectric layer
d_{min}	- minimum dielectric thickness
d_{max}	- maximum dielectric thickness under a constant voltage to actuate electrowetting
ε	- dielectric constant of insulator
ε_0	- vacuum permittivity
V	- applied voltage
V_{bd}	- dielectric breakdown voltage
V_{ew}	- voltage required to actuate electrowetting
E_{ds}	- dielectric strength
E	- electrical field
E_{sm}	- electrical field in surrounding medium
P_m	- the internal fluid pressure acting on the meniscus
P_a	- pressure from the surround medium (atmosphere pressure)
f	- contributions from material properties of substrate and fluid
W	- width of microchannel
H	- height of microchannel
S	- the average displacement of liquid column along x axis
e	- the elementary charge
z^k	- the valence of the kth species
n^k	- the concentration of the kth species
ρ_s	- surface charge density
ρ_0	- the charge density at the liquid-solid (dielectric) interface far from the three-phase contact line

$\vec{n}$	- the unit normal vector of the interface pointing towards air
σ	- conductivity
A	- the interfacial area
T	- Maxwell stress tensor / temperature
δ_{ij}	- the Kronecker delta
F_{el}	- electrostatic force
F_{ex}, F_{ey}	- the horizontal and vertical component F_{el}
ω	- the complex coordinates of the transformed plane
τ, υ	- transformed coordinates
α	- $\alpha=1-\theta/\pi$
R_{el}	- resistance of electrical wires
R_{water}	- resistance of water
R_{Au}	- resistance of gold pads
R_{total}	- total resistance of the electrical model
C_t	- the instantaneous capacitance
P	- the instantaneous power
P_{res}	- the total dissipated energy
N	- the numbers of sample data taken from the experiment
σ_{sd}	- the standard deviation
s_i	- the shortest distance between any experimental point and the simulated model
$\bar{s}$	- the mean of the summation of the shortest distances between the experimental points and the simulated model

CHAPTER 1

INTRODUCTION

1.1 Microfluidics Background

Microfluidics is the general research headline for enormous research projects focused on development of miniaturized devices, systems and innovative applications for fluidic (liquid and gases) manipulation in microscale. Microfluidics has now been internationally recognized as having potential towards widespread applications such as environmental monitoring, clinical diagnostics, civil defence and flow control. It has been strongly evidenced by the significant growth of publications in leading microfluidics journals and patents issued in the US since the last decade [1]. The distinctive emergence and remarkable growth of micro-electro-mechanical-systems (MEMS) technology in the past twenty five years, has enabled us to handle small amounts of fluid in the range of nano or even pico liters [2, 3, 4, 5]. Therefore, nano/microfluidics could be the link between the micro and nano sciences and technologies [6].

Among all the applications, a lot of research interests in microfluidics have been greatly motivated by biomedical applications. The ultimate goal of microfluidic devices and systems in these applications is a "lab-on-a-chip", which was first conceptually illustrated by Burns *et al*. (1998), to incorporate multiple aspects of

modern biology and chemistry laboratories in a single microchip. The microchip performance crucially depends on fast automatic manipulation of small quantities of liquids. Researchers have presented various processes used for clinical diagnostics on single-function biochips, such as capillary electrophoresis (CE) for DNA separation [7, 8, 9] and sequencing [10, 11, 12], DNA amplification with polymer chain reaction (PCR) [13, 14], cell lysis [15, 16, 17], diffusion-based separation [18, 19], chaotic mixer [20, 21] and DNA sensing [22, 23].   Numerous microfluidic components including pumps [24-32], valves [33-38], channels [39-42], mixers [43-47], sensors [48-51], actuators [52-59], reaction chambers [60, 61], detectors [62-64] and dispensers [65-67] have been demonstrated to be integrated in biochips in recent years.

The miniaturization of lab-on-a-chip systems offers a number of advantages, such as reduced sample size, decreased assay time, minimized reagent cost, increased automation level and sensitivity, enhanced safety, and improved portability and disposability. Some bio-assays and DNA microarrays based on MEMS /microfluidic technology have been developed with different targets and applications, which is summarized in Table 1.1 [68].

Microfluidic flow control has been thoroughly studied with emphasis on topics of fundamental interest for investigation of fluid motion and transportation processes. Many kinds of external fields, such as pressure, electric, magnetic capillary, thermal, and so on) can be utilized to manipulate fluid in microscale, which is different from the macroworld. As objects shrink, the ratio of surface area to volume increases rendering surface forces more important than gravitational, viscous, and inertial forces. The fluid manipulations can be realized through fields either applied macroscopically, e.g., at the inlets, outlets and chambers, or locally generated along the fluid paths (microchannel, cavity, etc.) by integrated components (electrodes, insulation layer, etc.).

Table 1.1. Microfluidic devices in biological applications.

Applications	Targets	Functions
Macromolecular Analysis	DNA Analysis	Mostly involving PCR, mixing DNA and a restriction enzyme, separation of fragments, sample preparation, performing biochemical reactions [69-85].
	Enzyme Assays	Determination of an enzyme's reaction kinetics, measurement of activities of liver transaminases, protein extraction and detection via diffusion [86-91].
	Immunoassays	High-throughput screening; antigen /antibody quantization and trapping and releasing materials on surfaces [92-104].
Cellular Analysis	Cytometry	Sorting, analyzing and counting cells with improved sensitivity, accuracy and less cost [105-114].
	Cell-based Assays	Cell-based high throughput assays [107, 114, 115].
	Cellular Biosensors	Sensors for environmental monitoring, toxic detection and physiological monitoring, cell-cartridge for sample analysis [116-119].
	Culturing	Creating cell-cell, cell-substrate and cell-medium interactions [120-124].

Table 1.2 summarizes and categorizes the frequently investigated driving forces and fields based on their mechanisms to manipulate microfluidic flow, which were reported in prestigious publications in recent years.

To summarize, many means have been studied and used to control flows. External fields can induce motion of objects embedded with fluids, or the channel walls can be systematically distorted to move the fluids. Magnetic fields can affect fluids directly or manipulate dispersive magnetic particles. Sound fields are able to create acoustic streaming movement. Thermo effects can generate periodical deformation of a membrane by temperature gradient to induce peristaltic pumping. Electric fields can manipulate flows in a variety of ways: the fluid is driven by viscous forces induced by an electrical double layer (EDL) which is relatively stationary along

the charged boundaries (electroosmosis); a two-fluid interface or a particle surrounded by viscous and incompressible ambient fluid can be moved in an electric field gradient (dielectrophoresis); a liquid can be driven by the surface tension which is modified with electric field change. For each manner of fluid flow, surface properties of fluid paths should also be investigated to provide additional control. Surface tension, related to both material properties and external fields, has been proven to be a dominant force in microscale fluid flow and the details will be discussed in the next section.

Table 1.2. Forces and external fields utilized to manipulate microfluidic flows.

Forces / Fields	Mechanisms	Remarks / Literatures
Mechanical Forces	Centrifugal force	Results from spinning disk [125-127]
	Pressure difference	Generated by actuators [128-131]
Sound Wave	Acoustic streaming	Induced by mechanical traveling wave [132-134]
Surface Tension Forces	Thermocapillary	Capillary pressure difference caused by induced-heat (temperature gradient) [135-138].
	Electrowetting	Surface tension changes / gradients [139-142].
	Electrochemical	Surface tension gradient [143-144].
	Optoelectrowetting	Pressure difference caused by the impedance change of the photoconductive layer upon illumination of light [145].
Electric Fields	Electroosmosis	External electrical field induces the movement of electrical double layer (EDL), uniform velocity profile [146-149].
	Dielectrophoresis	Forces originate from the polarization of fluid. The force density composes of a force density that arises from the non-uniformity of the material properties and a force density that can be combined with the hydrodynamic pressure [150-152].
	Electrohydrodynamic (EHD)	Electrostatic forces acting on dielectric fluids [153-157].
Magnetic Fields	Magnetohydrodynamic (MHD)	Lorentz force is generated by current-carrying ions in aqueous solutions subjected to a magnetic field to exert on the liquid and induce flow [158-161].

1.2   Microscale Surface Tension

1.2.1 Surface Tension at Microscale

The gravity and inertia effects dominate our behaviour in the physical world. However, phenomena such as viscosity, surface tension and diffusion become more significant when systems are reduced in size (length, area and volume). They are able to dominate and lead to a world at micrometer scale, which operates much differently from the macroscopic one we perceive and live in [162]. The scaling issues of various types of forces in the micro domain were systematically compared by Trimmer [163]. Based on his work, as system dimensions scale down in size, magnetic force scales down with second to fourth power; electrostatic force scales down with first to second power depending upon how electric field varying with size; pneumatic and hydraulic forces caused by pressures and biological (muscle) forces proportional to muscle cross-section scale down with second power; surface tension amazingly scales to first power because it only depends on the length of interface. It shows that surface tension becomes dominant over most other forces in microscale.

In physics, surface tension is represented by the symbol γ and is defined as the force along a line of unit length where the force is parallel to the surface but perpendicular to the line. Surface tension is therefore measured in newton per meter ($N \cdot m^{-1}$), although the centimeter gram second system of units of dyne per cm is normally used.

Surface tension is caused by various intermolecular forces between the liquid molecules. In the bulk of liquid, each molecule which has specific potential energy is pulled equally in all directions by surrounding liquid molecules, resulting in a net force of zero and a minimum potential energy. At the surface of liquid, the molecules are pulled inwards by other molecules deeper inside the liquid because of the unbalancing

attractive forces from the surrounding medium (be it vacuum, air or another liquid). The potential energy reaches its maximum at the surface. Therefore, all of the molecules at the surface are subject to an inward force of molecular attraction which can be balanced only by the resistance of the liquid to compression, shown in Figure 1.1. Thus, liquids will tend to minimize this surface energy by minimizing interfacial area and taking on a spherical shape in absence of external forces. Typical surface tension values for some liquids and solids in air at room temperature are given in Table 1.3.
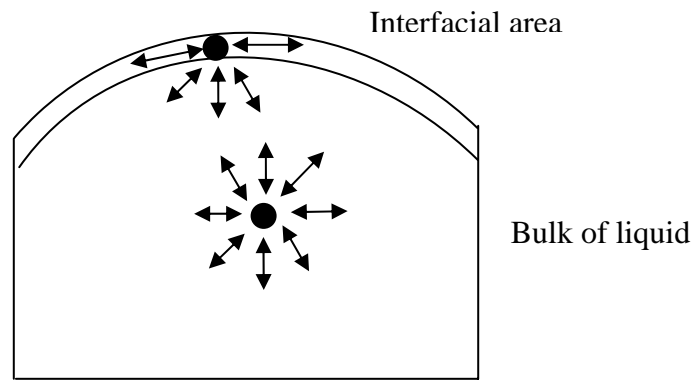
Fig. 1.1. Diagram of attractive forces on liquid molecules.

Table 1.3. Typical surface tension values of materials in air. Adapted from [163].

Materials	Water	NaCl	Methanol	Ethanol	Mercury
γ(mN/m)	72.94	72—78.754	22.50	22.39	486.5
Materials	Polydimethyl-siloxame (PDMS)	Self-assembled Monolayer (SAM)	Parylene C	SU8 Photoresist	Cytop™ Copolymer
γ(mN/m)	51	20.3 [164]	70.6 [165]	45.5 [166]	19 [167]

When a liquid droplet rests on a non-wetting solid surface, the forces at the three-phase interfaces (solid liquid and vapour) reach equilibrium without consideration of gravity, which is shown in Figure 1.2. The forces at solid-liquid-vapour interface are illustrated by Young's equation on his essay published in 1805 [168]

$$\cos\theta = \frac{\gamma_{sv} - \gamma_{sl}}{\gamma_{lv}} \tag{1.1}$$

in which the interfacial energies are interpreted as surface tensions pulling on the three-phase contact line, where γ_{lv}, γ_{sl} and γ_{sv} are the liquid-vapour, solid-liquid and solid-vapour surface energies respectively. θ is the equilibrium contact angle without externally applied electrical potential. Note that the horizontal component of forces is balanced at the three-phase contact line while the vertical component is balanced out by normal stresses in the solid surface.
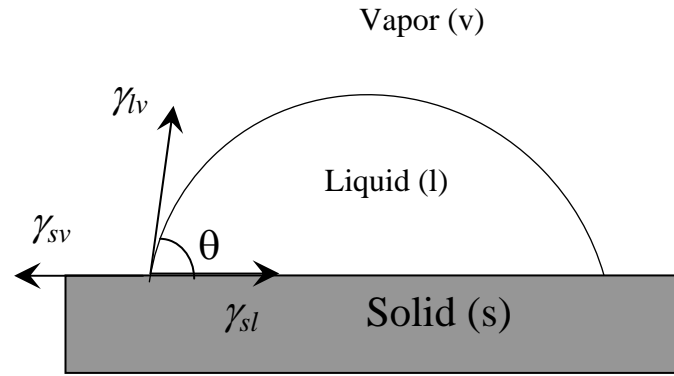
Fig. 1.2. Force equilibrium at the contact line of sessile drop.

Using Laplace equation, a simple geometrical derivation of the equation for a surface having two radii of curvature was provided by Adam [169] in his well known book on surface chemistry in the well known form:

$$\Delta p = \gamma_{lv}\left(\frac{1}{R_1} + \frac{1}{R_2}\right) \tag{1.2}$$

where R_1 and R_2 are the two principle radii of curvature of surface and Δp is the pressure difference across the interface. It states Δp is a constant, independent of the position of the interface. This pressure difference is balanced by the hydrostatic pressure at the surface. In Figure 1.3, *ABCD* is a small part of the surface of a liquid droplet resting on a solid surface (referring to Figure 1.2), with sides at right angles.

The normals of *A* and *B* meet at O_1 and those at *B* and *C* at O_2. Hence, the principle radius of curvature of the arc *AB* is R_1 and that of *BC* is R_2.
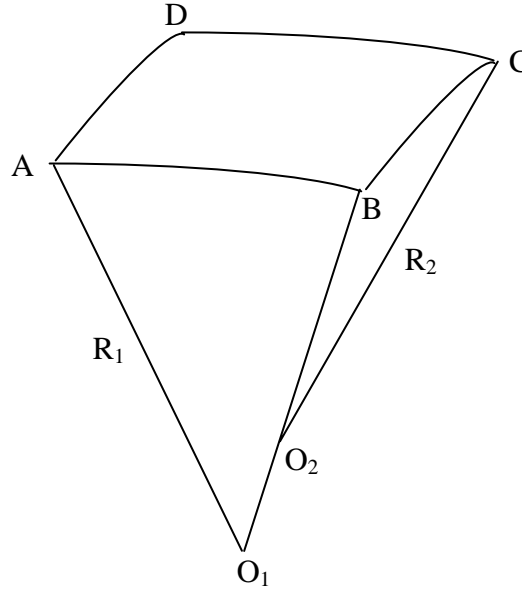
Fig. 1.3. The schematic of two principle radii of a liquid droplet surface.

For homogeneous substrates, it means that droplets form a spherical cap shape at equilibrium. Thus, for the surface of a sphere, it becomes

$$\Delta p = \frac{2\gamma_{lv}}{R} \tag{1.3}$$

From Equation 1.2, the pressure difference becomes large as the radius of curvature reduces. For example, the pressure drop at the interface of a water drop with radius of 1 μm would be 1.42 atm. Therefore, researchers should be aware of limitation of liquid droplet generation and handling for systems design because it will be difficult or even impossible to manipulate liquid droplets with the size of less than sub-micrometers.

1.2.2 Surface Tension Control

Actuation of fluid motion by surface tension needs approaches to actively control the interfacial energies in the system. Generally, the approaches of manipulation of interfacial energies should be realized real-time, reversibly, rapidly and inexpensively via an easily-handled physical variable, such as incident light intensity, electric field or

voltage. The recent development of the chemical, thermal and electrical methods was reviewed by Craig Rosslee *et al*. (2000) [170].

Chemical Methods

B. S. Gallardo *et al*. (1999) [143] reported an electrochemical method in which redox-active surfactants were used to manipulate the surface tension gradient. A moderate velocity of 2.5 mm/s was obtained at about 0.4 V. This method avoids using moving part and permits vectorial transport and positioning of materials on unconfined surfaces at low voltages (<1 V). However, since the electrochemically established gradient depends on the length of the fluid channel, this method does not offer a convenient way to control multiple droplets independently.

Opto- Methods

A photochemical method has been demonstrated by Ichimura *et al*. (2000) [171] to generate surface energy gradients for driving liquid motions through asymmetrical irradiation of a photoisomerizable azobenzene surface with blue light. The employment of light offers a convenient way to control two-dimensional movement of multiple droplets without using micromachined structures or devices. However, the limitation of hysteresis and photoinduced changes in contact angle can prohibit notably transportation of many liquids. And the obtained typical speed of 35 μm/s for the motion of a 2-μl olive oil droplet is very slow for chemical process systems.

Thermal Methods

The thermocapillary effect has been studied in detail [135, 172] and employed to transport liquids, which so far has achieved more promising results than chemical methods. By manipulating the surface tension on one side of a liquid drop through a temperature gradient across both ends of liquid droplets, a pressure difference can be generated for liquid motion. This pressure difference can be produced by heating one

drop interface because surface tension decreases linearly with meniscus temperature. However, the complexity of these systems results in many uncertain issues for design and analysis of a number of factors such as materials properties, structure geometry, fluid property and velocity. The temperature variations across the droplets are unacceptable for many potential biological applications where precise thermal control of 1°C accuracy or finer is normal required.

Electrical Methods

Electrical control of surface tension at interfaces between two liquids was first systematically studied in 1875 by Gabriel Lippmann [173], who first described it "Electrocapillarity". He demonstrated electrocapillary effect whereby capillary depression of mercury column in contact with electrolyte solutions could be varied by applying a voltage between the mercury and electrolyte. Based on his experiments, he not only formulated electrocapillary theory but also developed several applications including a very sensitive capillary electrometer and a motor. However, this classical electrocapillary effect strongly depends on the state of electric double-layer (EDL) at the interface which is sensitive to both the type and concentration of electrolyte in the aqueous phase.

1.3 Dimensionless Numbers in Microfluidics

A lot of physical phenomena have been involved in microfluidic systems and devices. Dimensionless numbers demonstrate the ratios of these phenomena encountered in fluids dynamics to understand complicated fluid behavior. The forces of interest include surface tension, pressure, inertia, viscosity and gravity. The dimensionless numbers yielded by the ratios between any two of these forces provide qualitative characterizations of fluid behaviors, which are summarized in Table 1.4.

Table 1.4. Dimensionless numbers for microfluidic analysis.

Abbreviation	Group	Definition	Interpretation
Re	Reynolds number	$\dfrac{2R\rho v}{\mu}$	inertial/viscous
Ca	Capillary number	$\dfrac{\mu v}{\gamma}$	viscous/surface tension
Bo	Bond number	$\dfrac{\rho g R^2}{\gamma}$	Gravity/surface tension
We	Weber number	$\dfrac{\rho R v^2}{\gamma}$	Inertial/surface tension

Of all dimensionless numbers, the **Reynolds number** (Re) is the most important dimensionless number in fluid dynamics and defined as the ratio of inertial forces to viscous forces. In its definition, ρ and v are the fluid density and mean velocity, μ is dynamic fluid viscosity and $2R$ (cross-section is circular with a radius of R) is a characteristic length (L) of fluid field. It provides a criterion to determine whether a flow pattern is laminar or turbulent. The standard transition from laminar to turbulent flow normally occurs for Re between 2000 and 3000. As Re increases, it results in unpredictable, irregular turbulent flow.

However, it was argued by P. Gravesen et $al.$ [174] that the Reynolds number may not be useful for complete determination of flow pattern because the length L is often shorter than the entrance length for fully developed flow in many microfluidic devices. Thus, Gravesen suggested that L should be determined depending upon the ratio of L to the hydraulic diameter D_h. For small ratios of L/D_h, the value for a sharp-edged slit-type orifice is used [175]. When the ratio is less than 70, the transitional Reynolds number should be defined by setting L equal to the entrance length for fully developed flow, which is approximately 30 L/D_h. With larger ratios (>70), the Reynolds number is generally accepted to be 2300.

Another dimensionless number is the **Capillary number** represented by a ratio of viscous forces and surface tension forces acting across an interface between two immiscible liquids, which is given in Table 1.4. The capillary number is important to characterize the contact line moving speed during the wetting or dewetting processes because it determines the free surface shape near the contact line. Assume a water drop with a velocity of 100 μm/s, Ca is approximately 10^{-6}, which shows that surface tension effect should determine the dynamics of contact line movement rather than viscous force in microfluidics.

The **Bond number** measures the strength of gravity with respect to surface tension and is given in Table 1.4, where g is the acceleration due to gravity and R is the length scale (typically the radius of a drop or the radius of a capillary tube). In most applications of microfluidics, the droplets with a typical size of the order of 1mm or less. The ambient medium can be either air or another immiscible liquid (normally an oil). Thus, Bo is usually less than 10^{-1} which indicates surface tension dominates the droplet shape rather than gravity. Therefore gravity is negligible throughout the rest of this thesis for considerations. Let's consider an ideal sphere water droplet, the gravitation force is represented by $4/3\pi\rho gR^3$, here, R is the droplet radius. The graphically comparison of surface tension and gravitational effect on this spherical water droplet is demonstrated in Figure 1.4.

The **Weber number** is a dimensionless number which is the ratio of inertia forces to surface forces in fluid mechanics. The Weber number is useful in analyzing fluid flows especially for multiphase flows with strongly curved surfaces such as droplets and bubbles. When $We > 12$, droplets become unstable and transform into thin layer on die surface or even disperse into smaller drops with higher values. Assume a water droplet with $V=1$ cm/s and $R=1$ mm, We is approximately 10^{-3}. It indicates that

only inertial stress should not cause dispersive droplets. More detailed review of the dimensionless numbers in fluid mechanics is given by T. M. Squires and S. R. Quake (2005) [176].
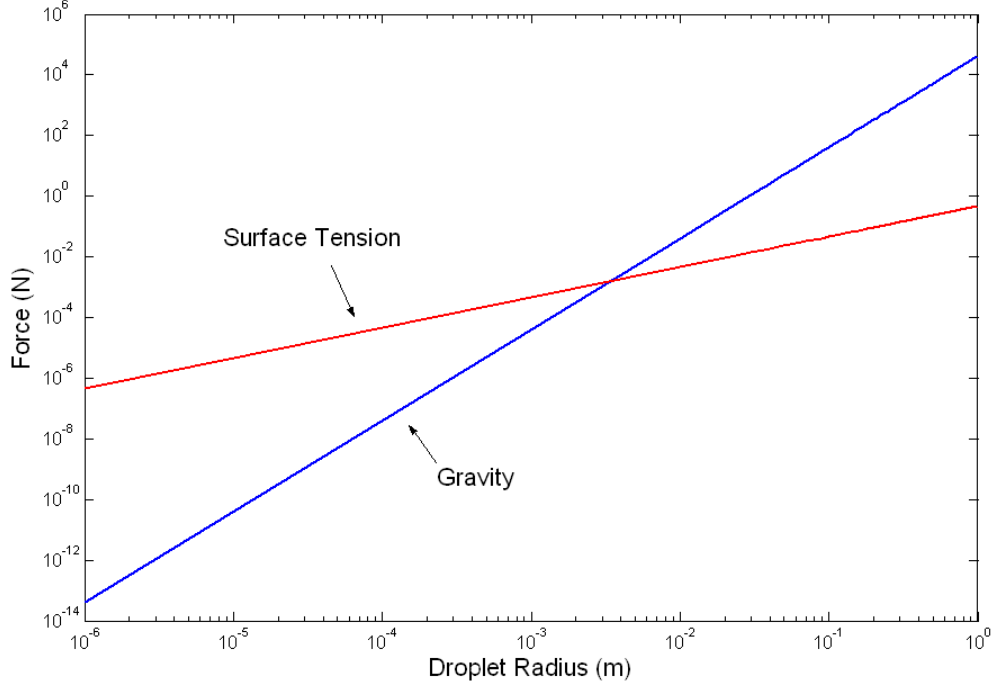
Fig.1.4. Microscale comparison of surface tension and gravity
acting on a spherical water droplet.

1.4 Micropump Technologies Review

The function of the presented microfluidic dispenser in this study, such as delivering controllable fluid flow, is similar to that of micropumps. Moreover, the mechanism of the presented microfluidic dispenser, i.e. electrowetting-on-dielectric (EWOD), is also utilized in micropump technology. Therefore, a literature review was carried out on micropump technologies.

The micropump is one of the components in a microfluidic system to supply a steady controllable fluid flow in the range from nano or micro liter to milli liter per

minute. There is a greatly growing market for the treatment of some diseases which need the micro dosing system [1]. Thus, in the microscale, it is an important and critical task to control and transport the fluid amount using different mechanisms such as the electrohydrodynamic effect, electrochemical effect and the electrowetting effect comparing to the macro scale previously.

Several papers have comprehensively reviewed micropumps and technologies. Peter Gravesen and Jens Branebjerg et al. overviewed the fluid mechanics modeling and devices in the microscale, such as valves and micropumps [174]. R. Zengerle and H. Sandmaier introduced recent developments in microfluidics and several types of micropumps [177]. N. T. Nguyen et al. systematically outlined pump principles and realization and graphically compared specifications such as feature size, flow rate and backpressure [178]. They categorized micropumps based on their work principles and discussed their merits and demerits for different applications. The most recent review was presented by D. J. Laser and J. G. Santiago [179] who have extensively studied Reciprocating and aperiodic displacement micropumps, electroosmotic and dynamic micropumps over past 25 years. They also indicated that micropumps suitable for important applications such as space exploration and chemical and biological analysis are not available yet.

Compared to other MEMS devices such as flow sensors, valves et al., micropumps use a much greater variety of operating principles. Usually, the micropumps can be categorized into mechanical pumps and non-mechanical pumps based on their working principles [180], as shown in Figure 1.5.
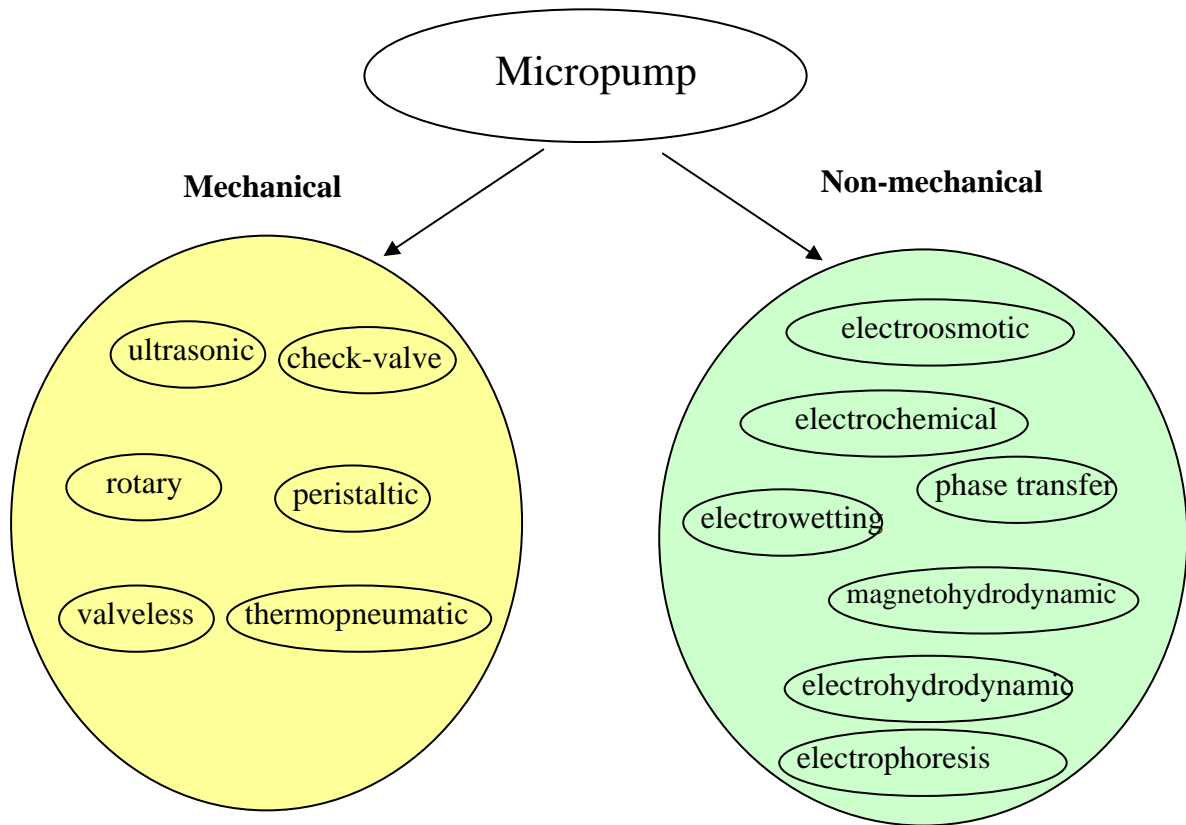
Fig. 1.5. Micropump categories.

Mechanical pumps utilize moving parts such as check valves, oscillating membranes or turbines for delivering a constant fluid volume in each pump cycle, which is mostly used in macro scale pumps and its output is large and size relatively big. The detailed review of the mechanical micropumps can be referred to the literatures mentioned above. In this thesis, it will focus on the review of non-mechanical micropumps.

Non-mechanical pumps normally add momentum to the fluid for pumping effect by converting other energy forms into kinetic energy. Its output is usually in the micro scale. In contrast to mechanical micropumps, most of non-mechanical micropumps are very competitive, having unique properties in microscale applications. For example, electrokinetic pumps (including electrophoresis and electroosmotic) are able to achieve high efficiency via a high electric field gradient. However, a

surprisingly large voltage should be applied to achieve a high electric field gradient in a macroscopic fluid system. It consumes a lot of power and can induce undesirable electrochemical reactions, i.e., electrolysis between fluids and electrodes. Another example is to employ surface tension to pump fluids, which is impossible to realize in macroscale by mechanical pumps.

One attractive non-mechanical micropump is the **electrohydrodynamic** (**EHD**) **pump** relying on the interaction of electrostatic forces with ions of dielectric fluids. The EHD pumping is based on electrostatic forces acting on dielectric fluids: the one based on the interaction between the conductivity gradient and the traveling wave of potential is called EHD induction pump; the one based on the Coulomb force acting on ions injected from one or both emitter electrodes into fluids by means of electrochemical reaction is called EHD injection pump. The principles of the EHD pumps are schematically shown in Figure 1.6 [180]. Here, E is the electrical field, ε is the fluid permittivity and γ is the surface tension.
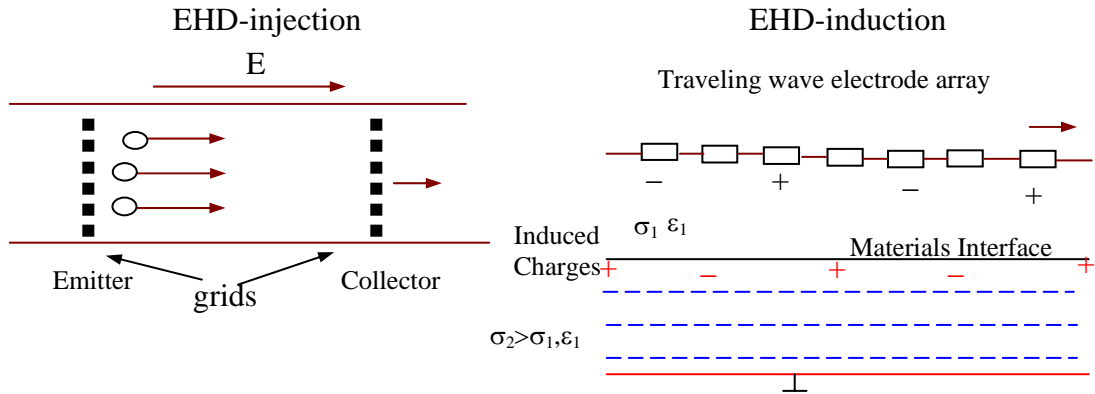
Fig. 1.6. Principles of EHD pumps [180]:
(a) EHD injection pump; (b) EHD induction pump.

Bart *et al*. [153] firstly reported the EHD induction micropump followed by Richter A. *et al*. [156-7, 181-2], Fuhr *et al*. [30, 154], Furuya, A, *et al*. [183] and Ahn

at al. [155]. Their designs are quite similar and the specifications are compared in Table 1.5.

Table 1.5. Typical parameters of EHD micropumps.

Authors	Bart *et al.* [153]	Richter *et al.* [156-7, 181-2]	Fuhr *et al.* [30, 154]	Furuya *et al.* [183]	Ahn *et al.* [155]
Typical Size (μm)	500	3000	600	400	3000
Chamber Height (μm)	-	-	50	100	200
Max Flow Rate (μl/min)	-	15000	0.45	0.12	50
Max Back Pressure (Pa)	-	500	-	-	220
Principle	EHD-induction	EHD-injection	EHD-induction	EHD-injection	EHD-injection
Fabrication Technology	Bulk	Bulk	Bulk	Bulk	Bulk
Year	1990	1990-1991	1992, 1997	1996	1998

The pumping principle of a **magnetohydrodynamic (MHD) micropump** depends on Lorentz force acting on conductive solution to create a pressure gradient to pump liquid. The Lorentz force is generated by current-carrying ions in conductive solutions subjecting to a magnetic field to induce fluid flow.

Figure 1.7 shows the actuation principle of a typical MHD micropump presented by Jang and Lee [158], where J is current density and B is magnetic flux density. This Lorentz force is produced when an electric current is applied across a channel filled with conducting solution in the presence of a perpendicular magnetic field. The Lorentz force is both perpendicular to the current in the channel and the magnetic field. The fabricated device consists of a 40 mm-long channel with a cross section of 1 mm width and 0.4 mm height, a pair of aluminum electrodes and two permanent magnets. With a magnet flux density of 0.44 T, the maximum flow rate was measured at 63 μl/min with 1.8 mA and a pressure difference between inlet and outlet at about 180 Pa

with 10 mA using seawater as medium. Several papers [159-161] have presented applications of MHD micropumps driven by AC or DC potentials respectively. Although MHD pumps have the abilities of bidirectional pumping and biocompatibility, its two performance factors including magnetic flux density and current density may result in miniaturization difficulty for permanent magnets and thermal effect.
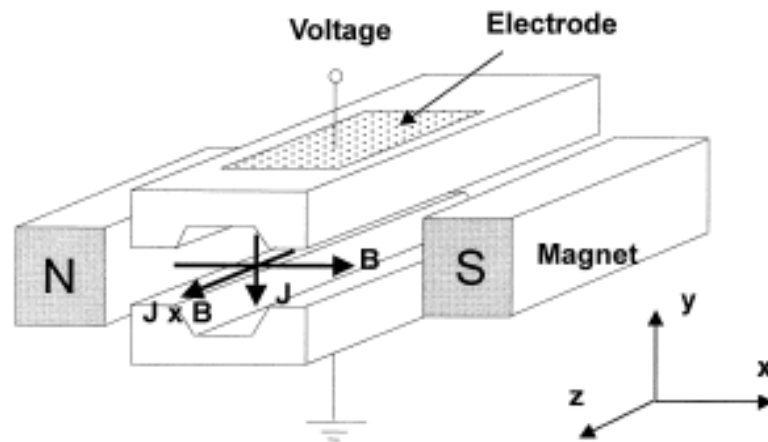
Fig. 1.7. The actuation principle of MHD pump driven by Lorentz force [158].

Electroosmotic (EO) pumping effect results from an electrified fluid under the application of an external electric field. Chemical reactions make the channel wall surface charged and counter ions accumulate at the vicinity of the charged surface to form an electric double layer of a typical thickness of the order of several nanometers. An applied external electric field forces the EDL layer to move, which also attracts opposite ions in the solution. Thus, the fluid in the channel will be pushed because of the viscous force. The pumping principle is illustrated in Figure 1.8 [179] and the physics of it is discussed in detail by R. F. Probstein [184].

(a)

(b)
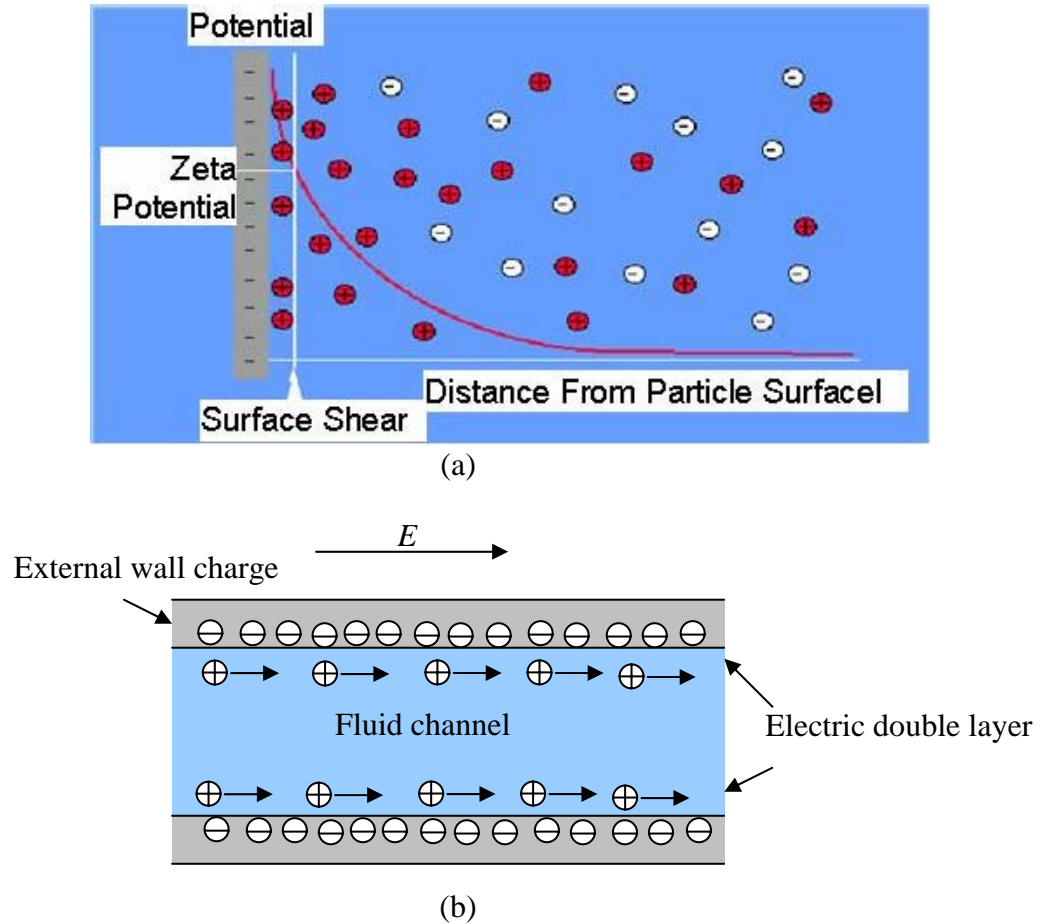
Fig. 1.8. Electrochemistry of electrical double layer at the solid-liquid interface and electroosmotic principle [179]. (a) Counter ions accumulate in the vicinity of charged surface due to chemical reaction to form EDL layer. (b) An external electric field causes EDL layer to move, which consequently drag the fluid in channel via viscous force.

Electroosmotic techniques and processes have been investigated for incorporation into microsystems for chemical and biological analysis applications including flow injection analysis [185], on-chip electrophoretic separation [186-7] and on-chip chromatography [188]. Pumping devices based on the electroosmotic effect were fabricated and characterized on silicon [31, 148-149]. Yao and Santiago *et al.* [146-7] extensively discussed optimization and other issues of electroosmotic micropump design, theory and experiment.   Table 1.6 summarizes comparisons between EHD, MHD and EO micropumps.

Table 1.6. Comparisons of EHD, MHD and EO micropumps.

Types	Max Flow Rate (μl/min)	Operating Voltage (V)	Pumping Fluids	Remarks
EHD	10^{-1}-10^4	10^1-10^3	Dielectric fluids	Only work with liquid with low conductivity (10^{-12} to 10^{-6}); thermal effect due to high current
MHD	10^1-10^2	~10^1-10^2	Many fluids for some pumps	Miniaturization challenge; thermal effect to induce Joule heating.
EO	5×10^{-3}--10^5	30-10^4	DI water, chemical buffer and many fluids for chemical and biological analysis	Thermal effect

1.5 The History of Electrowetting

The modern electrowetting originated from so-called "Electrocapillarity" firstly demonstrated by Gabriel Lippmann in 1875. In his classical experiment [173], as illustrated in Figure 1.9, the externally applied electrostatic charge significantly modified the capillary force at liquid-solid interface.

He observed that the mercury-electrolyte (a mixture of water and sulphuric acid (10% in volume)) interface change resulted from the force unbalance between the surface tension and pressure of mercury column. The alternation of surface tension attributed from charge density change at the interface. A great deal of work appeared to investigate the behaviour of electrified electrode instead of mercury directly in contact with electrolyte solution over 60 years ago [173]. It was actually an essential extension of classical electrocapillary experiments devoting to aqueous electrolyte in contact with a solid (electrodes or insulators) rather than a liquid metal. The capacitance varied in the order of several tens $\mu F/cm^2$ and the measured maximum potential for occurrence of electrocapillary was less than 1 V.
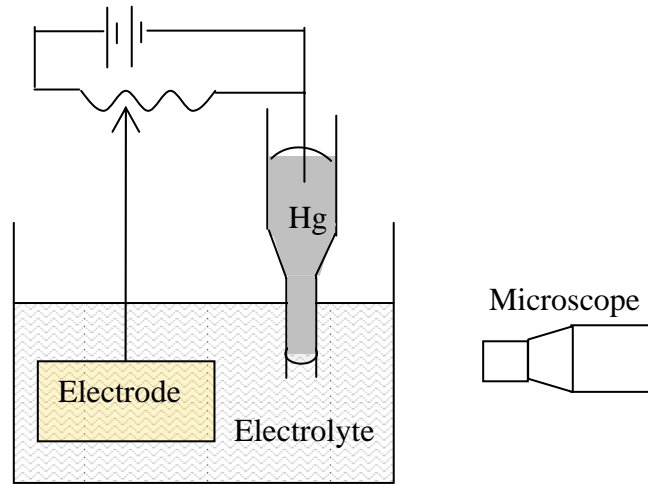
Fig. 1.9. Schematic of Lippmann apparatus for electrocapillary experiment [173].

In early 1980's, G. Beni *et al.* [189-190] from Bell Laboratory proposed a display method based on classical electrowetting. He introduced the idea of continuous electrowetting (CEW) in 1982 [191-2], which is schematically shown in Figure 1.10.
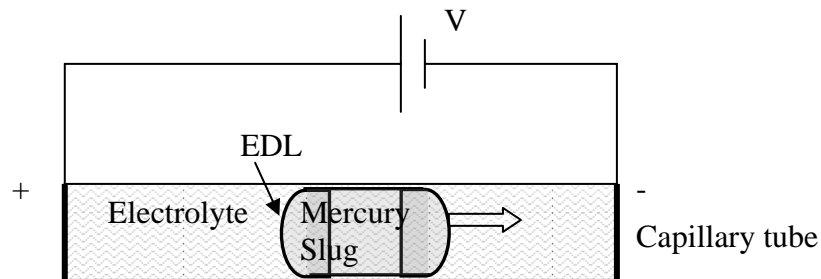
Fig. 1.10. CEW effect demonstration by G. Beni *et al*. [191-2].

A mercury slug was sealed in an electrolyte-filled capillary channel and a small gap was formed between mercury and channel walls. By applying a voltage potential across both ends of electrolyte, a potential difference formed across the mercury slug and consequently resulted in a surface tension gradient along the mercury-electrolyte interface. Thus, a surface tension gradient, accountable for lower surface tension on the right-hand side of mercury slug, drove the mercury slug to move to the right hand side

of Figure 1.10. G. Beni *et al.* [193] exploited optical switches based on the CEW mechanism. J. Lee and C. J. Kim *et al.* [194] successfully employed it as a microactuation mechanism in MEMS, and the mechanism of their device is depicted in Figure 1.11. Initially, without bias voltage, a liquid metal in a capillary filled with an electrolyte had a uniformly distributed charge density along the x-direction shown in Figure 1.11(a).

(a)

(b)
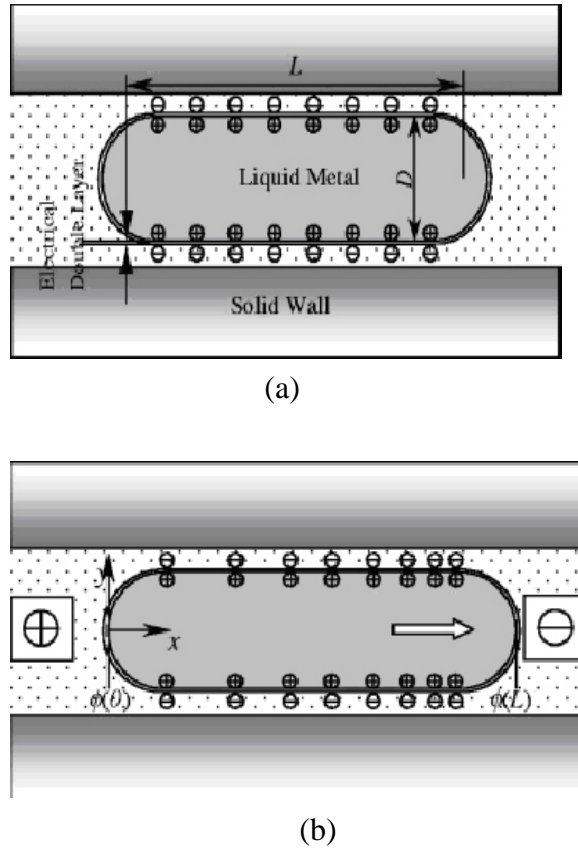
Fig. 1.11. CEW effect depicted by C. J. Kim *et al.*. (a) EDL and initial charges uniformly distributed; (b) electrically changed surface tension [194].

When a voltage was applied between two electrodes, the electric potential difference between the mercury and electrolyte varied along the x-direction and induced a charge redistribution. The more highly charged the interface became, the more the charges repelled each other, thereby decreased the cohesive forces and lowered the surface tension. Therefore, the surface tension on the right-hand side of the

mercury was less than that on the left-hand side. This gradient in surface tension induced motion of the mercury to the right, as shown in Figure 1.11(b). C. J. Kim *et al.* also demonstrated a surface tension induced micropump [195] and a liquid micromotor [142] fabricated by MEMS-based technologies. Unfortunately, these research efforts had not created any impactful practical applications or reliable devices easy for handling and manufacturing.

It was not until the early 1990's that the recent developments were initiated by Berge B. [196] who utilized a thin layer of solid insulator to electrically dispart electrolyte solution and metal electrode to prevent the occurrence of electrolysis problem, which was almost inevitable in classical electrowetting. M. Vallet, Berge B. and L. Vovelle [197] studied the wettability of poly(ethylene terephthalate) (PET) films and achieved a rather large (30°) and irreversible contact angle change of water drop upon applying a voltage of 200V across the 12-um-thick film. The irreversibility of contact angle shown in Figure 1.12(a) was found due to the surface modification of polymer film at the edge of liquid drop only. The workability of complex fluids like 0.1% copolyester solution in water with electrowetting was also investigated for industrial interest. The results shown in Figure 1.12(b) presented the overall behavior similar to that of pure water. Contact angle saturation, as well as contour line instability, i.e., the fragmentation of a liquid drop at high voltage, was reported. To dissolve a sufficient amount of salt in water was able to suppress the instability. Although the surface capacitance was very low (several hundreds pF/cm^2) and the applied voltage was very high (up to 3000V at a frequency from 50Hz to a few kilohertz), the thick insulating film was more efficiently tolerable with higher electric fields than the spontaneous potential barrier in systems without insulation between metal electrode and electrolyte.
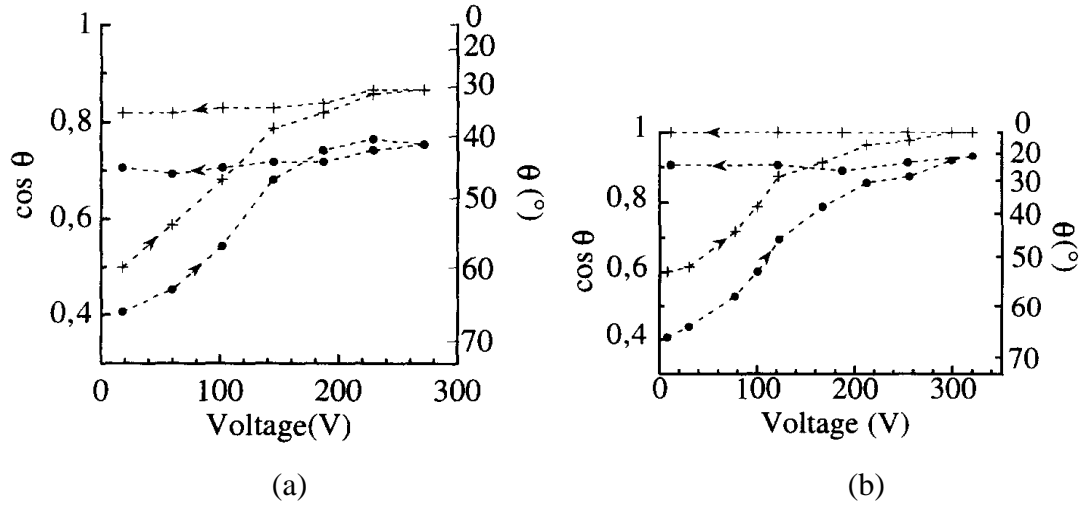
Fig. 1.12. Cosines of the receding (+) and advancing (•) contact angles of liquid drops on a PET film as a function of applied voltages. (a) pure water; (b) 0.1% copolyester solution in water [197].

V. Peykov *et al.* [198] experimentally proved that the contact angle and electrowetting effect was independent of the electrolyte concentration with a negligible high capacitance of Debye layer (the layer of charge around electrode) in serial with an insulating layer.

In general, this concept proposed by Berge B., which was further developed by H. J. J. Verheijen and M. W. J. Prins [199], becomes well-known as electrowetting-on-dielectric (EWOD). The induction of an insulating layer widely avails a lot of materials for controlling the electrode surface properties upon electrification. The tangible advantages offered by EWOD have attracted researchers to extensively focus on it as a microactuation principle and accounted for a lot of very exciting achievements and applications subsequently.

The number of investigations on electrowetting has been increased since the beginning of 21st century. It has been utilized to assist the fundamental studies of wetting dynamics to improve the liquid coating process for industry [200-1]. C. Quilliet and B. Berge [202] provided a possibility to tune the thickness of a fluid film

in a nanometric regime through applying an effective interface potential by electrowetting.

In general, many aspects related to electrowetting phenomena such as electrostatic field influence [203], electrical double layer [204], droplet movement [205] and contact angle hysteresis and saturation [206] etc., have been studied to understand the physics of electrowetting. Several papers have reviewed in detail the recent development of electrowetting covering from theoretical background, materials properties, surface morphologies to applications [207-9].

1.6 The Physics of Electrowetting

To understand the physics of electrowetting phenomena, let's first consider the experiment of EWOD effect as shown in Figure 1.13. A droplet of a conducting liquid is placed on an insulating layer of thickness d, which is deposited on a metal electrode. Applying a potential V between the droplet and the metal electrode, the charges are redistributed to induce the change of free energy/surface tension of droplet. Consequently, it results in a decrease of the contact angle θ. The changed droplet shape is represented by the dashed line.
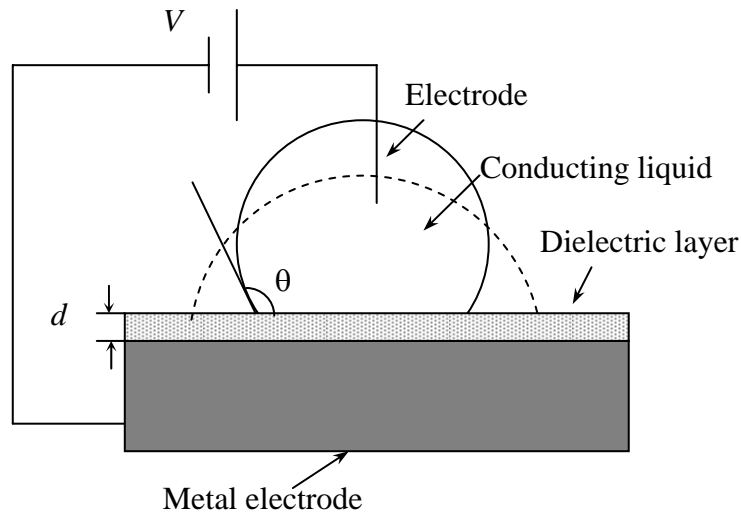
Fig. 1.13. Schematic of an electrowetting-on-dielectric experiment.

The dielectric layer of EWOD serves both to block the electron transfer and provide a hydrophobic surface that enables large variations and reversibility in contact angle. The solid-liquid region can be modeled as a parallel plate capacitor with the insulating layer as the medium between the plates as illustrated in Figure 1.14.
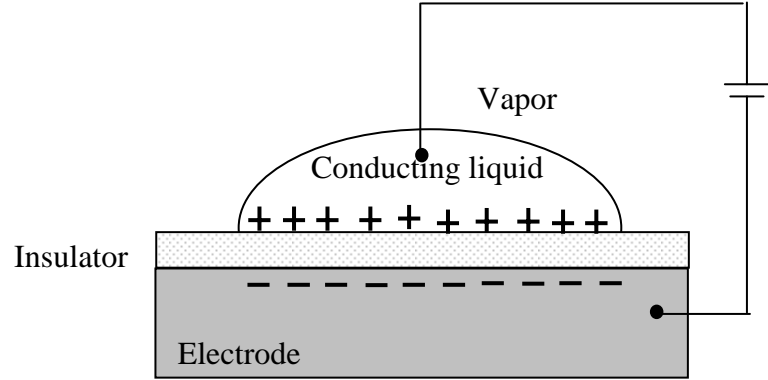
Fig. 1.14. Charge separation between the conductive liquid and electrode
due to the employment of an insulator.

The EWOD phenomenon was quantitatively interpreted in terms of Young and Lippmann's equations through many tangible experiments. Referring to Figure 1.2, a sessile drop reaching mechanical equilibrium on a smooth, inert and non-deformed homogeneous solid surface was defined by Thomas Young. Liquid evaporation and gravity are assumed to be negligible. Young's equation (Equation 1.1) is obtained by balancing the horizontal component of forces acting on the three-phase contact line.

The potential dependence of interfacial energies and contact angle was experimentally and theoretically studied by J. A. M. Sondag-Huethorst and L. G. J. Fokkink [210-11]. It was observed that both the liquid-vapor interfacial energy γ_{lv} and solid-vapor interfacial energy γ_{sv} were independent of electrical potential while the solid-liquid interfacial energy γ_{sl} and contact angle θ were functions of the electrode potential. Furthermore, γ_{sl} had contributions both from an electrical component (γ_{sl}^{el}) and a chemical (potential-independent) component (γ_{sl}^{ch}). The electrical component

γ_{sl}^{el} could be derived thermodynamically [196] through the change in free energy involved in establishing the electrical double layer, which equaled the double integral of the capacitance with respect to the potential. Sondag-Huethorst and Fokkink [210-11] gave a much elaborative derivation:

$$\gamma_{sl} = \gamma_{sl}^{ch} + \gamma_{sl}^{el} = \gamma_{sl}^{ch} - \iint Cd^2V \qquad (1.4)$$

Here, C is the capacitance of the solid-liquid interface. In that case, Equation (1.4) can be integrated, and the capacitance is only dependent on the thickness (d) of the dielectric layer and its dielectric constant ε ($C=\varepsilon_0\varepsilon/d$). Thus, the contact angle as a function of potential can be yielded by combination with Young's equation (Eq. 1.1) and Equation 1.4,

$$\cos\theta = \cos\theta_0 + \frac{\varepsilon_0\varepsilon V^2}{2\gamma_{lv}d} \qquad (1.5)$$

Here, θ is the contact angle under applied voltage of V, ε is the dielectric constant of the dielectric layer and ε_0 is the vacuum permittivity 8.854 x 10^{-12} F/m. Equation 1.5 is also called the Young-Lippmann equation. Note that the potential polarity does not influence the contact angle change. Although complete wetting with $\theta = 0°$ under sufficiently high voltage was supposed to occur based on Equation 1.5, it was never experimentally reported.

Equation 1.5 suggests that electrowetting is the consequential result of interfacial polarization, i.e., the induced electrical charges accumulating at the solid-liquid interface under external electrical potential to induce the change of solid-liquid surface tension, which accounts for the changing of contact angle. Moreover, the verification of Equation 1.5 has been successfully implemented by many investigators through correlating empirical results on contact angles within a moderate change of contact angle [198,212].

1.7 Applications and Limitations of Electrowetting-on-dielectric

1.7.1 Applications--Lab-on-a-chip

Two well-known research laboratories, i.e., Digital Microfluidics Lab of Prof. Richard Fair at Duke University and Micromanufacturing Lab of Prof. Chang-Jin Kim at UCLA, have pioneered the technique of moving liquid droplets using EWOD.

The research work of Prof. C. J. Kim *et al.* on EWOD actuation at early stage using liquid metal in direct contact with electrolyte has been mentioned in Section 1.5. However, only electrolyte could be transported and electrolysis would occur if the actuation voltage was above 2.5 V, under which the liquid metal (mercury) became so instable as to split into several slugs. This makes it very difficult to manipulate bio- and physiological fluids. Moreover, the employment of mercury, which is very toxic, results in the complexity and difficulty in manufacturing process. This actuation method has not created any impact for practical applications.

M. G. Pollack, Richard B. Fair and A. D. Shendrov [139, 213] presented a microactuation method for manipulation of discrete liquid drops on a substrate with an electrode array capable of individual addressability. The droplets could be transported along the sequential activation of the electrode, as shown in Figure 1.15. The cross-section schematic of sandwiched electrowetting based microactuator is shown in Figure 1.15(a).

The top substrate (glass) was deposited with homogenous and grounded electrode to provide electrical contact to liquid drops independent of their locations along the electrode array. The grounded electrode consisted of an optically-transparent indium-tin-oxide layer coated with a very thin layer (~ 60nm thick) of Teflon® AF 1600 serving as a hydrophobic surface of a contact angle of 104° with water. The thickness of Teflon® AF 1600 was identified to make sure the electrical contact to the

ground electrode. The control electrodes were deposited and patterned using chrome on the bottom substrate (also glass), coating with an 800-nm-thick film of Parylene C as an insulation layer and a Teflon AF 1600 layer as well as it on the top substrate. 0.1 M KCl liquid drops were dispensed in to the sandwiched structure with a gap of 0.3 mm surrounded with silicon oil. As the droplets must overlap with at least two neighbouring electrodes to form an electrical loop, an electrode pitch of 1.5 mm and a droplet diameter of 1.9 mm were determined in order to achieve a reliable and consistent droplet manipulation. The typical droplet volume ranged from 0.1 to 1 μl.

(a)

(b)
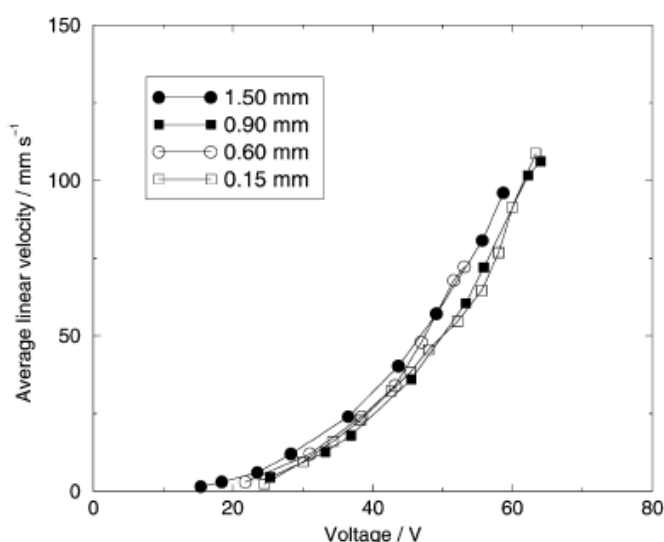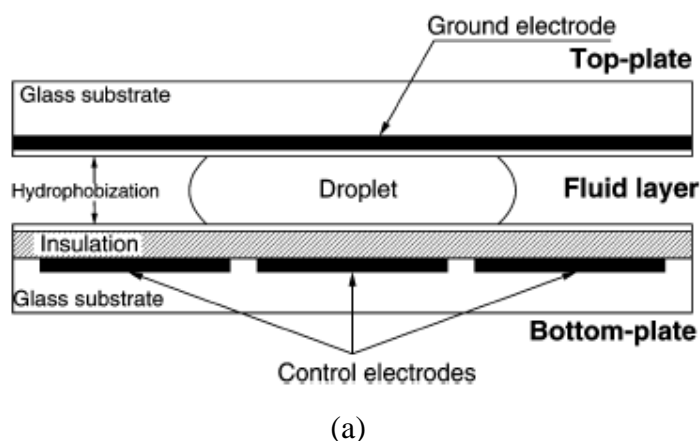
Fig. 1.15. A digital microfluidic lab-on-a-chip [213]. (a) Schematic of cross section of the electrowetting actuator; (b) The average velocity of the droplet as a function of voltage for transporting 1 centistokes (cSt) silicon oil.

With different patterns of voltage activations or electrode configurations, other manipulations such as splitting, merging or dispensing of microdroplets could be accomplished. The silicon oil here was to prevent the liquid evaporation which was a critical issue in micro scale at room temperature. Also, this sandwiched structure prevented ohmic heating and undesirable electrochemical reactions. Figure 1.15(b) shows the testing results of the average linear velocity of droplet as a function of voltage for transporting 1 cSt silicon oil. A rapid repeatability of well-above-10000 cycles was demonstrated together with a maximum transporting velocity of 10 cm/s.

With these above-mentioned established microfluids manipulation techniques using electrowetting, the up-to-date research efforts tend to demonstrate the lab-on-a-chip applications of EWOD-based systems and devices [214-217].

However, several limitations of these above-mentioned liquid droplets manipulation techniques are still clear visible. Firstly, all the experiment reported were done in silicon-oil environment, where droplet driving is much easier than in air environment. This silicon-oil environment definitely will bring a lot of contaminations and troubles for lab-on-a-applications such as chemical analysis system and clinical diagnostics. Secondly, the volume of liquid droplets manipulated in these devices was normally pre-defined by a pipette in the range of 0.05 –1.0 ul. This pre-defined volume should be able to assure liquid droplet to overlap the adjacent electrodes for movement. It makes difficult to miniaturize the device with key feature size of sub-micro meter range and additional equipment (pipette, dispenser, etc.) is necessary to precisely generate / control liquid droplets of a volume in sub-/ micro liter range.

1.7.2 Limitations

Firstly, Equation 1.5 was found to be valid as long as the value of voltage was below certain threshold. Unfortunately, beyond a certain system-dependent threshold voltage,

the contact angle as a function of the applied voltage has always been experimentally reported to be independent [198-99, 218-220]. A typical experiment done by M. Vallet *et al.*, as shown in Figure 1.16, shows the measurement of cosine of contact angle versus applied voltage for polytetrafluoroethylene (PTFE) films, where contact angle saturation occurs. Several factors such as high electric field strengths charging the insulator [197], the charge built up at the insulator surface [199], dielectric breakdown and adsorption of water molecules [201] have been reported to result in the contact angle saturation phenomena based on experimental results respectively. However, no individual theory has yet been verified to be applicable to such a wide range of electrowetting systems with different specifications.
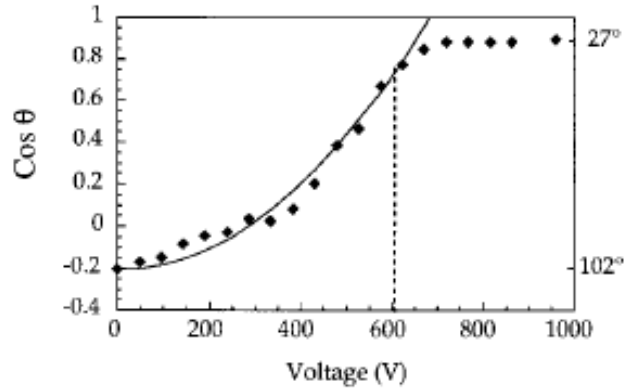
Fig. 1.16. Cosine of contact angle as a function of applied voltage on a PTFE film of 50 μm thick, contact angle saturation occurred after above 600 V, reproduced from [218].

Secondly, dielectric breakdown mostly induced by the electrical properties and the thickness of dielectric layer causes dielectric layer to fail to function as a capacitor because the charges do not accumulate there. Since the breakdown voltage depends on the electric field, a minimum dielectric thickness (d_{min}) is always required to operate the device safely. Referring to Equation 1.5, we are able to avoid dielectric breakdown either by increasing the thickness of dielectric layer, the capacitance C of capacitor, or

its dielectric constant ε. However, increasing dielectric layer thickness requires higher voltage to achieve the same effect, thus, consumes more power. A hydrophobic dielectric of high dielectric constant and strength is ideal for EWOD. Unfortunately, such materials are very limited. The properties of dielectric materials employed in EWOD are discussed in detail in Chapter 2.

Lastly, the reproducibility and stability of many reported EWOD experiments or devices are quite questionable for the applicability with industry and commercialization. Very few tangible experimental data about these specifications have been presented.

1.8   Motivation and Scope

Although a lot of research development efforts and investments have been made during the past two more decades, the disparity between research achievement, publications and patents and commercialized products of microfluidics is still clearly visible. Very few patents, achievements and technologies are transformed into products. Caliper Life Sciences, among very few successful companies devoted to microfluidics, has successfully commercialized integrated chips with minimum requirement of fabrication and integration.   These chips use high voltages to electrokinetically transport liquid "plugs" through a network of microchannels with mixing and separations occurring at predefined points along the flow pathway [208]. However, the application of micromachining technology to make such miniaturized chips was in its infancy and the applied high driving voltage of 5000 V limited the applications of these chips.

On the other hand, traditional micropumps utilize electrostatic force, thermopneumatic force, electromagnetic force etc., as the driving source. However, the

piezo actuator to generate electrostatic force is difficult for miniaturization in microscale, and the thermopneumatic or electromagnetic force consumes a large amount of electric power. Therefore, the micropumps based on those above-mentioned methods are difficult to be used in the remote environmental monitoring systems, implantable medical devices and chemical analysis systems because of their relative big size or high power consumption. There are a few publications and patents on micropumps utilizing the continuous electrowetting mechanism. This mechanism utilizes the surface tension force generated between the liquid metal and the electrolyte in order to pump fluid. As mercury is usually used as the liquid metal, this type of micropump has a lot of problems in implementation due to the difficulty and complexity of the fabrication process of the mercury.

Electrowetting-on-dielectrics (EWOD) has been extensively studied and demonstrated to be able to manipulate discrete liquid droplets in micro scale [201-203]. However, these liquid droplets should be electrolyte to be pumped by liquid metal (mercury) based on CEW mechanism; the liquid droplets were transported in silicon-oil environment and should overlap the neighboring electrodes for electrically actuation; the volume of liquid droplets was pre-defined by addition equipment like pipet or dispenser. All these drawbacks make those above-mentioned EWOD devices very difficult to handle or manipulate bio-physiological fluids in sub-micro liter and even smaller range.

In recent years, many microfluidic lab-on-a-chip systems and devices, which incorporate all the necessary steps to perform a specified chemical analysis (sample treatment, transport, reactions and detections) or bioprocessing (cell isolation, cell lysis, DNA purification and recovery) etc. [221-22]. An example of such a system for the detection of ammonia is shown in Figure1.17 and its analysis procedure is as

follows: a sample fluid is fed from a branch into a main channel with a continuous carrier fluid of de-mineralized water. The first reagent is added into the sample fluid and mixed together in the first mixer. Then the fluids pass further down the main channel and mix with another reagent in the 2nd mixer. After that, the mixture runs through a reactor channel and reaches a detection chamber, where light adsorption at a wavelength of 590 nm is measured. From this adsorption measurement, the original amount of ammonia is calculated [221]. The fluids are propelled by 4 peristaltic piezo-electrically driven micropumps, which are difficult to be further miniaturized and need a very high driving voltage. The above-mentioned EWOD systems and devices are not capable of being integrated into this chemical analysis system because of their limitations or drawbacks discussed above.
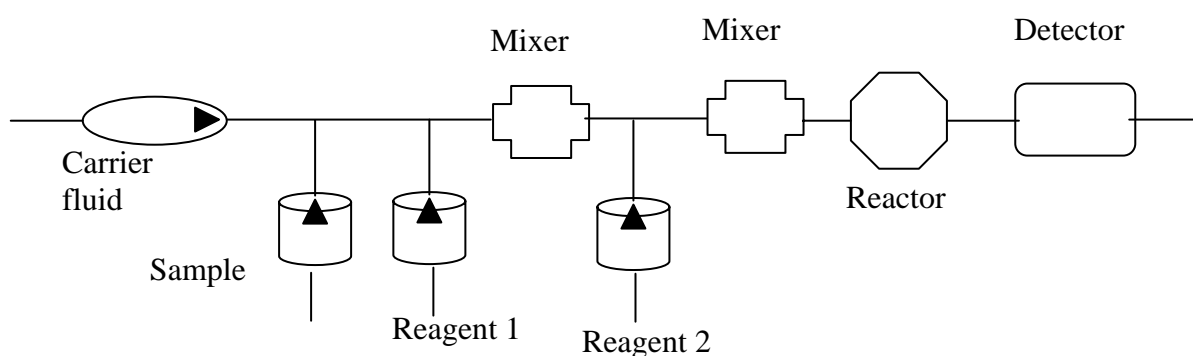
Fig. 1.17. The schematic of a miniaturized chemical analysis system for the detection of ammonia [221].

Accordingly, the objective of this research work is to refine the fundamental liquid manipulation techniques and design, fabricate, test and characterize a hydrophobicity controlled microfluidic dispenser with an in-built metering feature, which can be integrated into a lab-on-a-chip performing specific chemical analysis, clinical diagnostic and environmental monitoring. This microfluidic dispenser in

combination with a pneumatic pump is able to provide a precisely-controlled liquid flow in the range of micro liter to pico liter. This study will focus on the dispensing behavior and development of this microfluidic device based on electrowetting-on-dielectric. The transportability, controllability, reproducibility of liquid manipulation will be the focus of this work. The details of this microfluidic dispenser will be presented in Chapter 3.

The deliverables of this project can be divided into the following:

- System design for dispensing manipulatable liquid column using controlled hydrophobicity.

- Surface properties investigation and optimization for dielectric layers.

- Modelling and simulation of the flow of a liquid column under the action of an applied electrical field.

- Device testing and characterization.

1.9 Thesis Overview

In this thesis, the design, modeling analysis, realization together with testing and characterization of an electrowetting based microfluidic dispenser are presented. This section summarizes the content of this thesis, which comprises 6 chapters. Chapter 1 gives a brief introduction of the background and research trends of microfluidics, summarizing the biological applications of microfluidic devices and forces/fields employed to manipulate microflows. Surface tension is conceptually introduced followed by a brief analysis of dimensionless numbers of microfluidics. After that, the historical development and fundamental theory of electrowetting are reviewed followed by an introduction of its applications and limitations. Several typical

pumping devices based on electrowetting are demonstrated and their limitations and drawbacks are depicted in terms of lab-on-a-chip applications. Finally, the motivations and project scope are presented to study and develop the dispensing behavior of a microfluidic device which can be incorporated into a lab-on-a-chip for specific chemical analysis, clinical diagnostic and environmental morning.

Chapter 2 reviews and analyzes material property issues relevant to electrowetting-on-dielelctrics (EWOD), among which, the dielectric layer is more important in influencing EWOD performance. The investigation and optimization of the surface properties of dielectric layers are presented in Chapter 2. Several materials for dielectrics were tested and compared for determining the optimized parameters for device integration.

Chapter 3 demonstrates the conceptual design and working principles of the proposed microfluidic dispenser. The hydrodynamic behavior of liquid dominated by surface tension will be analyzed including the dynamic changing of contact angle and the net force acting on the liquid-air interface in EWOD. The average flow rate and the principle radius of liquid meniscus as a function of time are predicted together with the simulation results of the electrical potential distribution and surface charge distribution upon applying potentials.

The device realization by silicon, glass and polymer microfabrication technologies is introduced in Chapter 4. The fabrication process flow includes fabrication of the top plate, the bottom plate and bonding. The top plate made of glass has the electrodes array and the microchannel is formed by SU-8 on bottom plate of silicon. Bonding technology is illustrated to complete the device fabrication.

Chapter 5 presents the characterization of the device. The experimental procedure is briefly mentioned in the beginning of the chapter. A comprehensive discussion on the experimental observations is made at the end of this chapter.

Chapter 6 concludes this research work and overlooks the challenging issues as future works for further development of this project.

CHAPTER 2

DIELECTRIC MATERIALS FOR EWOD

This chapter discusses the fundamental building blocks of electrowetting-on-dielectric (EWOD) actuation, and the importance of these building blocks in determining the EWOD mechanism. Typically, a fully functional EWOD device consists of four essential components, that is, an *ionized liquid* (including pure water) working as a medium, a *dielectric material* providing the capacitance between liquid and electrode. the hydrophobic surface property at the solid-liquid interface (some dielectrics require a separated top-coating of hydrophobic layer), and finally a conductive material serving as the *electrodes*. The material properties of these four components influence the performance of a EWOD device in different ways.

2.1 EWOD Dependence on Liquids and Electrodes

Conventionally, the liquid electrolyte is assumed to be a perfect conductor in classical electrowetting experiments, i.e. the water is assumed to be in direct contact with metal electrodes. In recent years, researchers have investigated the effects of a variety of liquids on EWOD. Their results indicate that the requisitions of liquid properties for EWOD such as concentration and charge carrying ability are not so rigorous. Using

typical liquid electrolytes like KCl and K_2SO_4 with concentrations of the order of 0.01

M/liter − 1.0 M/liter, Verhejen *et al.* [199] reported the independence of ion type, ion

molarity and ion valence of electrolytes on the applied voltages for EWOD. Through

an improved Pellat's apparatus for demonstration of electrically induced capillary rise,

T. B. Jones *et al.* [223] observed EWOD phenomenon using deionized (DI) water with

frequencies of 20 Hz -20 kHz under voltages of up to 300V. Figure 2.1 shows the

schematic of experimental set-up and the frequency dependence of DI water on applied

voltage.

(a)   (b)
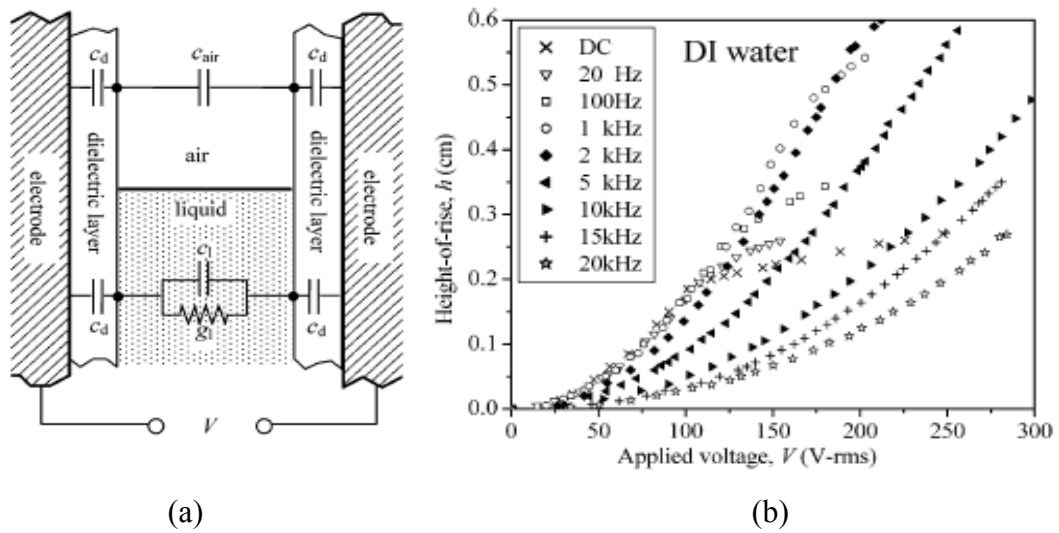
Fig. 2.1. Improved Pellat's experiment for demonstration of electrically induced
capillary rise [224]. (a) Schematic of set up and electric circuit simplification.
(b) Frequency dependence of DI water on applied voltages.

F. Mugele *et al.* [224] also presented an EWOD experiment with DI water on

indium-tin-oxide (ITO) electrode coated with a thin layer of Teflon[®] AF and obtained

a noticeable contact angle change. Electrowetting phenomenon was also observed for

mixtures of salt solutions (NaCl or Na_2SO_4) with other species, i.e., glycerol [224-6],

ethanol [227] and methanol [228], without any degradation of EWOD performance.

In biomedical applications, researchers have explored the applicability of

EWOD devices in the presence of biomolecules and physiological fluids. Yoon and

Garrell [229] showed that EWOD occurred with biofluids containing protein, DNA and adult bovine whole serum of a biomolecule concentration of 4μg/ml, although the performance was degraded by biomolecules adsorption into the insulation layer giving rise to the reduced contact angle change and hysteresis. The compatibility of EWOD with physiological fluids such as insulin, cytochrome, myoglobin etc. has been demonstrated by A. R. Wheeler *et al.* using a EWOD based chip [230]. Recently, EWOD actuation of human physiological fluids containing human whole blood, serum, plasma, urine, saliva sweat and tears was demonstrated at 20 Hz and less than 65 V by Prof. R. B. Fair *et al.* [219, 231] using an integrated digital microfluidic chip.

Hitherto, the findings indicate that the performance of a EWOD device has limited dependence on the liquids properties.

Those commonly used metal electrodes in IC and PCB industry, which can be patterned by photolithography and lift off / wet etching processes, are also widely employed in EWOD. These materials includes gold (Au) [198,232,233], silver (Ag) [205], aluminum (Al) [140,199], chromium (Cr) [232], platinum (Pt) [232,234], titanium (Ti) [232] and Si [223, 230, 145] with a typical thickness of the order of several to 200 nanometers. Stainless steel sheets were also reported as electrodes for EWOD [197,218, 235].

Due to the increasing practical demand to visualize the operation of the device or induce light transmission, it is necessary to incorporate the top-substrate conductive material which should be semi / transparent to light into the EWOD device. Indium-tin-oxide (ITO) films of 50-200 nm thickness intrinsically have a transmittance of above 80% with sheet resistances of less than 10 Ω/sq. Thus, ITO has been widely used as the top-substrate ground electrode in EWOD [145, 236, 231-2, 237-44]. In general, electrode property has almost no influence on EWOD.

2.2   EWOD Dependence on Dielectrics

The material properties of dielectric layer have drawn a lot of attentions since the emergence of EWOD because it has significant impact on the performance of EWOD. There have been a significant number of research works focusing on optimizing the extrinsic properties (e.g. thickness, applied voltages) and intrinsic properties (e.g. surface property, dielectric strength or constant) of EWOD, where the corresponding research results provide valuable reference for practical EWOD designs and applications.

Referring to the Young-Lippmann equation (Equation 1.5), there are two important criteria in the design of a EWOD device, i.e., firstly, the inherent contact angle (without external applied voltage) should be as large as possible to achieve maximum contact angle variation; and secondly, the dielectric layer should be as thin as possible. To obtain large contact angle at zero applied voltage, one can either use highly hydrophobic insulators or hydrophilic insulators deposited with a very thin hydrophobic layer without blocking electrical connection. Minimizing the dielectric thickness may give rise to poor dielectric strength, and may cause further dielectric breakdown. Nevertheless, the insulators should be of high dielectric constant and high dielectric strength to facilitate application of a higher potential across the dielectric. Beside these considerations, applied potential or power consumption should be minimized when operating the devices / systems. Materials employed should be chemically inert / resistant to achieve reliability. Mechanical, thermal and charge stability are important for manufacturing reproducibility. Biocompatibility and minimal bimolecular adsorption of materials must be taken into considerations when handling bio- and physiological fluids.

There are several materials that can be used in designing a EWOD device, which is discussed below. Polymer materials, induced as insulators at the early stage of EWOD, have been extensively studied and employed including parylene-C [139-140,198,224,234-5,237,245] and parylene-N [199], conventional Teflon® films [218,238,245], Teflon® AF [139-140,198-9, 234,237] and Cytop™ [239-243] amorphous fluoropolymer, polydimethylsiloxane (PDMS) [205], and polyimide [237,239], as well as other commercially available polymers like PET [197,218] and polyethylene (PE) [246] etc.. In EWOD, parylene has been reported exclusively to work together with a top-coated hydrophobic thin layer like Teflon® AF 1600. Teflon® AF has the lowest dielectric constant of 1.93 among known polymers, which exposes itself a candidate for next-generation interlevel dielectrics [247] but a poor dielectric capacitor. Therefore, it has frequently served only as a hydrophobic layer instead of a prime insulator in electrowetting. It has a typical thickness of the order of 100 nm in between liquid and insulation layer without electrical isolation in order to provide a low contact angle hysteresis (8°) [237]. Cytop™ has actively appeared as a new member of dielectrics for EWOD since the early 2000s. Compared to Teflon, Cytop™ yields lower contact angle hysteresis (4°) and impermeability, better light transmission for optical applications [248]. Poly(dimethylsiloxane) (PDMS) Sylgard® 184, Dow Corning, becomes a potentially attractive material for the integrated electrowetting based devices because of its very hydrophobic surface property and low material cost compared to Teflon. However, a potential of 500 V, a rather high voltage for EWOD, was required to obtain a contact angle change of 35° on a 38 μm thick PDMS film [205]. Compared to its high popularity as a molding material for microfluidic devices, almost no interests of PDMS as an insulating material have been demonstrated in recent years. Polyimide has a dielectric constant of 3.4 and dielectric strength of 22

kV/mm, which are higher than that of parylene-C. However, it demands much higher applied voltages to achieve the same magnitude of contact angle change as that of parylene-C [237]. Thus, polyimide was employed as an intermediate dielectric only at early prototypes and its popularity among EWOD community becomes very poor nowadays. Table 2.1 summarizes and compares the materials properties and specifications of these above-mentioned polymers employed in EWOD.

Table 2.1. Specifications and comparisons of polymer materials for EWOD.

Materials	Parylene -N & -C [139-140,198-9, 224,234-5,237,245]	Teflon® AF 1600 [140,198-9,237]	Teflon (PTFE) [218,238,245]	Cytop™ [239-243,248-250]	PDMS [205]	Polyimide [237,239]
Dielectric Strength (kV/mm)	276 (-N) 268 (-C)	21	60	110	21.2	22
Dielectric Constant	2.65 (-N) 3.15 (-C)	1.93	2.1	2.1	2.3-2.8	3.4
Applied Voltage (V)	$\pm$ 240 (DC) <1k (AC 50 ~ 20 kHz)	--	<300 (DC) <600 (AC 1 kHz)	120 (DC) <800 (AC 2 kHz)	$\pm$ 500 (DC)	< 400 (DC)
Thickness (μm)	3.5-30	0.01-0.1	25-50	0.1-1	38	6-35
Contact Angle of Water (°)	126°	120	114	110	120	50-80
Fabrication Method	Chemical vapor deposition	Spin or dip coating	Commercial	Spin coating	Spin coating	Spin coating

Another interesting group of materials as inorganic insulators employed in EWOD includes silicon dioxide (SiO_2) [229,234,220,232,244], silicon nitride (SiN_x) [240, 243] and the Sol-Gel derived barium strontium titanate (BST) [$(Ba,Sr)TiO_3$] [232,234]. As their original surface properties exhibit hydrophilic (water contact angle is 46.7° [251], 30° [252] and 40.8° [253] for SiO_2, Si_3N_4 and BST, respectively),

normally they have to perform electrowetting actuation in combination with a hydrophobic top-coating layer like Teflon® AF 1600.

The prime benefits of SiO_2 as a capacitive insulator are from its high dielectric constant, high dielectric strength and availability as one of the predominate materials in MEMS and microelectronics industry. Compared to Teflon® AF as an insulator, SiO_2 is able to offer a larger contact angle change at the same applied voltage due to its higher dielectric constant [234]. Figure 2.2 compares the thickness effect of silicon dioxide and parylene on the contact angle change as a function of applied voltage [234].
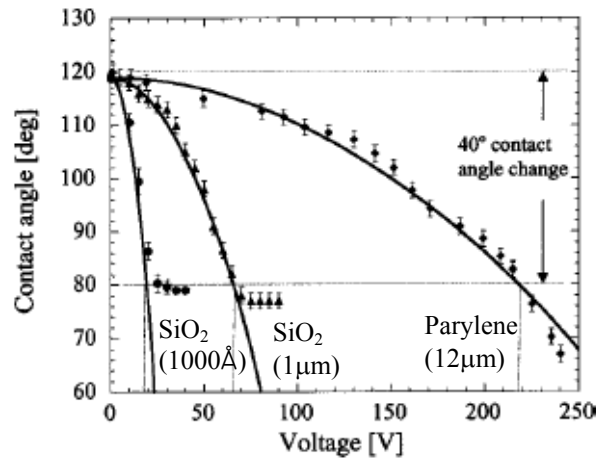
Fig. 2.2. The thickness effect of dielectrics on contact angle change as a function of applied potential [234]. From the left, 1000 Å SiO_2 (●), 1 μm oxide (▲) and 12 μm Parylene (♦).

Silicon nitride was incorporated into a tunable liquid lens in combination with a 1-μm thick Cytop™ layer (hydrophobic coating) [240, 243]. No changes were observed under the applied voltage of 40 V for a droplet of 6 μl.

Barium Strontium Titanate (BST) has a significantly higher dielectric constant (200-300) than that of SiO_2 and SiN_x. Therefore, it can provide even lower operation voltage (15 V_{dc}) to reduce the contact angle from 120° to 80°. Metal organic chemical

vapor deposition (MOCVD) can be used to deposit this thin film with a typical thickness of the order of less than 100 nm [232,234]. Figure 2.3 shows the comparisons of contact angle change as a function of applied voltage between dielectrics including BST, SiO_2 and Teflon AF. The theoretical trends predicted by the Young-Lippmann equation for these three materials are also plotted respectively [234]. Table 2.2 summarizes the material properties of SiO_2, SiN_4 and BST.
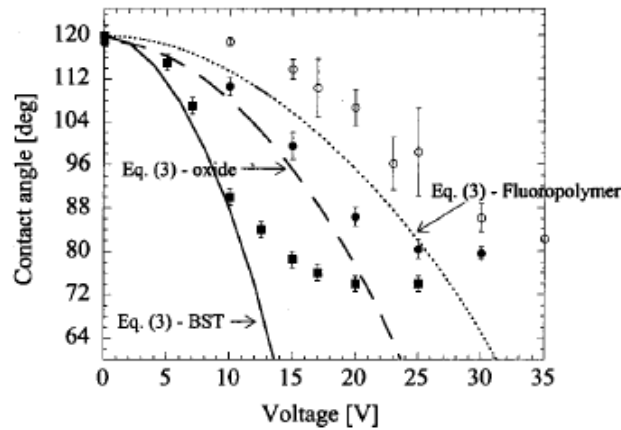
Fig. 2.3. Contact angle change as a function of applied voltage for BST (700Å, ■), SiO_2 (1000Å, ●) and Teflon® AF (1200Å, ○). The trends predicted by the Young-Lippmann equation are represented by lines respectively [234].

Table 2.2 Comparisons of inorganic insulators for EWOD

Materials	SiO_2 [256]	Si_3N_4 [256]	BST [257]
Dielectric Strength (kV/mm)	400-600	500	18-54
Dielectric Constant	3.9	7.5	225-265
Applied Voltage (V)	$V_{dc} \geq 25$	> 40	$V_{dc} \geq 15$
Thickness (μm)	100 nm-1 μm	150 nm	70 nm
Contact Angle of Water (°)	46.7	30	40.8
Fabrication Method	Thermal oxidation or PECVD	Chemical vapor deposition	MOCVD

Self-assembled monolayers (SAMs) has been studied and incorporated with electrowetting since last decade. SAMs normally can be prepared by immersing the substrates coated with gold films (~100 nm thick) into ethanoic solution for several

hours and its typical thickness is around 20-30 angstroms [258]. The value of dielectric constant for SAMs was obtained analytically nearly at 2 [259], which was in agreement with the results through experiment [210]. Huethorst *et al.* reported the electrowetting effect using SAMs as dielectric material on gold surface, in which a partial irreversibility was caused by contact angle hysteresis [211]. The wetting was observed to appear till current was generated to give rise to the degradation of monolayer desorption, which accounted for the irreversibility of contact angle [233]. Gorman *et al.* demonstrated a relative low reproducibility of about 50 cycles with a very low applied voltage of 1.7 V at a frequency of 1 min/cycle [260]. In short, the discreetness of employment of SAMs as dielectric layer for EWOD can be observed because of its limited stability and contact angle irreversibility.

Progress of EWOD development is summarized in Table 2.3, showing the corresponding applied voltages, dielectric materials and features. The research of EWOD at early stage was initiated by both industrial companies (Philips Research Laboratories and Bell Labs) and academics. There are broadening interests in EWOD recently, and increasing success stories in commercializing EWOD.

Table 2.3. Progress of EWOD development.

Year / Ref.	Voltage	Dielectrics	Features
1980 [261]	AC 0-2 kV (50 or 1k Hz)	PE (200-900 μm)	• θ changes from 80° to ~20° • Irreversibility
1993 [196]	AC (50-3k Hz)	PTFE (53 μm)	• Reversibility • Saturation
1994 [211]	DC (0-0.9 V)	SAM	• Limited reversibility • Hysteresis
1995 [259]	DC (0-1.7 V)	SAM	• θ changes from 128° to ~37° • Reversibility
1996 [197]	AC (0-3 kV at 50 Hz- a few kHz)	PET (12 μm)	• Reversibility at moderate voltage • Contour line instability at high voltages
1998 [237]	DC (0-400 V)	Parylene C (6 -10 μm) or polyimide (18-35 μm) + Teflon® AF 1600 (0.1 μm)	• Hysteresis (8°) • Reversibility • θ changes from 110° to ~60°
1999 [199]	DC (± 240 V)	Parylene N (10 μm) +Teflon® AF 1600 (30 nm) + silicon oil	• Hysteresis (2°) • Reversibility • Polarity, ion type, molarity and ion valence independent
2000 [139]	DC (55-80 V)	Parylene C (700 nm) + Teflon® AF1600 (200 nm)	• Reproducibility • High transportation speed • Relative stability
2000 [260]	1.0 mW/cm² (light intensity	Photoisomerizable monolayer	• Reversibility • θ changes from 24° to 11°
2001 [140]	DC (± 227 V)	Parylene C (11.5 μm) + Teflon® AF1600 (10 nm)	• Weak hysteresis • High transportation speed
2002 [239]	DC (0-100 V)	Polyimide (2 μm) + Cytop™ (1 μm)	• Reversibility •Pinning-free voltage control
2002 [262]	DC (15-100 V)	Parylene C (800nm) + Teflon® AF1600 (60nm)	• High reproducibility • High transportation speed
2003 [232]	DC (15-25V)	SiO$_2$ (0.1 μm) / BST (70 nm) +Teflon® (20nm)	• Low voltage operation • Reproducibility • Versatile droplet handling
2003 [145]	AC (100V at 100-700Hz) /	Photoconductive material (amorphous Si)	• Light induced • high transportation speed
2004 [236]	AC (65 V at 20 Hz)	Parylene C (800nm) + Teflon® AF1600 (50nm) + silicon oil	• Biocompatibility • High transportation rate • High reproducibility
2005 [225]	AC (0-1 kV at 1-10 kHz)	Teflon® AF (3-5 μm) +silicon oil	• Saturation • Contact line instability
2006 [243]	DC (~120 V)	SiO$_2$ (0.3 μm) + Cytop™ (0.2 μm)	• High transportation speed • Reliability

2.3 Dielectric Breakdown Analysis

Dielectric breakdown is a phenomenon where insulators are forced to conduct electricity. In EWOD, it refers to the failure of the insulating materials which results in a short circuit between the electrodes and conductive liquids. As mentioned in Section 1.7.2, a dielectric breakdown damages the dielectric layer, and charges do not accumulate at the interface of dielectric and conducting layer to give rise to stop EWOD. Thus, the dielectric strength is one of the most important factors in selecting insulator materials and caution must be taken into determining the minimum thickness of an insulating layer.

Rearranging the Young-Lippmann equation, the electrical potential required to induce a desirable variation of contact angle ($\Delta\cos\theta$) can be shown as:

$$V_{\Delta\cos\theta} = \sqrt{\frac{2d\gamma_{lv}\Delta\cos\theta}{\varepsilon_0\varepsilon}} \tag{2.1}$$

Also, the dielectric breakdown voltage V_{bd}, i.e. the minimum voltage to make an insulator act as a conductor, equals to

$$V_{BD} = E_{ds} \cdot d \tag{2.2}$$

Here, E_{ds} is the dielectric strength and d is the thickness of the insulator. Figure 2.5 compares the effects of the required electrowetting voltage and the breakdown voltage on the insulator thickness respectively, using Cytop™ as the reference material. The required EW voltage to induce a specific $\Delta\theta$ is proportional to the square root of the thickness of the dielectric layer with a fix dielectric constant. In contrast, the breakdown voltage is linear to the thickness of the dielectric layer. The minimum insulator thickness (correspondingly a minimum voltage) required to obtain a specific $\Delta\theta$ for a given dielectric strength and dielectric constant is determined by the intersection of these two functions of square root and linearity. Dielectric breakdown

always occurs before obtaining the desired contact angle change with thickness less than the minimum value. Take note that the result presented in Figure 2.4 is not applicable for nanoscale effect of SAMs, as reported by Moon *et al.* [2234].
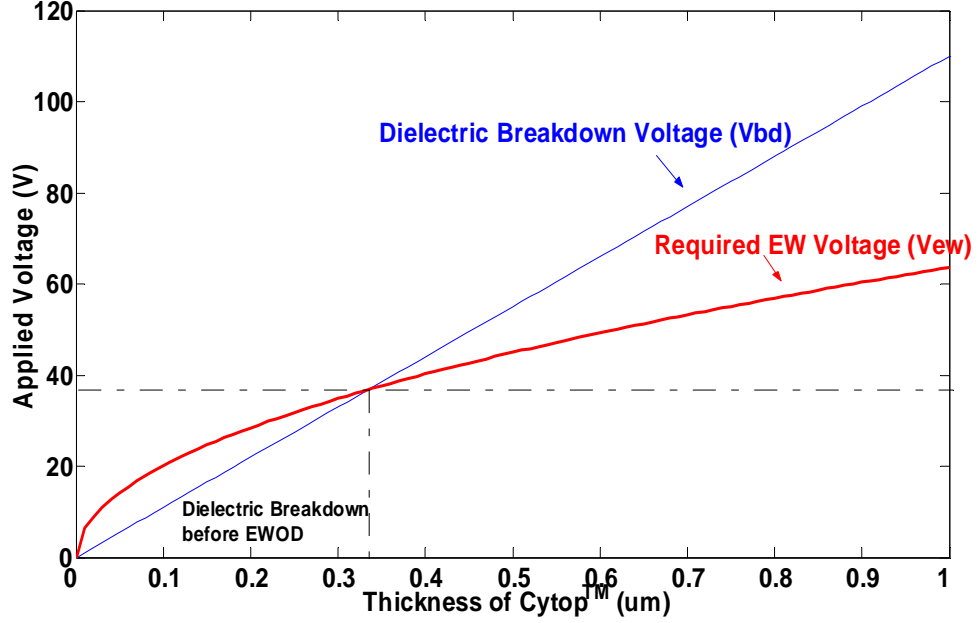
Fig. 2.4. Electrowetting voltage to obtain a specific contact angle change ($\Delta\theta$) and dielectric breakdown voltage as a function of dielectric layer thickness. For the example demonstrated, the dielectric layer is assumed to be Cytop™ with ε=2.1, E_{ds}=110 MV/m, and θ is from 110°to 80°.

Values of the minimum dielectric thickness (d_{min}) and corresponding dielectric breakdown voltage (V_{bd}) for different dielectrics are calculated and listed in Table 2.4. The dielectric breakdown voltage V_{bd} is the minimum theoretical voltage required to initiate EWOD effect in air without any failure of insulator. The upper and lower bound of linearly larger operational voltage and dielectric thickness can be improved for safety of breakdown. A practically acceptable maximum driving voltage of 100 V was taken to calculate the minimum (limited by dielectric strength E_{ds}) and maximum (limited by driving voltage V_{ew}) value of thickness for each dielectric in Table 2.4.

Table 2.4. The dielectric breakdown voltage at corresponding minimum thickness for typical dielectrics. (Minimum and maximum dielectric thickness under 100 V).

Dielectrics	d_{min} (µm)	V_{bd} (V)	100V		$\Delta\theta$ (°)
			d_{min} (µm)	d_{max} (µm)	
Cytop™	0.33	36.74	0.91	2.47	110~80
PDMS	4.27	90.59	4.72	5.21	120~100
Teflon® AF 1600	13.04	273.84	1.74	4.76	120~80
Parylene C	74.16	511.704	2.83	14.49	126~85
BST	2.87×10^{-3}	0.14	2	1392	40.8~30
SiO$_2$	3.05×10^{-3}	1.5	0.2	13.14	46.7~30

The values of contact angle change for each dielectric material are based on the measurement results which will be discussed in Section 2.4. Electrowetting and dielectric breakdown voltage as a function of the dielectric thickness for each dielectric material are graphically shown from Figure 2.5(a)-(e), respectively.
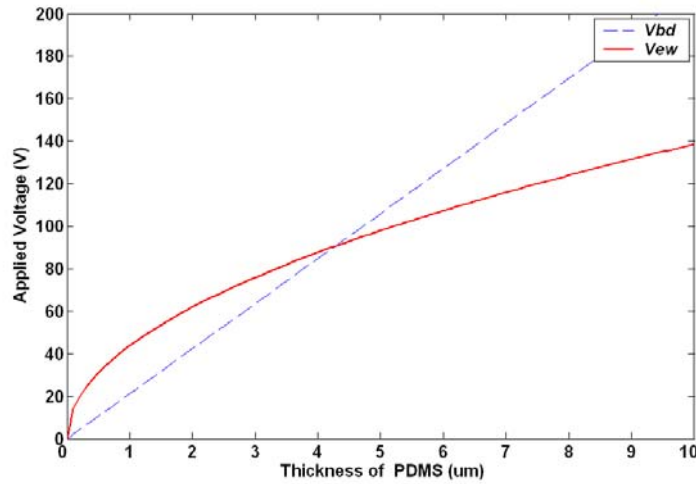
(a)
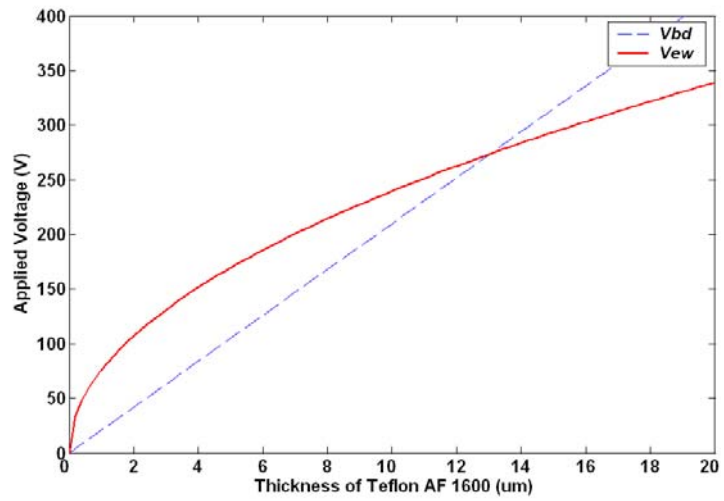
(b)
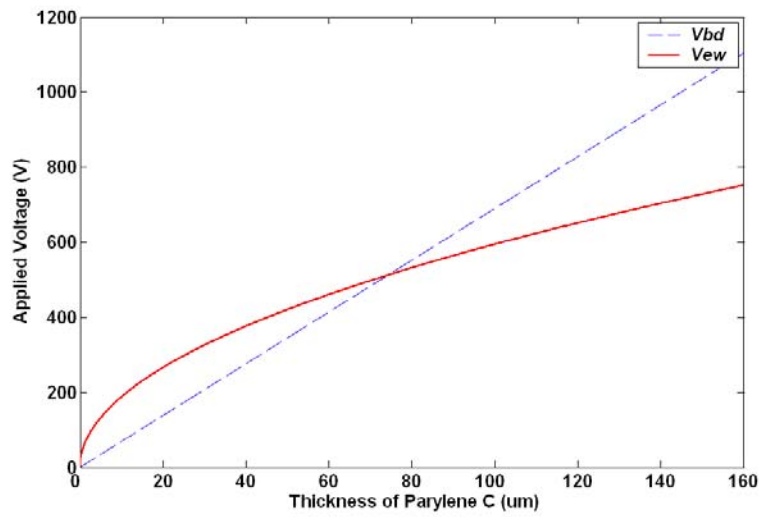
(c)
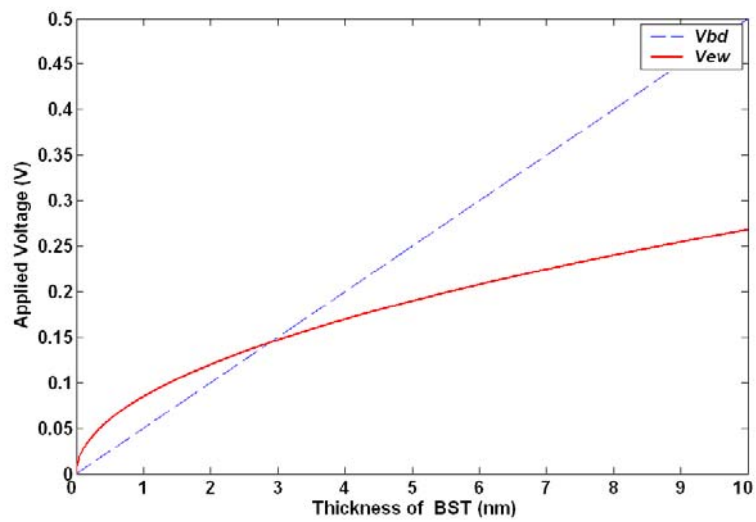
(d)
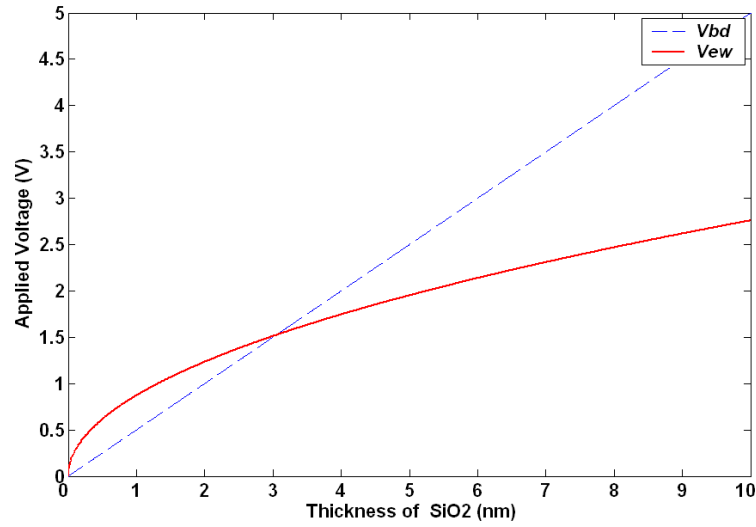
(e)

Fig. 2.5. Electrowetting voltage (solid line, V_{ew}) required to achieve a specific contact angle change ($\Delta\theta$), breakdown voltage (dashed line, V_{bd}) as a function of thickness for each dielectric material. Dielectrics include:
(a) PDMS, (b) Teflon® AF 1600, (c) Parylene C, (d) BST, (e) SiO$_2$.

To summarize, Parylene C coated with a thin layer of Teflon® AF 1600 exhibits the highest variation of contact angle (~40°) which can sustain up to 300 V before dielectric breakdown. In contrast, BST and SiO$_2$ materials have a small breakdown voltage of 0.14-1.5 V and a small initial contact angle (< 50°) which are not sufficient to generate adequate electrowetting force for EWOD actuation. Thus, they are not suitable as dielectric materials. A moderate contact angle change (20°) can be obtained with PDMS at a relatively high applied voltage of about 100 V. In contrast, the contact angle variation of Cytop™ is as large as 30° under the same voltage and EWOD can always be operated at as low as 40 V before dielectric breakdown.

Besides the dielectric layer, dielectric breakdown may also happen in the medium (air or silicon oil) surrounding the liquid. Therefore, silicon oil immiscible with water has normally been employed to reduce contact angle hysteresis and prevent

evaporation of liquid. An appropriately designed gap or channel height between the top and bottom substrate is essential to avoid the short circuit of electrode through the surrounding medium. For simplicity, we only consider a perfect model of parallel-plate capacitor of interfaces of three dielectric regions parallel to the substrates with a negligible morphological influence of droplet and electrode in electrical field.

Assuming an applied potential of V_0 across the substrates, the corresponding electrical field E in any of the dielectrics can be electrostatically represented as

$$E = \frac{V_0}{d_1 + \frac{\varepsilon_1}{\varepsilon_2}d_2 + \frac{\varepsilon_1}{\varepsilon_3}d_3} = \frac{V_0}{\sum_{i=1}^{3}\frac{\varepsilon_1}{\varepsilon_i}d_i} \qquad (2.3)$$

Here ε_i and d_i are the dielectric constant and dielectric thickness respectively for each dielectric region. Assume the top and bottom solid insulation are identical, we can simplify the electrical field in surrounding medium E_{sm} as

$$E_{sm} = \frac{V_0}{d_1 + \frac{\varepsilon_1}{\varepsilon_2}d_2 + \frac{\varepsilon_1}{\varepsilon_3}d_3} = \frac{V_0}{d + \sum_{i=1}^{2}\frac{\varepsilon_{sm}}{\varepsilon_i}d_i} \qquad (2.4)$$

Here d and d_i are the gap depth or channel height and thickness of solid insulating layer respectively, ε_{sm} and ε_i are the dielectric constant of surrounding medium and solid insulation respectively. Consequently, the breakdown voltage of the surrounding medium as a function of the ratio of d_i/ε_i is depicted in Figure 2.6. Some typical values of d in both air ($\varepsilon=1.0$, $E_{ds}=3.0\times10^6$ V/m) and silicon oil ($\varepsilon=2.5$, $E_{ds}=15\times10^6$ V/m) were taken as the examples for demonstration. Applying a maximum operating voltage of 100 V, the minimum gap depth for silicon oil is less than 10 μm and it is about 35 μm for air.
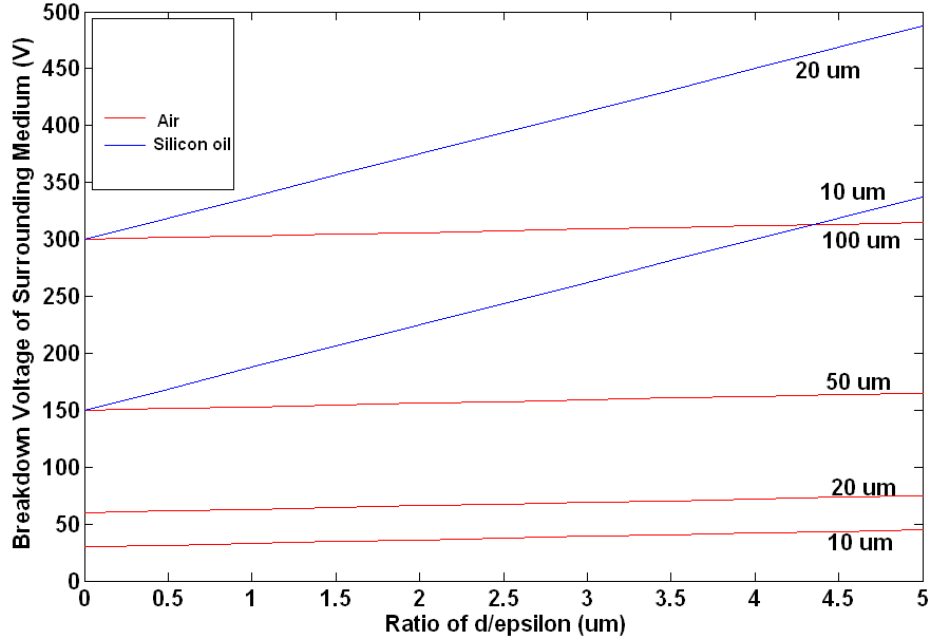
Fig. 2.6. Breakdown voltage of surrounding medium as a function of ratio of d/ε of insulator for some values of d.

Several ways to prevent dielectric breakdown have been discussed in Section 1.6.1. In addition, using SAM-coated electrodes could greatly reduce the applied voltage (~1.7 V) while obtain significant contact angle change [259]. However, the limited contact angle reversibility and specific working liquids narrow down the application scope of electrowetting on SAMs.

In summary, there is no ideal dielectric material of extremely high dielectric strength and dielectric constant. Certain trade-offs are needed when designing EWOD devices. For example, thinner dielectric layer needs low driving voltage which is the most common requirement for commercialized products. If larger electrowetting force generated by higher voltage is desired to achieve a large contact angle change, thicker dielectric layer should be employed.

2.4 Experimental Measurement of Contact Angle

This section documents the experimental results in measuring the contact angle for several dielectric materials. The accuracy of the measurement depends on factors such as composition of liquid droplet, water evaporation, droplet size / volume, humidity and temperature. Other factors such as air pressure, relative velocity between air and liquid droplet are negligible.

Liquid evaporation is almost inevitable for droplets in real world and it is also regarded undesirable for contact angle measurement. In microfluidics, liquid evaporation becomes significant for microdroplets.   Under typical experimental conditions (T=20°C and relative humidity is about 40%), the evaporation rate of water is about 3 μg/s [263-264]. In addition, water evaporation is against the increasing of humidity while significantly speeds up with air temperature rise-up. Therefore, in this case, each contact angle measurement of a typical size of liquid droplet (3-5 μl) has been completed within 2 minutes before water evaporation becomes significant at room temperature. The humidity in the lab is controlled at 40% and monitored during the experiment.

The significant effect of illumination was observed at the beginning of the experiment. A non-transparent plastic cover (like a box) was made to cover the goniometer and it only allows people to operate the goniometer in front. All illumination sources in the lab were turned off during the experiments to minimize the influence of illumination.

Only pure water and saturated sodium chloride (NaCl) were used as electrolytes for this study. 4-inch silicon wafers were firstly diced into 25 mm x 25 mm chips then sputter-deposited with Au thin films (2500 Å, with 100Å thick Cr underlayer). Totally four dielectrics, Parylene C, PDMS, Cytop™ and SAMs, which are able to serve as

prime insulators without additional hydrophobic coating, were prepared and tested. Teflon® AF 1600 was not considered because it normally serves as a thin hydrophobic layer instead of a prime insulator.

Parylene C thin films (2.25 μm thick) were deposited onto the Au-coated silicon chips by a customized parylene coating equipment.

PDMS (Sylgard® 184, Dow Corning) thin films were firstly prepared by mixing the base and curing agent at a ratio of 10:1 either by weight or volume (10 parts of base and 1 part of curing agent). Then, they were placed into a VWR vacuum oven to degas air bubbles at 101.6 kPa for 30 mins. After that, PDMS was dispensed onto Au-coated silicon chips and spin coated at 2000 rpm, and finally cured at around 150°C for 1 hr. Its thickness was about 38.2 um thick measured by a surface profilometer.

Cytop™ (TL809M, Asahi Glass Co. Ltd.) was deposited onto Au-coated silicon chips by spin coating at 2000 rpm with a ramp rate of 500 rpm. Then, they were cured at 60° C for 30 mins. The thickness is about 950 nm.

A hexadecanethiol ($C_{16}H_{34}S$, from Fluka) self-assembled monolayer was formed by immersing the Au-coated silicon chips in 1 mM hexadecanethiol (15.28 μl) in ethanolic solution (50 ml) sealed in a glass beaker placed in a fume hood for 12 hours. Then the monolayer was thoroughly rinsed with ethanol and its thickness was measured at about 24Å by a variable angle spectroscopic ellipsometer (WVASE32, J. A. Woollam Co. Inc.).

Figure 2.7 schematically shows the contact angle measurement of EWOD in open air using a contact angle goniometer (model no. 100-00-220-S, Rame-hart Instrument Co.). 3-μl droplets were dispensed by a micropipette for each measurement to minimize the gravitational effects. A DC potential was applied between the Au electrode underneath the dielectric layer and a thin Au wire (25 μm in diameter)

dipping into the droplet. Each measurement was repeated 3 times using fresh droplets to eliminate the evaporation effect and trapped charges. The droplet images were recorded by a camera to calculate contact angle and analyze droplet shape by the software of DROPimage. An amp meter was used to monitor the dielectric breakdown. Figure 2.8 shows the images of water droplets on these dielectrics in the presence and absence of various applied potentials respectively.
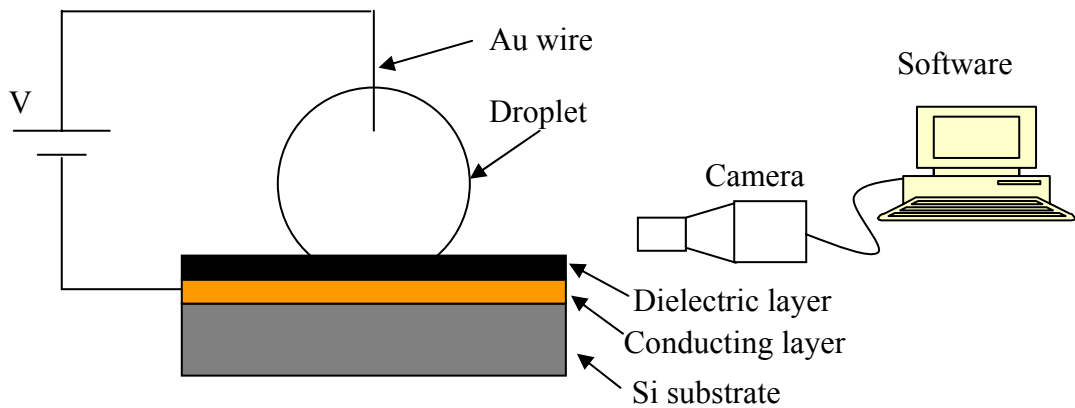
Fig. 2.7. The experimental setup for contact angle measurement of EWOD.
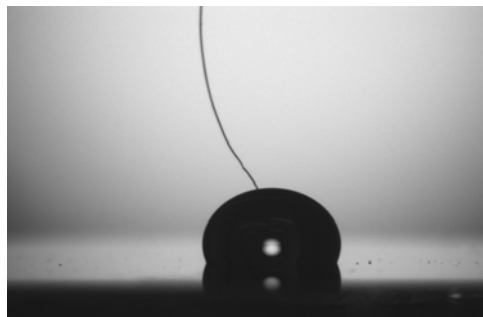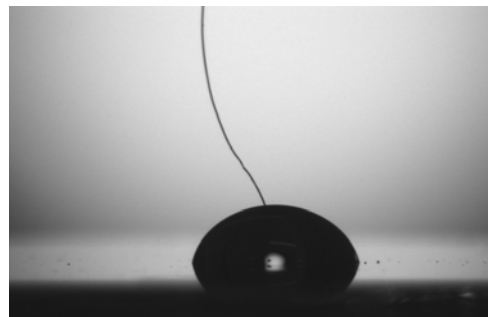
(a) Cytop™, 110° (0 V)   75° (65 V)

(b) Parylene C, 128° (0 V)   87° (125 V)

<div align="center">(c) PDMS, 120° (0 V)　　　　　　　　　105° (125 V)</div>

<div align="center">(d) SAM, 105° (0 V)　　　　　　　　　65° (6.5 V)</div>
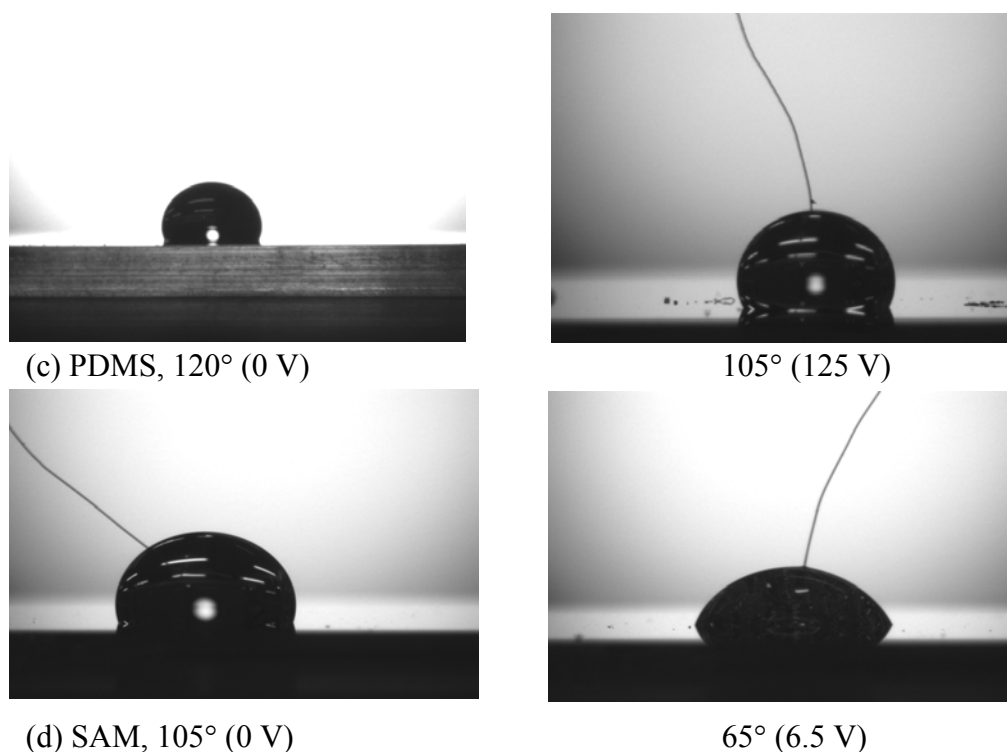
Fig.2.8. Contact angle of dielectrics with and without applied potentials.

Figure 2.9 plots the contact angle variation of water on the above-mentioned dielectrics as a function of applied voltage. A desirable contact angle modulation of 40° (from 128° to 88°) of Parylene C required about 120 V. The contact angle saturated at ~88° on this 2.25 um-thick Parylene C sample. A small contact angle modulation of 16°(117° to 101°) on a 38.2-um thick PDMS sample was obtained under a potential of about 140 V without observation of contact angle saturation. A moderate potential of 65 V was applied to achieve the contact angle variation of 35° (from 110° to 75°) with Cytop. Contact angle saturation was observed on this 0.95 um-thick Cytop sample when the potential was beyond 65 V.

A contact angle variation of 40° (from 105° to 65°) with SAMs could be obtained when applying a potential as small as 7.5 V, beyond which the contact angle saturated. However, it was observed that its hydrophobicity degraded significantly and the

surface became hydrophilic in 1-2 days. The instability and contact angle irreversibility make SAMs impossible to be applied in the device. Hence, SAMs as a prime insulator was not considered for the rest of contact angle measurement experiment.
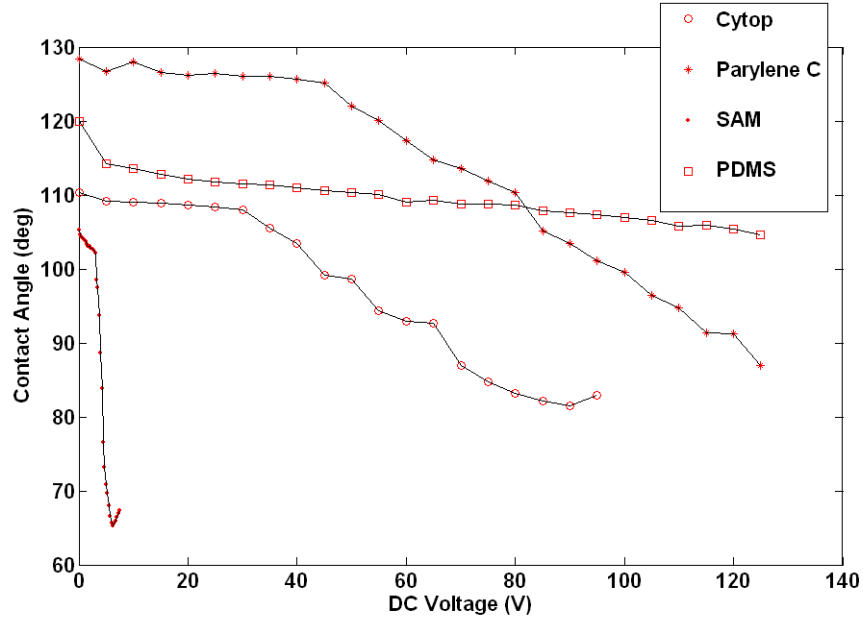
Fig. 2.9. Contact angle as a function of applied potential using water with the dielectrics of Cytop™ (950 nm), parylene C (2.25 um), SAMs (2.4 nm) and PDMS (38.2 um).

The EWOD dependence on polarity was tested using both saturated sodium chloride solution and water. The measurement results of Cytop™ and Parylene C denoted by solid markers and the theoretical prediction by the Young-Lippmann equation represented by solid line are shown as Figure 2.10(a) and (b) respectively. The theoretical model in Figure 2.10 can be directly derived from the Young-Lippmann equation (Equation 1.5) by

$$\theta = a\cos\left(\frac{\varepsilon_0 \varepsilon V^2}{2\gamma_{lv} d} + \cos\theta_0 \right) \qquad (2.5)$$
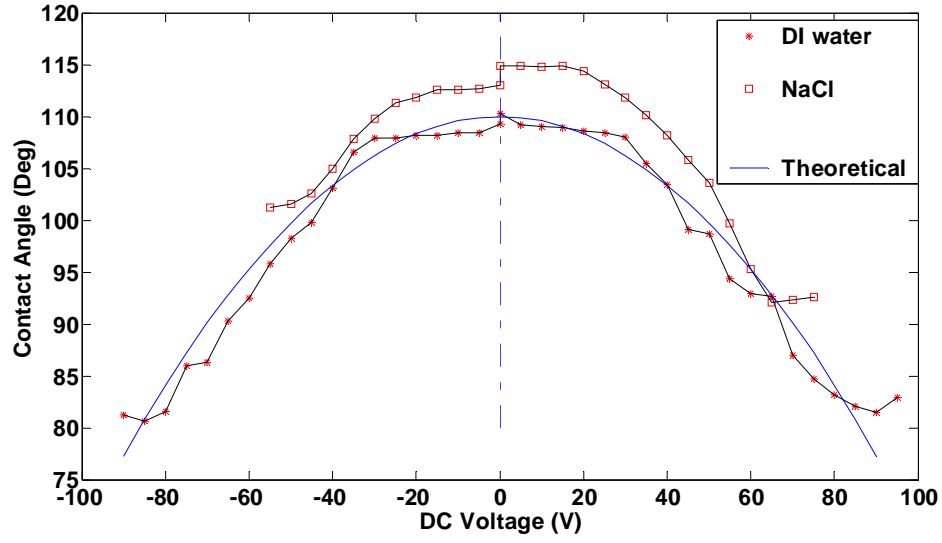
(a)
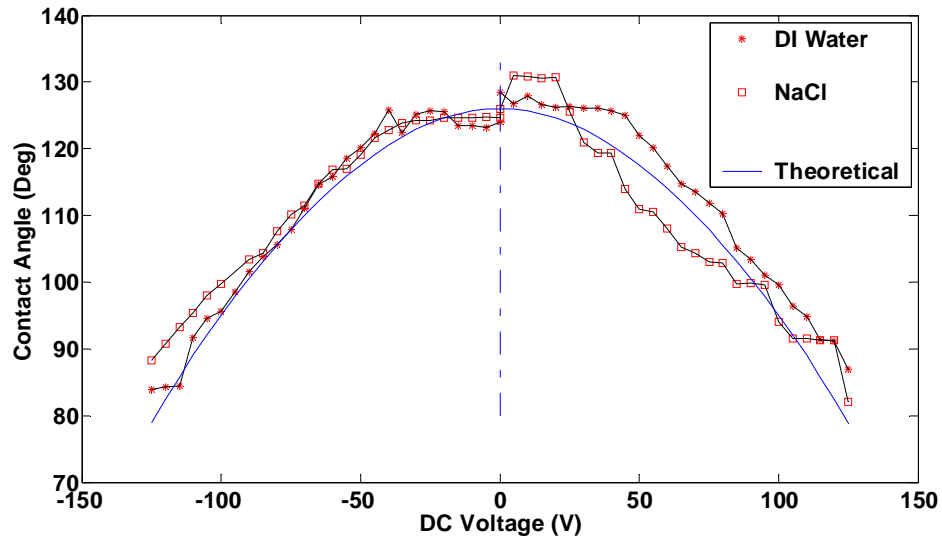
(b)

Fig. 2.10. EWOD dependence on polarity with (a) Cytop^{TM} and (b) Parylene C using water and saturated NaCl. Theoretical predication based on Equation 2.5 is represented by solid line.

The assumptions for derivation of this theoretical model include that the substrate is homogenous; liquid evaporation and gravity are negligible. Young-Lippmann equation is well-known and its derivation can be referred to Section 1.6. The experimental results follow the trend predicated by Equation 2.5 and a standard deviation of 1° for Cytop (with water) and 1.6° for Parylene C (with water) were

obtained respectively. Contact angle hysteresis of 1° and 3.6° were observed for Cytop and Parylene C respectively. Contact angle saturated with both of these materials, which was independent of the potential polarity. Both Cytop™ and Parylene C exhibit the independence of contact angle change on polarity with water and electrolyte, which is in agreement with literature [199] and theoretical predication.

The experiment on thickness dependence of contact angle modulation by electrowetting using water droplets have been performed on electrodes (Au) coated with dielectrics of varying thickness. These different thicknesses of Cytop and PDMS were achieved by spin coating from 2000rpm to 5000rpm with a ramp rate of 500rpm. Figure 2.11 shows the voltage required to change the contact angle of both materials experimentally, as well as theoretically by the following model, which is directly derived from the Young-Lippmann equation

$$V = \sqrt{\frac{2\gamma_{lv} d\left(\cos\theta_0 - \cos\theta\right)}{\varepsilon_0 \varepsilon}} \qquad\qquad (2.6)$$
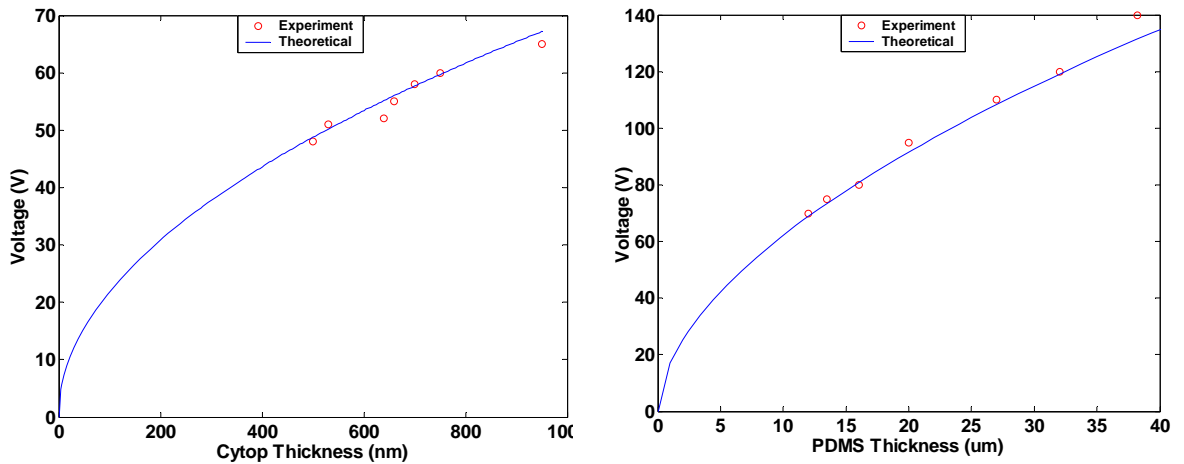
Fig. 2.11. The voltage required to generate a contact angle variation as a function of the dielectric thickness. The contact angle modulation is 35° for Cytop and 16° for PDMS. The solid line is calculated based on Equation 2.6 and the circle markers denote the experimental data.

The assumptions to derive Equation 2.6 are the same as that for Equation 2.5.The contact angle variation of Cytop was from 110° to 75° (35° modulation) and it was from 117° to 101° (16° modulation) for PDMS. The standard deviation was about 1.33 V for Cytop and 1.18 V for PDMS respectively. The results show good agreement with the theoretical predication up to the point where the contact angle saturates. Using spin coating method, it is difficult to make PDMS thickness thinner than 10 um because the maximum spinning speed (about 5000-6000 rpm) has been reached. The thickness of Cytop was achieved above 500nm, which was thicker than the minimum thickness of 330nm to avoid the dielectric breakdown.

Figure 2.12 shows the contact angle reversibility of Cytop™ as a dielectric (700 nm thick) for EWOD using water droplet and Figure 2.13 shows the corresponding experimental images of the reversible contact angle of water droplet in the experiment. Contact angle hysteresis varies from 3.2°-4°, which is acceptable for EWOD devices. Other tested dielectrics (SAM, parylene C, and PDMS) present uncompetitive or even poor reversibility of contact angle changes for both water and the electrolyte solution.

Comparing the tested dielectrics, Parylene C requires quite high driving voltage to obtain a desirable contact angle modulation of 40°. It is difficult to be patterned by dry/wet process in microfabrication. Hence, it is not suitable to be applied in the proposed device. PDMS presents a small contact angle variation of only 16° under an extremely high potential of 140 V. Microstructure of PDMS can not be patterned successfully by dry/wet process like RIE etching. In contrast, a desirable contact angle modulation of Cytop (35°) can be obtained under relatively low applied potential (65 V). Cytop also exhibits good reversibility of contact angle and patternability with dry etching process.
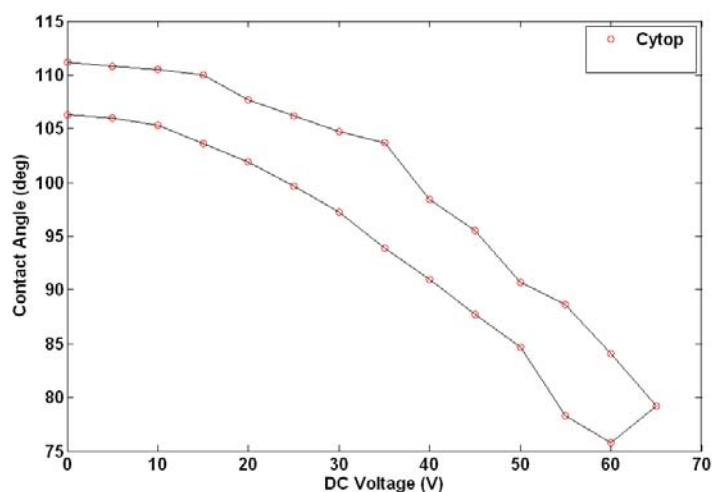
Fig. 2.12. The reversibility of contact angle of Cytop™ film
with a contact angle hysteresis of 3.2°-4°.
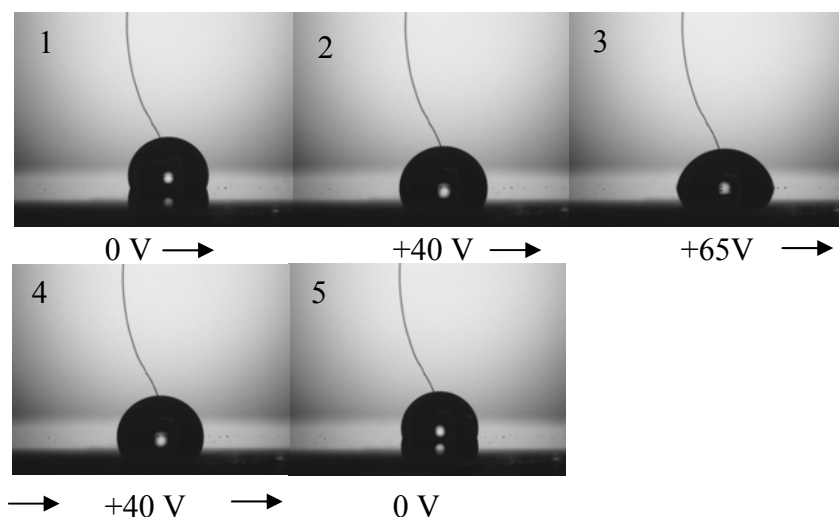
Fig. 2.13. Experimental images of the reversible contact angle
of water droplet on top of Cytop™.

In summary, Cytop™ is suitable as a dielectric material for EWOD with a good combination of mechanical, electrical, chemical and thermal properties. Its competitive surface properties including better reversibility of contact angle, lower contact angle hysteresis and larger contact angle changes with moderate actuation voltage make it suitable for EWDO systems and devices for commercialization.

CHAPTER 3

DESIGN AND ANALYSIS OF A HYDROPHOBICITY CONTROLLED MICROFLUIDIC DISPENSER

In this chapter, the conceptual design, working principles and advantages of an EWOD-based microfluidic dispenser having in-built flow volume metering ability are discussed. This chapter briefly discusses the hydrodynamic behaviour of liquid column dominated by the surface tension forces. Understanding the dynamics of EWOD is important to predict and evaluate the performance of the device performance. The EWOD device performance depends heavily on the operation conditions. Moreover, a desirable model to obtain scaling factors in terms of device performance has been established for further miniaturization. Theoretical studies have been carried out to interpret the dynamics of contact angle, surface charge built-up process and the net force acting on the interface of liquid-vapour. A prototype with key feature sizes in the micrometer scale was fabricated in a manner similar to MEMS fabrication. The prototype was also used for proof-of-concept experiments.

3.1 Concept of the Microfluidic Dispenser

The present innovative microfluidic dispenser, of which the motivation and scope are mentioned in Section 1.8, is particularly useful to dispense ultra-small volume of varying liquid columns using controlled hydrophobicity actuation features in a microchannel.

Figure 3.1 schematically shows how this microfluidic dispenser can be incorporated into a lab-on-a-chip chemical analysis system mentioned earlier in Section 1.8, which incorporates multi aspects of biology and chemistry laboratories together on a small chip. Electrode arrays are fabricated along the fluid path in the main and branch microchannels. The hydrophobic pads are patterned and coated alternatively on the bare electrodes.
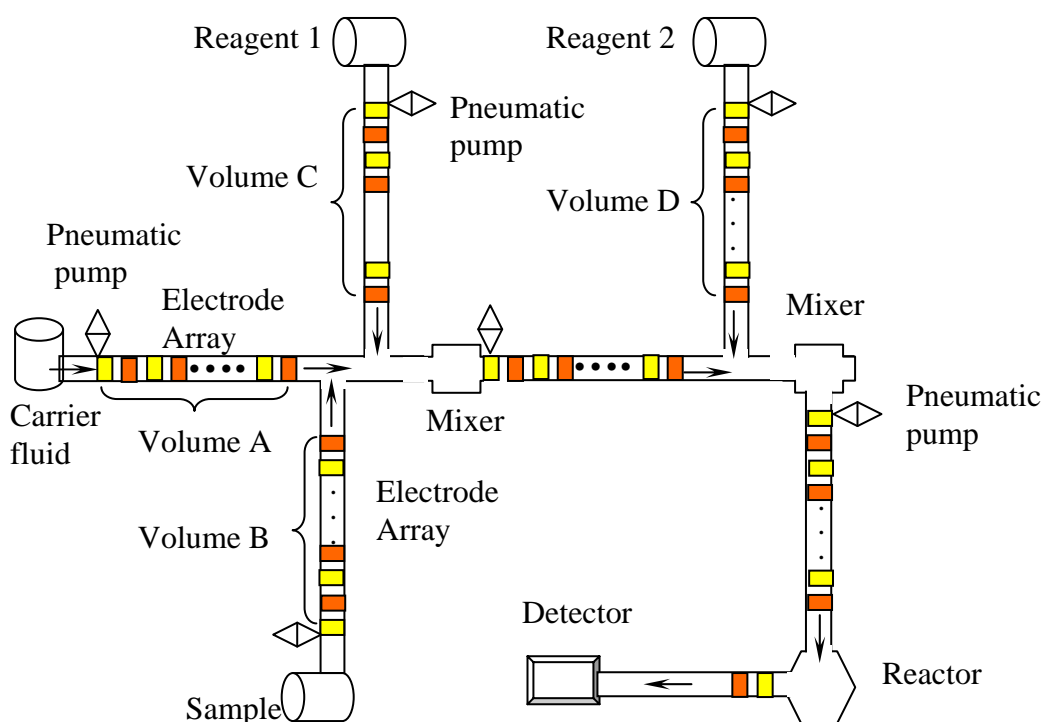
Fig. 3.1. The schematics of the analysis procedure of a flow injection analysis. The electrode arrays are fabricated along the fluid path in main and branch channel. A hydrophobic layer (denoted by ■), is alternatively coated on the bare electrode (denoted by ▢).

The carrier flow propagates into the main channel under capillary force till it stops at the 1st hydrophobic coated electrode. Applying a potential difference across the adjacent electrodes (the 1st bare and hydrophobic coated electrode), an electrostatic force will be generated at the liquid meniscus to pull the carrier fluid column till it stops at the next hydrophobic coated electrode along the main channel. As the cross section area of the channel is constant, the fluid volume can be measured by the numbers of electrodes passed by the liquid meniscus. When a desirable volume A of carrier fluid is reached, air pressure is induced in the main channel, which is allocated at the first bar electrode, to cut off the liquid column and push the carrier column of volume A into the first mixer. Using the same method, a sample fluid of volume B and reagent 1 of volume C are delivered into the 1st mixer.

Then, the fluids are actuated in the same way and pass further down the main channel and mix together with reagent 2 in 2nd mixer. Reagent 2 is also actuated and delivered with a prescribed volume D in the same manner as mentioned earlier. Hence, these fluids are mixed by a pre-defined volume ratio, which is necessary for the analysis. After that, the mixture is actuated again to run through a reaction chamber and a detector for further analysis. It should be noted that, the volume of the mixtures, which will be delivered for further analysis, still can be precisely controlled by the electrode arrays in between mixers, reaction chambers and detectors. Finally, the amount of ammonia can be calculated based on the measurement result, which has been introduced in Section 1.8.

This study will focus on the liquid dispensing behavior of this hydrophobicity controlled microfluidic dispenser and the behavior of the pneumatic pump is not included. The detailed study of this microfluidic dispenser is presented in the following sections.

The device consists of a microchannel which is connected to a liquid reservoir. Hydrophobic pads are made along the inside wall of the microchannel as shown in Figure 3.2. These hydrophobic pads become hydrophilic by applying an electric field across the hydrophobic layers. Gold conductive electrodes are formed in between the hydrophobic pads and exposed to the liquid in order for it to be in contact with the liquid, unlike the electrodes which are underneath the hydrophobic coating.
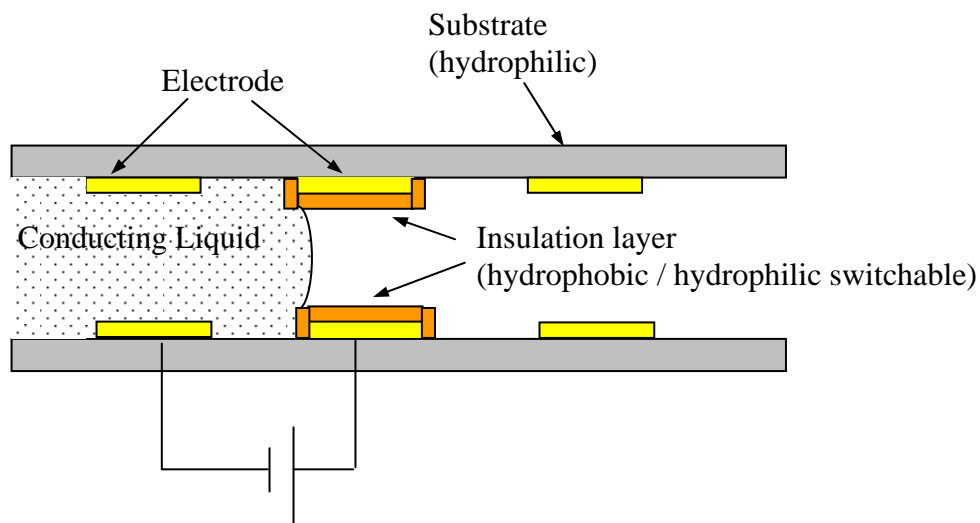
Fig. 3.2. The schematic of cross-section view of dispenser.

The dispensing sequence is shown in Figure 3.3. The electrode underneath the hydrophobic pad is connected to the positive terminal of the power supply while the exposed electrode is connected to the negative terminal. Initially, the liquid column propagates into the channel under capillary force due to the hydrophilic surface of the inner wall (Figure 3.3(a)). When no potential is applied, the liquid column stops at the first hydrophobic pad (Figure 3.3(b)). When an electrical potential is applied, as shown in Figure 3.3(c), the hydrophobic pad becomes hydrophilic and the meniscus of liquid changes from convex to concave transiently because of ion separation induced by the applied potential (Figure 3.3(c)). The liquid column starts to propagate in the channel

again until it reaches the next hydrophobic pad, at which point the liquid column stops propagating and the meniscus becomes convex (Figure 3.3(d)). Applying potential again, it starts another dispensing cycle (Figure 3.3(e)). This invention has been patented with an international publication no. WO 2006/115464 A1 [265].
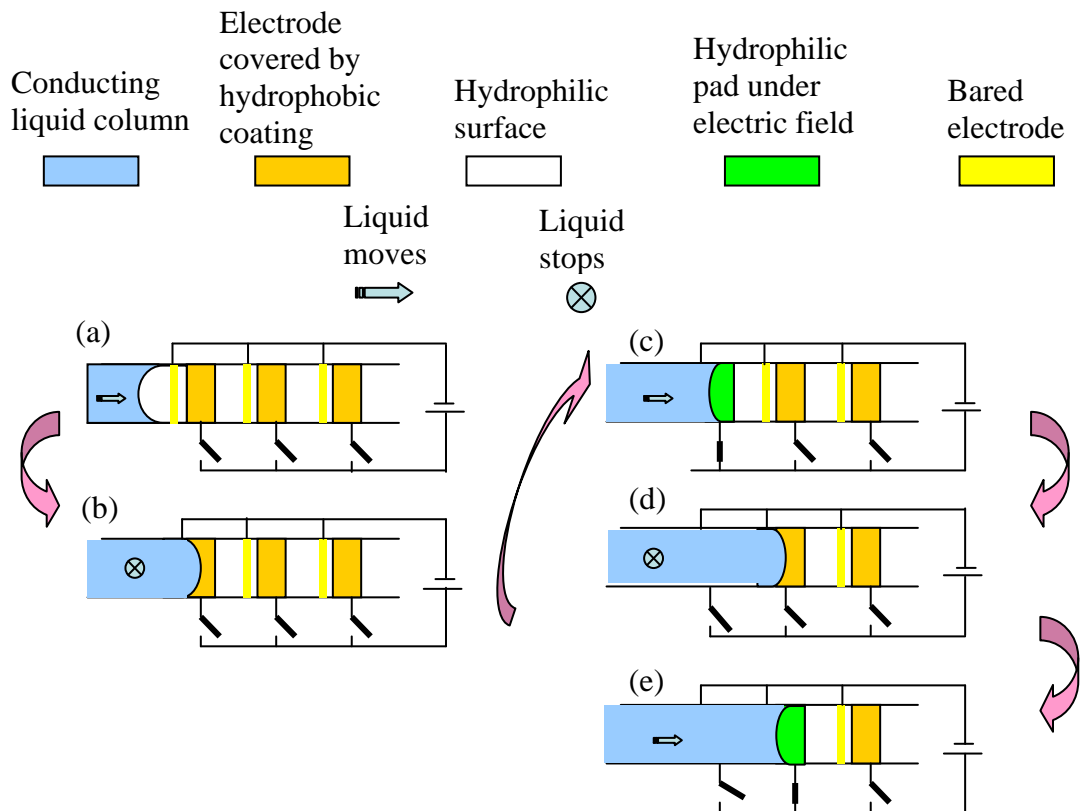
Fig. 3.3. Dispensing sequences.

This microfluidic dispenser exhibits several advantages. It does not employ actuators that would limit minimum device sizes, and therefore can be miniaturized as desired for the particular application and therefore is suitable for chip scale fluidic systems. The limitation of miniaturization is only imposed by the limitations in current lithography techniques (*i.e.*, the smallest feature size that can be defined using current lithography techniques). For example, if the lithography process used in making a

device is capable of defining 100 nanometer (nm) features, then the size of features of the device is on the order of few hundred nanometers and the device is capable of dispensing quanta of liquids as small as a few atto liters. The voltage required to dispense liquids using controlled hydrophobicity actuation features of the present invention is advantageously about 20 Volts. Furthermore, this dispenser includes an in-built metering feature that is useful to deliver a measured volume of liquid. This measured volume can be selected to be in the range of a few milliliters to a few attoliters. Since the cross section of the microchannel is a constant, the delivered fluid volume can be calculated if we know the numbers of electrodes already passed by fluids. This so-called in-built metering feature can be realized using a multiplexer. Moreover, the liquid volume can be varied and controlled in sub-microliter or even smaller by a combination of the electrode arrays, multiplexer and a pneumatic pump. The new micro/nano fluidic device design presents a variety of new applications. For example, the low power consumption and low voltage requirements of this device make it very attractive for applications that require an ultra miniature metering microfluidic device which operates at a low voltage. Last but not least, the liquid column propagates due to capillary force and it automatically gets rid of any unwanted air bubbles present in the system.

3.2 The Hydrodynamics of Liquid-solid Interfacial Tension

The surface charge density of the accumulated charges at the liquid-solid interface influences both of the surface tension and electrostatic force. To study it, let's firstly look at the free charges carried by ions in an electrified liquid. Free charge density and ion concentration are related as:

$$\rho_s = \sum_k e z^k n^k \qquad (3.1)$$

here e is the elementary charge, z^k is the valence of the kth species whose concentration is n^k. The gas phase (i.e., air) as an insulator and the liquid phase (i.e., ionized solution) as a leaky dielectric are involved in this case. In the regions of uniform conductivity (κ=constant), the potential distribution of the electrostatic field in the regions of uniform conductivity (conductivity is constant) is governed by Equation 3.2:

$$\nabla^2 V = 0 \qquad (3.2)$$

The bulk free charge density is considered zero in the liquid. Thus, the electric potential V is irrotational and divergence-free throughout the field. An electric field discontinuity normal to the liquid-gas interface is generated by the interfacial charge density ρ_s. The accumulation rate of the interfacial charge density ρ_s is given by the continuity condition for conservation of charge expressed via Ohm's law:

$$\vec{n} \cdot \left(\varepsilon_l \nabla V_l - \varepsilon_g \nabla V_g \right) = \rho_s \qquad (3.3)$$

where $\vec{n}$ is the unit normal vector of the interface pointing towards air, ε is the dielectric constant, subscript l and g indicate the liquid phase and gas phase, respectively. Hence, the interfacial charge density is given by:

$$\frac{d\rho_s}{dt} = -\vec{n} \cdot \sigma \cdot \nabla V_l \qquad (3.4)$$

where d/dt is the Lagrangian derivative, and σ is the conductivity of the liquid. The accumulation process of the interfacial charge is given by Equation 3.4.

Using FlexPDE 5 (a multi-physics finite element solution software for partial differential equations from PDE Solutions Inc.), Eq. 3.3 and Eq. 3.4 were solved numerically. As the thickness of the electrodes (500 nm) is too small compared to the channel height (20 μm), it is negligible in the simulation. The electrode width is 20 μm

and the electrode gap is about 40 μm. Figure 3.4a shows the electrical potential distribution (under 20V) in the absence of liquid in the channel and Figure 3.4b shows the distribution of the magnitude of electrical field, respectively.
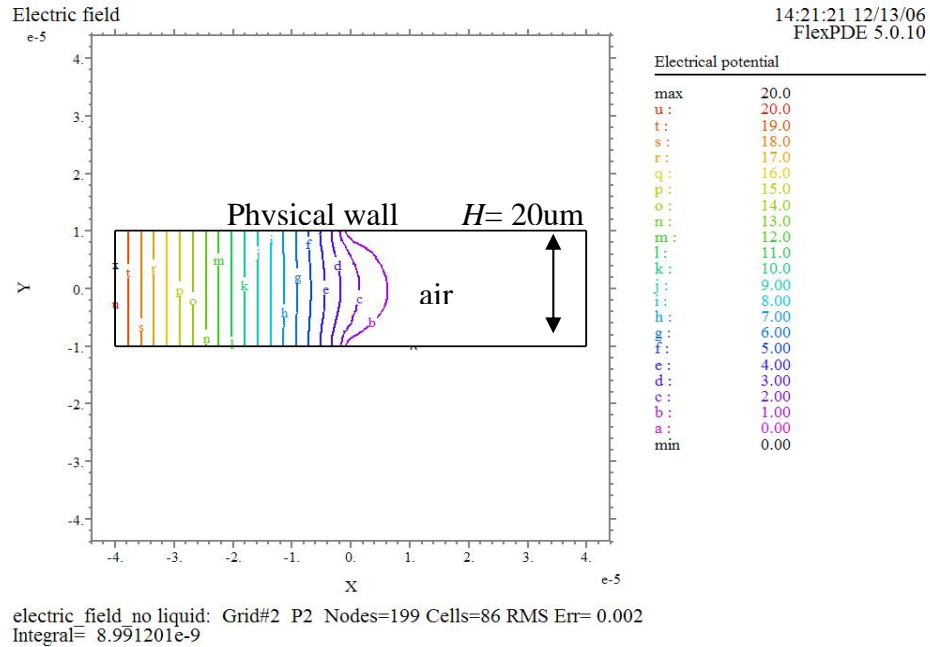
Fig. 3.4a. The electric potential distribution in the absence of liquid.
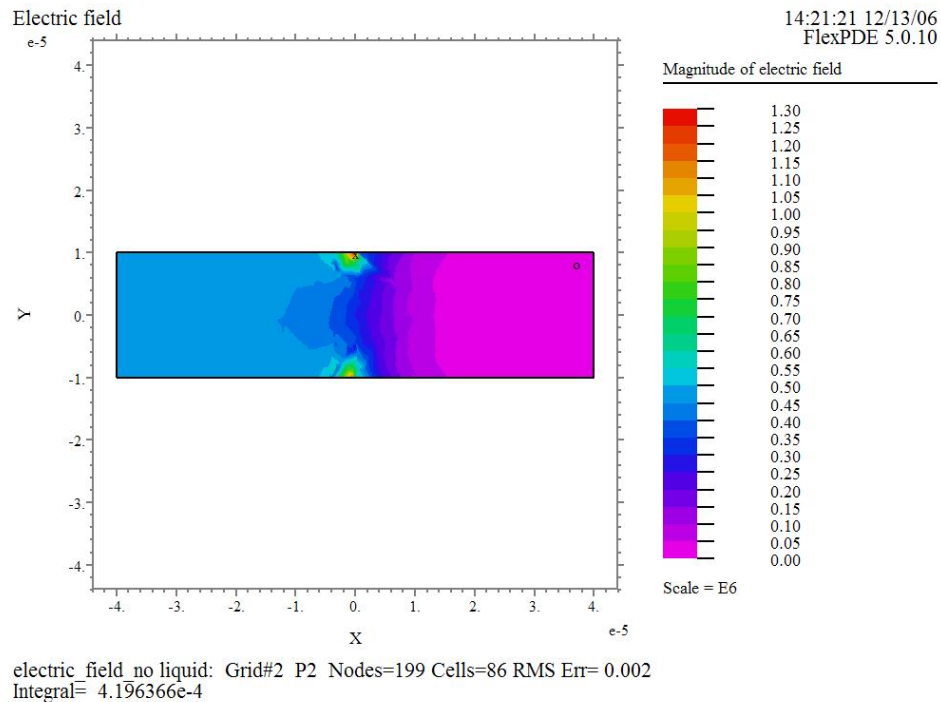
Fig. 3.4b. The distribution of the magnitude of electric field in the absence of liquid.

The liquid propagates in the channel and then it stops at the first hydrophobic pad. Applying 20V, the surface charges build up at the meniscus. Figure 3.5a and Figure 3.5b illustrate the electrical potential distribution and the distribution of the magnitude of electrical field with liquid under 20 V, respectively. Figure 3.6a and Figure 3.6b show the electrical potential distribution of surface charges and the magnitude of electrical field distribution, respectively. The boundary conditions are shown in Figure 3.5a and Figure 3.6a respectively. The detailed program scripts for the above-mentioned simulations using FlexPDE 5 are listed in Appendix A.
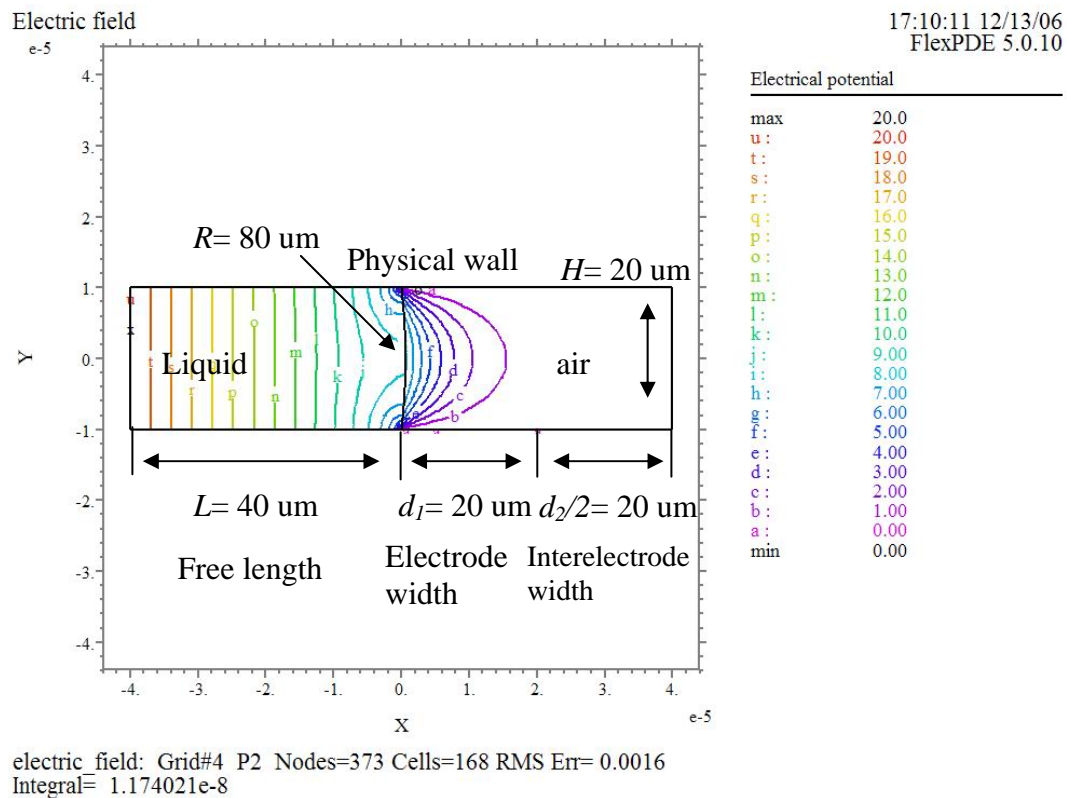
Fig. 3.5a. The electric potential distribution with liquid under 20V.
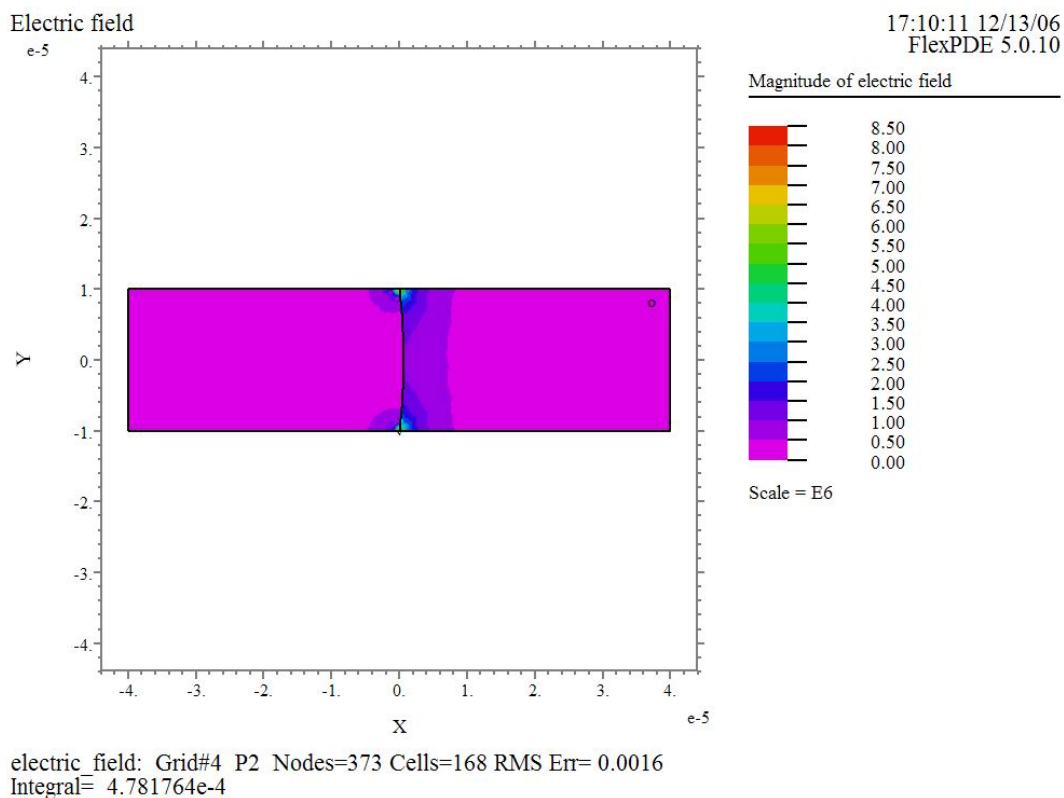
Fig. 3.5b. The distribution of the magnitude of electric field with liquid under 20V.
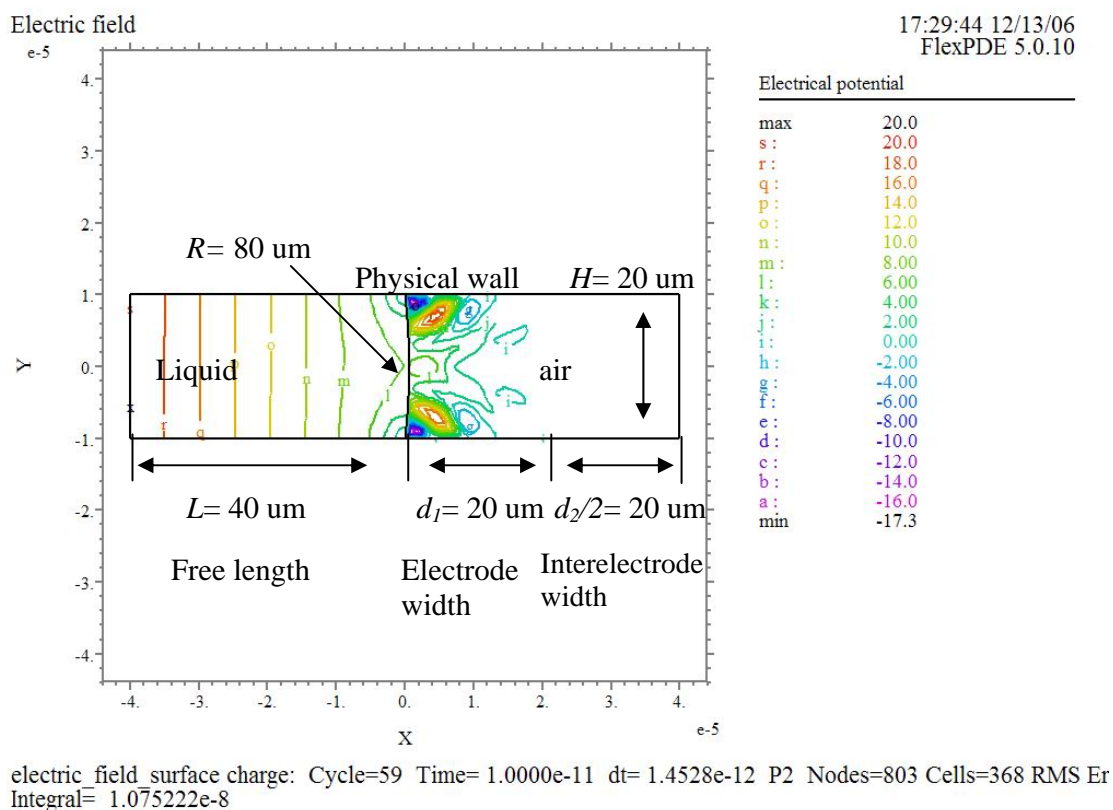
Fig. 3.6a. The electric potential distribution of surface charges under 20 V.
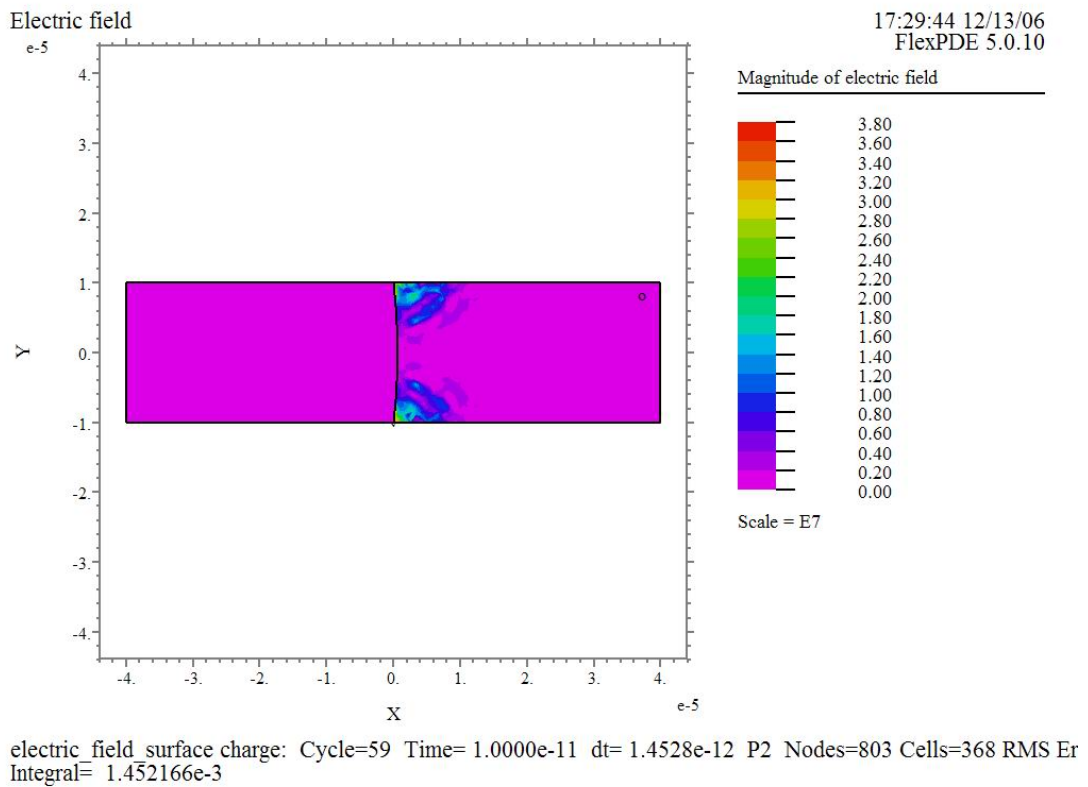
Fig. 3.6b. The distribution of the magnitude of electric field of surface charges under 20 V.

3.3 The Electrostatic Force Acting on Liquid Column

EWOD originates from a free charge distribution at the liquid-solid interface and generates an electrostatic force on the tri-phase contact line on the electrodes to pull the liquid forward, referring to Figure 3.7. This electrostatic force is resulted from the accumulation of free surface charges induced by the non-uniform electrical field near the contact lines on the electrodes. The electrostatic force acts on the tri-phase contact line, normal to the liquid-vapor interface, and points away from the liquid column.

The electrostatic force acting on the electrified liquid surface with negligibility of the osmotic contributions is given by,
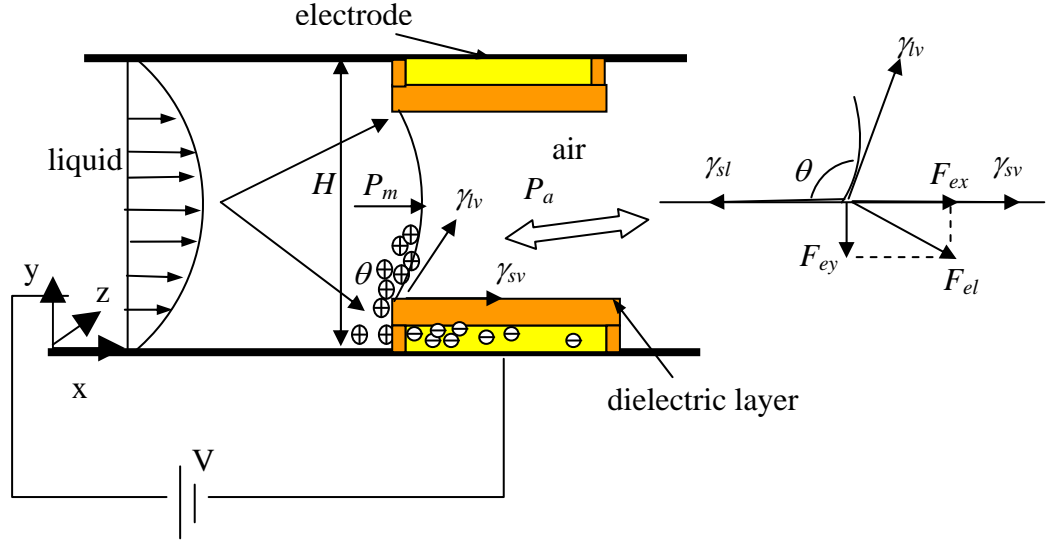
Fig. 3.7. Charge distribution upon potential and electrostatic force
pulling on the meniscus.

$$F_{el} = \int_{A_{lv}+A_{ls}} T \cdot \vec{n} dA \qquad (3.5)$$

Here, A is the interface area with the subscripts l, v and s indicating liquid, vapor and

solid, $\vec{n}$ denotes the unit normal vector and T is the Maxwell stress tensor, which can

be written as

$$T_{ij} = \varepsilon \left(E_i E_j - \frac{1}{2} \delta_{ij} E^2 \right) \qquad (3.6)$$

Here, δ_{ij} is the Kronecker delta and i, j=x, y, z. At the surface of conductive liquid, the

tangential electrical field vanishes and the normal component relates to the surface

charge density as

$$\rho_s = \varepsilon \vec{E} \cdot \vec{n} \qquad (3.7)$$

Note that $\vec{E}$ vanishes in bulk liquid. Using Einstein summation convention, the net

force acting on the liquid can be obtained by

$$F_{el} = \int_{A_{lv}+A_{sl}} \frac{1}{2} \varepsilon E^2 \cdot \vec{n} dA = \int_{A_{lv}+A_{sl}} \frac{1}{2} \varepsilon E \rho_s dA \qquad (3.8)$$

From Equation 3.8, a non-vanishing net electrostatic force was excited by electric field on the liquid surface, which is perpendicular to the surface and pointing towards vapor (air). Thus, it is a negative pressure contribution to the total pressure on the liquid. The magnitude and direction of the net force are dependent on the electric field distribution as a geometrical function of the liquid.

The electrostatic field near the edge area was analyzed by Vallet *et al.* [218] by considering this edge area of liquid as an infinite planar wedge as shown in Figure 3.8. In Figure 3.8, $\omega = \tau + i\pi$ is the complex coordinates of the transformed plane, τ and υ are the transformed coordinates. l is the length from the apex of the wedge along the liquid-vapor interface (A_{lv}) and the differential relation between l and the complex coordinate τ can be established as
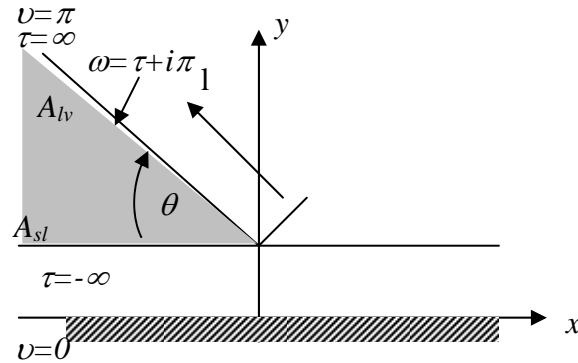
Fig. 3.8. Edge contribution to the electrostatic field [218].

$$dl / d\tau = \frac{d}{\pi} \left| e^{\tau} - 1 \right|^{\alpha} \tag{3.9}$$

The surface charge density is obtained as following [218],

$$\frac{\rho_s}{\rho_0} = \frac{1}{\left| \left(e^{\omega} + 1 \right)^{\alpha} \right|} \tag{3.10}$$

Here, ρ_0 denotes the charge density at the liquid-solid (dielectric) interface far from the three-phase contact line and equals to $\varepsilon V/d$. α relates to the contact angle θ of the

liquid column as $\alpha = 1 - \theta / \pi$. Thus, substituting Equation 3.9 and 3.10 into Equation 3.8, the net electrostatic force acting on the upper side of the wedge, i.e. the liquid-vapor interface, due to the Maxwell stress, can be obtained

$$F_{el} = \int_{A_{lv}} \frac{\rho_s^2}{2\varepsilon} dl = \frac{\varepsilon V^2}{2d^2} \int_{A_{lv}} \frac{1}{\left(e^\tau - 1\right)^{2\alpha}} dl = \frac{\varepsilon V^2}{2\pi d} \int_0^\infty \frac{1}{\left(e^\tau - 1\right)^\alpha} d\tau \qquad (3.11)$$

Let $\zeta = e^\tau - 1$ and substituting it into Equation 3.11, the net electrostatic force acting on the liquid-vapor interface and directing away from the liquid can be further developed as

$$
\begin{aligned}
F_{el} &= \frac{\varepsilon V^2}{2\pi d} \int_0^\infty \frac{1}{\left(e^\tau - 1\right)^\alpha} d\tau = \frac{\varepsilon V^2}{2\pi d} \cdot \int_0^\infty \frac{1}{\zeta^\alpha} d\left(\ln(\zeta + 1)\right) \\
&= \frac{\varepsilon V^2}{2\pi d} \cdot \int_0^\infty \frac{\zeta^{\theta/\pi - 1}}{\zeta + 1} d\zeta = \frac{\varepsilon V^2}{2\pi d} \cdot \frac{\pi}{\sin \theta} \\
&= \frac{\varepsilon V^2}{2d \sin \theta}
\end{aligned}
\qquad (3.12)
$$

Hence, the horizontal (F_{ex}) and vertical component (F_{ey}) can be obtained through decomposition of this net force respectively,

$$F_{ex} = F_{el} \sin \theta = \frac{\varepsilon V^2}{2d} \qquad F_{ey} = F_{el} \cos \theta = \frac{\varepsilon V^2}{2d} \cot \theta \qquad (3.13)$$

It is found that the horizontal component F_{ex} is independent of the contact angle while adjustable with applied potentials when the dielectric thickness and permittivity are kept constant. This force pulls the liquid meniscus forward till it is balanced with the surface tension force. Referring to Figure 3.9, a macroscopic balance of the horizontal forces at the three-phase contact line for a very small volume of liquid can be achieved,

$$\gamma_{lv} \cos \theta = \gamma_{sl} - (\gamma_{slv} + F_{ex}) = \gamma_{sl} - (\gamma_{slv} + \frac{\varepsilon V^2}{2d}) \qquad (3.14)$$

Equation 3.14 shows the consistency of this result with the Young-Lippmann equation. The last term ($\varepsilon V^2/2d$) of Equation 3.14 comes from the Maxwell stress. On the other hand, it is implicated that the vertical component F_{ey} of the net electrostatic force increases with $cot\theta$ when contact angle decreases. From the mechanical viewpoint, this downward electrostatic force tends to resist the decreasing of contact angle driven by the horizontal component F_{ex}. That is, with the reduction of contact angle caused by the horizontal force F_{ex}, the vertical component F_{ey} will becomes larger till it reaches a certain threshold value, at which F_{ey} is large enough to resist the contact angle reduction. This could be a new explanation for the origin of contact angle saturation, the mechanism of which has been explored by researchers [198,206,218] in the past a few years. In addition, a small change of contact angle $\Delta\theta$ has to consume a considerable amount of energy which is implemented to overcome the vertical component of the electrostatic force.

The horizontal component of the electrostatic force given by Equation 3.14 has common features with line tension effect suggested by R. Digilov (Equation 33 in [266]). Figure 3.9 shows the three-phase contact line equilibrium in the presence of the electric charges [266].
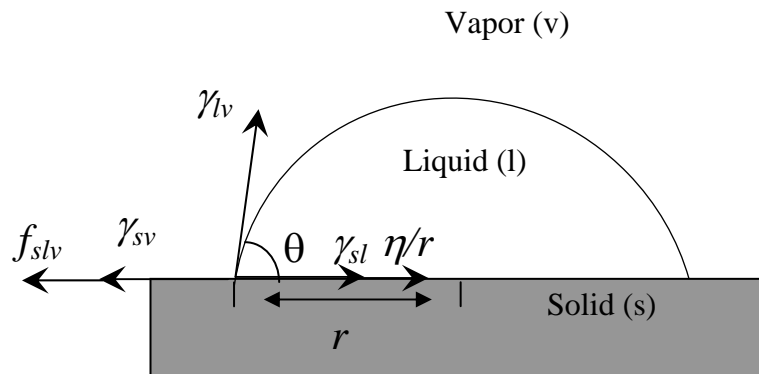
Fig. 3.9. The three phase contact line equilibrium in the presence of electric charges, which was presented by Digilov [266]. η is the line tension, r is the radius of the curvature, f_{slv} is the electric driving force of the wetting.

Here, η is the line tension, r is the radius of the curvature, f_{slv} is the electric driving force of the wetting. R. Digilov considered that the excess electrostatic energy per unit length of the three phase contact line was given by

$$n_{slv} \delta U_{slv} = n_{slv} q \delta \varphi_{slv} = \chi_{slv} \delta \varphi_{slv} \tag{3.15}$$

where, n_{slv} is the line density at the three phase contact line, U_{slv} is the excess electrostatic energy at the three phase contact line, $\chi_{slv}=n_{slv}q$ is the line density of the electric charges and $\delta \varphi_{slv}$ is the change of the electrostatic potential on the three phase contact line. R. Digilov generated the Young equation in the presence of charges

$$\sum_{j} \gamma_{j} \delta t_{j} + \left(\frac{\eta}{r} + \frac{\partial \eta}{\partial r} \right) \delta r + n_{slv} \delta U_{slv} = 0 \tag{3.16}$$

Where, $\Sigma_{j}\gamma_{j}\delta t_{j}$ is the Young term, η/r is the line tension contribution, $\partial\eta/\partial r$ defines the curvature dependence of the line tension and the last term is the electrostatic contribution due to the presence of the line charges. Substituting Eq. 3.15 into Eq. 3.16 and opening the summation sign, one has

$$\gamma_{sv} - \gamma_{sl} = \gamma_{lv} \cos\theta + \left(\frac{\eta}{r} + \frac{\partial \eta}{\partial r} \right) \frac{\delta r}{\delta t_{sl}} + \chi_{slv} \frac{\partial \varphi_{slv}}{\partial t_{sl}} \tag{3.17}$$

Here, δt_{sl} is the virtual displacement of the contact line, $\delta r/\delta t_{sl}=\cos\beta$, where β is the angle of inclination. For a flat substrate (this case) $\delta r/\delta t_{sl}=\cos\beta=1$. The derivative $\delta\varphi_{slv}/\delta t_{sl}=E_{slv}$ is the strength of the electrostatic field at the wetting line. Substituting these relationships in Eq. 3.17 and disregarding $\partial\eta/\partial r$, one obtains Young's equation in the presence of charges

$$\gamma_{sv} - \gamma_{sl} = \gamma_{lv} \cos\theta + \frac{\eta}{r} - \chi_{slv} E_{slv} \tag{3.18}$$

where $f_{slv} = \chi_{slv} \, E_{slv}$ is the specific electric driving force of the wetting. In the absence of the charges on the triple line, Eq. 3.18 becomes Youngs equation with line tension correction

$$\gamma_{sv} - \gamma_{sl} = \gamma_{lv} \cos\theta + \frac{\eta}{r} \tag{3.19}$$

The above derivation of the electrowetting force elaborated by Digilov is different from that was done in this work. The line tension of Digilov was caused by the excess free energy at the three-phase contact line while the electrostatic contribution was from the presence of line charges. It separately considered the contribution from the electrostatic pressure.

Based on the modified Pellat apparatus to an EWOD configuration, T. B. Jones [267] analyzed the electrostatic driving force acting on the liquid using different methods. He provided a general approach of calculating virtual displacements from lumped parameters in the electromechanics framework. The geometry used to calculate the force of electric origin is given in Figure 3.10.
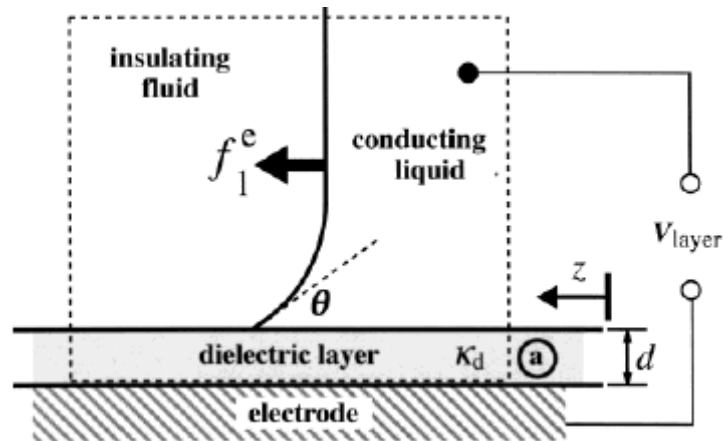
Fig. 3.10. Geometry used to calculate the force of electrical origin per unit length of the contact line of a conducting liquid adjacent to a coated electrode [267]. The dashed line defines a closed surface. Note that no precise location for the electrical force was specified.

In T. B. Jones's method, the system capacitance per unit length was given as

$$c(z) = \frac{k_d \varepsilon_0 z}{d} + c_0 \tag{3.20}$$

Here, k_d and d are the dielectric constant and thickness of the dielectric layer, respectively; z is the length in z-direction, c_0 is a constant. Using standard methods, the coenergy per unit length w_e' was then given by

$$w_e' = c(z)V_{layer}^2 / 2 \tag{3.21}$$

and the net electrostatic driving force, also per unit length of the contact line, was equal to the partial derivative of the coenergy with respect to z,

$$f_1^e = \frac{\partial w_e'}{\partial z} = \frac{V_{layer}^2}{2}\frac{dc}{dz} = \frac{k_d \varepsilon_0 V_{layer}^2}{2d} \tag{3.22}$$

This force pulls the liquid surface from right to left as shown in Figure 3.9. This result is consistent with the expression of the horizontal force in Eq. 3.13.

Figure 3.11 shows the modified Pellat apparatus to illustrate the EWOD configuration in the work of J. Zeng *et al.* [268].
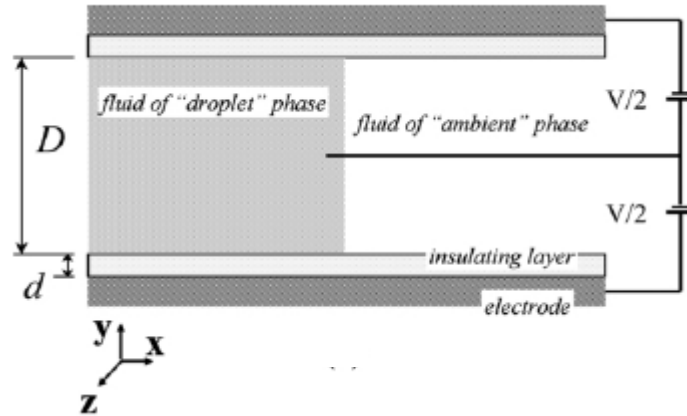
Fig. 3.11. The modified Pellat apparatus illustrates the EWOD configuration [268]. *D* is the width of the gap between the two insulating layers and *V* is the voltage difference between the two electrodes, *d* is the thickness of the insulating layers.

The droplet fluid is a conductor, the ambient fluid and the insulating layer are insulators with permittivity ε_a and ε_i, respectively. The two-fluid interface sustains

zero free charge since its normal is perpendicular to the electric field E. The free charge exists only at the droplet-insulator interface. For a given control volume, the electrostatic driving force can be calculated via

$$F^e = \nabla_\xi \int W dV \qquad (3.23)$$

where W is the volumetric density of the electroquasistance energy, the integral over the volume, and the gradient is with respect to ξ, the displacement of the material [269]. Application of Eq. 3.23 to the Pellat apparatus of EWOD configuration indicates that there exists: (1) no EHD force in the droplet bulk; (2) an EHD force at the two-fluid interface with a surface density is given by

$$f^{EWOD-I} = -\frac{\varepsilon_a V^2}{8d} \frac{\left(\dfrac{2d}{D}\right)^2}{\left(1 + \dfrac{2d}{D}\dfrac{\varepsilon_a}{\varepsilon_i}\right)^2} \qquad (3.24)$$

and (3) and EHD force at tri-phase contact line with a line density, denoted f^{EWOD-W} of, is given by

$$f^{EWOD-W} = \frac{\varepsilon_i V^2}{8d}\left(1 - \frac{1}{\left(1 + \dfrac{\varepsilon_i}{\varepsilon_a}\dfrac{D}{2d}\right)^2}\right) \qquad (3.25)$$

which is in plane with the droplet-insulator interface, perpendicular to the contact line, and point away from the droplet. However, in laboratory practice, d is much smaller than D; therefore, f^{EWOD-I} is usually negligible and f^{EWOD-W} is reduced to

$$f^{EWOD} = \frac{\varepsilon_i V^2}{8d} \qquad (3.26)$$

The single term in Eq. 3.26 expresses what is commonly regarded in the literature as the complete EWOD force. The constant of denominator ($8d$) in the expressions given by J. Zeng $et\ al$. was different from the ($2d$) from T.B. Jones just

because of the different definitions for *V* (see Figs. 3.10 and 3.11). As a result, the electrostatic driving force (horizontal) obtained by T.B. Jones and J. Zeng *et al.* is identical to the result obtained in the current work within the classic electrostatic framework. All these three methods are equivalent. However, unlike the current work, none of those above-mentioned researchers gave further analysis of the vertical component of the electrostatic force.

3.4 Liquid Column Electrohydrodymanics

The physics of this dispensing principle is based on liquid column hydrodynamics described by the Navier-Stokes equation, which is derived from conservation principles of mass, momentum and energy. Here, the fluid is assumed to be incompressible and Newtonian without any external force such as gravity acting on the fluid.

When an ionized liquid comes into the microchannel driven by the capillary force, it stops at the interface of the 1st electrode coated with hydrophobic dielectric layer. A meniscus is formed and the ions are considered to be uniformly distributed throughout the liquid column without an external electric field, which is shown in Figure 3.12.
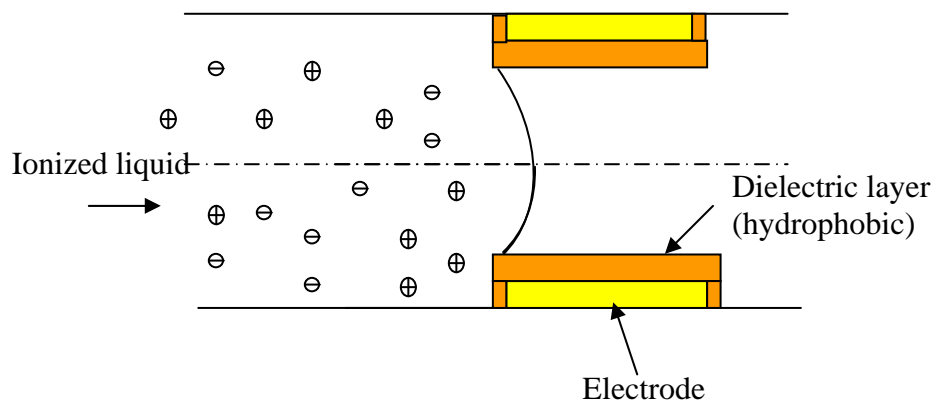
Fig. 3.12. The free charges uniformly distribute in the liquid which stops at the interface of hydrophobic dielectric layer.

Upon applying a voltage, the free charges conduct through the liquid and accumulate at the interface with the ambient fluid (air) as shown in Figure 3.7. From the Ohmic conduction model, there is no bulk free charge in the electrified liquid.

Figure 3.7 shows the internal fluid pressure P_m acting on the meniscus, the pressure from the surround medium P_a (atmosphere pressure) towards the fluid model, surface tension γ_{lv} and electrostatic force F_{el} acting on the interface between the fluid and air.

The presence of the interfacial charge results in an additional interfacial stress, especially a tangential stress, because of the repulsive force between these charges which in turn will modify the fluid dynamics. Thus, surface tension is affected by this interfacial stress to modify the contact angle and shape, depending on the density of surface charge.

Electrostatic force due to the accumulation of the charges significantly influences the fluid dynamics and consequently the meniscus and contact angle are affected.

It can be concluded that both of the surface tension and electrostatic force are affected by the surface charge density of these accumulated charges.

A mechanical equilibrium can be obtained at the interface of liquid and surrounding medium (air) so that a force balance can be derived from two symmetrical contact angles (top and bottom) [270]:

$$P_m - P_a = \Delta P = -\gamma_{lv} \cos\theta \left(\frac{1}{R_1} + \frac{1}{R_2} \right) \qquad (3.27)$$

where R_1 and R_2 are the principle radii of the meniscus. Eq. 3.27 is the Laplace equation stating that ΔP is a constant pressure difference across the liquid-air interface and independent of the position on the interface.

Assuming the substrate is homogeneous, it means that the liquid meniscus shapes a spherical cap in mechanical equilibrium. Thus, Eq. 3.27 can be simplified to ($R_1 = R_2 = R = H/(2cos\theta)$)

$$\Delta P = -\frac{2\gamma_{lv}\cos\theta}{R} = -\frac{4\gamma_{lv}\cos^2\theta}{H} \qquad (3.28)$$

where, H is the channel height. Equation 3.28 shows the mechanical equilibrium built across the liquid-air interface, which is caused by the change of contact angle upon applying voltage.

The characteristic contact angle change of the liquid upon applying voltage can be described by Lippmann-Young equation. However, it can not be applied to all system to obey the quadratic reduction of surface tension under applied electric field. B. Jonocha et al. demonstrated that both of decane droplets surrounded by water and placed on a polytetrafluoroethylene (PTFE) and a perfluoroalkoxy (PFA) thin film respectively presented an antisymmetric parabolic response with respect to applied voltage [206]. The plotted experiment data exhibited a linearity over than a parabolic curve. It indicated the Lippmann-Young equation was too simplified with negligibility of many factors which may affect the functional dependence of contact angle change in certain aspect. Here, we only consider the combined contributions from the materials properties of substrate and liquid itself, which determines the exact functional dependence on applied voltage. Thus, the functional dependence can be considered as a constitutive equation specific to the contributions from material properties of substrate and fluid involved:

$$\cos\theta = f[V, d, \varepsilon, \gamma_{sl}, R_a, ...] \qquad (3.29)$$

here, Ra is the surface roughness of substrate and f is less than 1.

A mathematical equation model for capillary driven flow of Newtonian fluid which comes into the microchannel and stops at the 1st hydrophobic dielectric layer is considered to analyze the fluid velocity profile. From the force balance across the liquid-air interface in Eq. 3.28, we can analyze the liquid column velocity profile and predict the meniscus velocity by solving Navier-Stokes equation with the proper boundary conditions. This simplified model is presented in order to provide a theoretical approach to fluid flow driven by electrowetting and demonstrate the fundamental hydrodynamic forces involved.

Figure 3.12 presents the sketch of the cross section of microchannel with the employed coordinate system. The parallel plates with channel height *H* and width *W* are brought into contact with liquid and placed horizontally. Taking the fluid as Newtonian, incompressible, fully developed, laminar and homogeneous, we use Cartesian coordinates x, y and z with origin on the bottom plane at the entrance of the microchannel. The balance between surface tension, hydrostatic pressure and viscous friction (gravity is negligible) generates a net force to drive the liquid move along the channel. The liquid motion is governed by time-dependent Navier-Stokes equation, which shows the dynamic momentum balance in the liquid [271]:

$$\frac{\partial \vec{v}}{\partial t} + (\vec{v} \cdot \nabla)\vec{v} = -\frac{1}{\rho}\nabla P + \frac{\mu}{\rho}\nabla^2 \vec{v} \qquad (3.30)$$

and the continuity equation

$$\nabla \cdot \vec{v} = 0 \qquad (3.31)$$

here in, $\vec{v}(x, t)$ and $P(x, t)$ are the velocity and pressure fields, respectively. ∇P is the pressure gradient between the liquid meniscus front and the entrance, which is the vector quantity defined as

$$\nabla P = \left(\frac{\partial P}{\partial x}, \frac{\partial P}{\partial y}\right) \qquad (3.32)$$

To further simplify the model, we also reasonably assume that the flow is only in one dimension (i.e., towards the activated electrodes along x axis) because the electrodes in this device is configured and fabricated on top and bottom of microchannel, which are along the path of liquid movement. Since the effect of the gravitational force is negligible and there is no other y-directional forces acting on the fluid, thus, the pressure gradient is assumed to be zero along the y-axis, i.e. $\partial P/\partial y = 0$. Therefore, the pressure gradient generated by electrowetting along x axis is given by:

$$\nabla P = \frac{\partial P}{\partial x} = \frac{\Delta P}{L(t)} = -\frac{4\gamma_{lv}\cos^2\theta}{H \times \left[L_0 + R(t)(1 - \sin\theta)\right]} \qquad (3.33)$$

where , $L(t)$ corresponds to the liquid column length measured from the entrance of the channel to the liquid meniscus front while L_0 is the constant distance between the fluid entrance and the left edge of the base of spherical cap shaped by liquid meniscus. As the surrounding medium is air, γ_{lv} is simply γ_l, the surface tension of liquid which can be commonly tabulated in handbooks.

For a micro-scale fluid flow, the laminar flow assumption can be employed. Combining this assumption for a fully developed flow, we can simplify Eq. 3.30 by assuming that the velocity component of the fluid flow is uniaxial, i.e. $v_x = v_x(y, t)$. As a result of these assumptions, the convective acceleration term in Eq. 3.30 vanishes, i.e. $(v \cdot \nabla)v = 0$.

In addition, since the y-component of the fluid velocity is zero, i.e. $v_y = 0$, and v_x does not depend on x-component for a fully developed flow, the $\nabla^2 \vec{v}$ term becomes:

$$\nabla^2 \vec{v} = \hat{x}\left(\frac{\partial^2 v_x}{\partial x^2} + \frac{\partial^2 v_x}{\partial y^2}\right) + \hat{y}\left(\frac{\partial^2 v_y}{\partial x^2} + \frac{\partial^2 v_y}{\partial y^2}\right)$$
$$= \hat{x}\left(\frac{\partial^2 v_x}{\partial x^2} + \frac{\partial^2 v_x}{\partial y^2}\right) = \hat{x}\frac{\partial^2 v_x}{\partial y^2}$$

(3.34)

Consequently, we can compute the internal velocity profile and estimate the liquid column velocity by solving Equation 3.29-3.34 subject to the appropriate boundary conditions. Because the transient length $L(t)$ is a global or marcoscopic quantity, averaging the Navier-Stokes equation across the liquid column is sufficient to account for the liquid meniscus contact line velocity. Thus, substituting Eq. 3.33 and Eq. 3.34 into the Navier-Stokes equation (Eq. 3.30) and integrating it over the directions orthogonal to the liquid flow direction, we have

$$\int_0^H \frac{dv_{avg}}{dt}Wdy = \int_0^H \left(-\frac{\nabla P}{\rho} + \frac{\mu}{\rho}\frac{\partial^2 v_x}{\partial y^2}\right)Wdy \quad \Rightarrow$$
$$W\frac{dv_{avg}}{dt}\int_0^H dy = -\frac{W\nabla P}{\rho}\int_0^H dy + \frac{\mu W}{\rho}\int_0^H \frac{\partial^2 v_x}{\partial y^2}dy \quad \Rightarrow$$
$$H\frac{dv_{avg}}{dt} = -\frac{H\nabla P}{\rho} + \frac{\mu}{\rho}\left(\frac{\partial v_x}{\partial y}\right)_0^H$$

(3.35)

where W is the channel width in the z direction. Based on the study of Huang, etc. [272], the velocity profile is parabolic Poiseuillean at a distance far enough away from the meniscus. Together with the assumption of small Reynolds' numbers on the order of less than 10, a typical parabolic profile of laminar flow for v_x between parallel plates is further approximated by:

$$v_x = \frac{3}{2}v_{avg}\left[1-\left(\frac{y}{H}\right)^2\right]$$

(3.36)

Furthermore, as the fluid moving distance L has length orders of magnitude greater than the channel height H, i.e. $L>>H$, we postulate that the fluids far away from the

meniscus moves like stacked rigid laminae whose velocity depends on the y-position based on Eq. 3.36. Therefore, we can directly assume v_{avg} as

$$v_{avg} = \frac{\partial L}{\partial t} = \frac{\partial (L_0 + R(t))}{\partial t} = \frac{\partial R(t)}{\partial t} \qquad (3.37)$$

i.e., the average flow velocity equals to the variation rate (expansion and contraction) of the meniscus radius. We can arrive at the differential equation by substituting Equation 3.36 and 3.37 in to Equation 3.35:

$$H\frac{dv_{avg}}{dt} = -\frac{H\nabla P}{\rho} - \frac{3v_{avg}}{2H^2}\frac{\mu}{\rho}(2y)_0^H \quad \Rightarrow$$

$$H\frac{dv_{avg}}{dt} = -\frac{H\nabla P}{\rho} - \frac{3v_{avg}}{H}\frac{\mu}{\rho} \quad \Rightarrow$$

$$\frac{dv_{avg}}{dt} = -\frac{1}{\rho}\left[\nabla P + \frac{3v_{avg}}{H^2}\right] \quad \Rightarrow$$

$$\frac{dv_{avg}}{dt} = \frac{4\gamma_{lv}\cos^2\theta}{\rho H[L_0 + R(t)(1-\sin\theta)]} - \frac{3\mu v_{avg}}{\rho H^2} \quad \Rightarrow \qquad (3.38)$$

$$\frac{d}{dt}\left(\frac{dR(t)}{dt}\right) = \frac{4\gamma_{lv}\cos^2\theta}{\rho H[L_0 + R(t)(1-\sin\theta)]} - \frac{3\mu}{\rho H^2}\frac{dR(t)}{dt} \quad \Rightarrow$$

$$\frac{d^2R(t)}{dt} + \frac{3\mu}{\rho H^2}\frac{dR(t)}{dt} - \frac{4\gamma_{lv}\cos^2\theta}{\rho H[L_0 + R(t)(1-\sin\theta)]} = 0$$

Since $L_0 \gg R(t)(1-\sin\theta)$, Eq. 3.38 can be approximately simplified as

$$\frac{d^2R(t)}{dt} + \frac{3\mu}{\rho H^2}\frac{dR(t)}{dt} - \frac{4\gamma_{lv}\cos^2\theta}{\rho H L_0} = 0 \qquad (3.39)$$

It can numerically solve Equation 3.39. As ρ, μ, H, γ_{lv}, L_0 and $\cos\theta$ are all constant,

let $c_1 = \frac{3\mu}{\rho H^2}$ $c_2 = -\frac{4\gamma_{lv}\cos^2\theta}{\rho H L_0}$, Equation 3.27 is converted to:

$$\frac{d^2R(t)}{dt} + c_1\frac{dR(t)}{dt} + c_2 = 0 \qquad (3.40)$$

The initial conditions are

$$\begin{cases} R(0) = \dfrac{H}{2\cos\theta} \\ R'(0) = 0 \end{cases}$$

Let $\dfrac{dR(t)}{dt} = \psi$, $\dfrac{d^2 R(t)}{dt^2} = \dfrac{d\psi}{dt}$, thus Equation 3.40 can be replaced by

$$\frac{d\psi}{dt} + c_1\psi + c_2 = 0 \quad \Rightarrow$$

$$\frac{d\psi}{dt} = -(c_1\psi + c_2) \tag{3.41}$$

Then, integrating Equation 3.41, we can obtain the result as

$$\int \frac{d\psi}{c_1\psi + c_2} = -\int dt \quad \Rightarrow$$

$$\frac{1}{c_1}\ln(c_1\psi + c_2) = -t + \eta \quad \Rightarrow$$

$$c_1\psi + c_2 = \exp[c_1(-t + \eta)] \quad \Rightarrow$$

$$\psi = -\frac{c_2}{c_1} + \frac{\exp[c_1(-t + \eta)]}{c_1} = \frac{dR(t)}{dt} \tag{3.42}$$

integrating Eq. 3.42, we have

$$\int dR(t) = \int \left\{ -\frac{c_2}{c_1} + \frac{\exp[c_1(-t + \eta)]}{c_1} \right\} dt \quad \Rightarrow$$

$$R(t) = -\frac{c_2}{c_1}t - \frac{\exp[c_1(-t + \eta)]}{(c_1)^2} + \lambda \tag{3.43}$$

Apply the initial conditions, $R(0) = \dfrac{H}{2\cos\theta}$ and $R'(0)=0$, we obtain that

$$\begin{cases} -\dfrac{c_2}{c_1}\cdot(0) - \dfrac{\exp[c_1(0 + \eta)]}{(c_1)^2} + \lambda = \dfrac{H}{2\cos\theta} \\ -\dfrac{c_2}{c_1} + \dfrac{\exp[c_1(0 + \eta)]}{c_1} = 0 \end{cases} \Rightarrow$$

$$\begin{cases} \eta = \dfrac{\ln c_2}{c_1} \\[2mm] \lambda = \dfrac{H}{2\cos\theta} + \dfrac{c_2}{(c_1)^2} \end{cases}$$
(3.44)

Substituting Equation 3.44 into Equation 3.43, we obtain $R(t)$, the transient radius of

liquid meniscus,

$$\begin{aligned} R(t) &= -\frac{c_2}{c_1}t - \frac{\exp[c_1(-t+\eta)]}{(c_1)^2} + \lambda \\[2mm] &= -\frac{c_2}{c_1}t - \frac{c_2\exp(-c_1 t)}{(c_1)^2} + \frac{H}{2\cos\theta} + \frac{c_2}{(c_1)^2} \end{aligned}$$
(3.45)

From Equation 3.45, the average velocity v_{avg} can be derived by substituting constants

c_1 and c_2 and Eq. 3.29,

$$v_{avg} = \frac{dR(t)}{dt} = \frac{c_2}{c_1}\left[\exp(-c_1 t) - 1\right] = -\frac{4H\gamma_{lv}f^2}{3\mu L_0}\left[\exp\left(-\frac{3\mu}{\rho H^2}t\right) - 1\right]$$
(3.46)

Hence, the velocity profile of v_x can be further approximated by

$$v_x = -\frac{2H\gamma_{lv}f^2}{\mu L_0}\left[\exp\left(-\frac{3\mu}{\rho H^2}t\right) - 1\right]\cdot\left[1 - \frac{y^2}{H^2}\right]$$
(3.47)

Figure 3.13 shows the simulated x-directional velocity profile of the liquid

column predicted by our hydrodynamic model given by Equation 3.47. The initial

velocity increases sharply because the internal pressure gradient builds up upon

applying voltage. Then, this pressure increase is counteracted by fluid viscous force,

which gradually becomes significant at longer time scales. Thus, liquid velocity

becomes convergent with time.
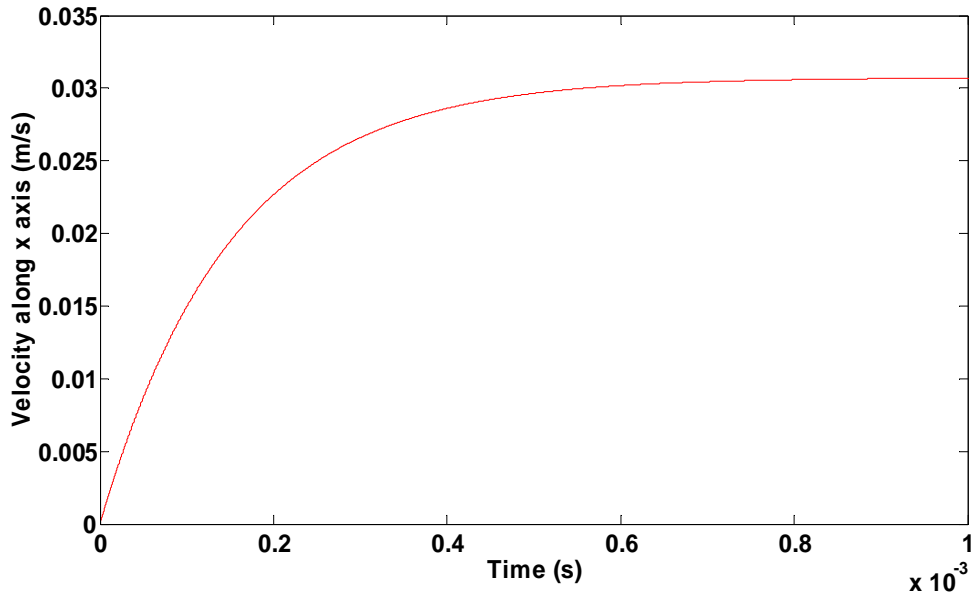
Fig. 3.13. Plot of the simulated x-directional velocity of the liquid column as a function of time.

However, the plotted velocity profile only includes the fact that the liquid column passes through the potentially activated electrode pad and it could reach the maximum predicted velocity before it go through the right edge of the pad. In the proposed design, the liquid column will have cleared the length of activated electrode (10 μm) and the gap of neighboring hydrophobic pads (10 μm) and stopped at the adjacent hydrophobic pad. Once the liquid meniscus passes through the potentially activated pad, the electrowetting-induced pressure gradient suddenly vanishes. This causes the liquid column to decelerate immediately in the presence of viscous force until it stops at the adjacent hydrophobic pad which is not potentially activated. A new mechanical equilibrium is built up to balance the internal pressure of liquid column and surface tension.

Figure 3.14 and Figure 3.15 show the simulated radius of liquid meniscus and the time-averaged flow rate of the liquid column as a function of time predicted by Equation 3.45 and 3.46 respectively. Assuming the initial contact angle is

approximately 105°, the radius of liquid meniscus increases from 40 μm to 40.6 μm in less than 0.1 ms. It means the radius rises only about 1.5%. The simulated time-averaged flow rate shown in Fig. 3.15 increases sharply and converges with longer time scales, the tendency of which is consistent with the simulated x-directional velocity of the liquid column.
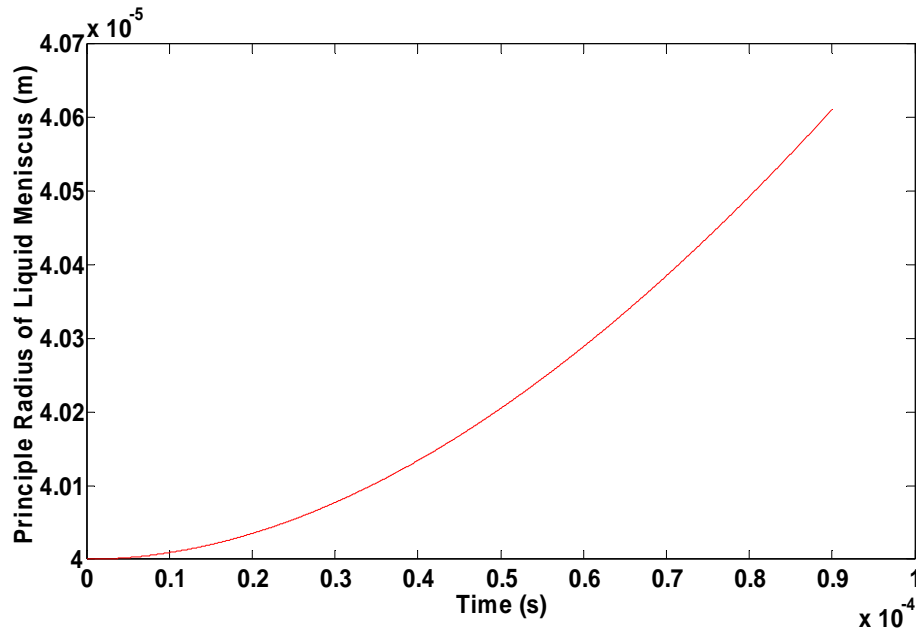
Fig. 3.14. Plot of the simulated principle radius of liquid meniscus as a function of time.
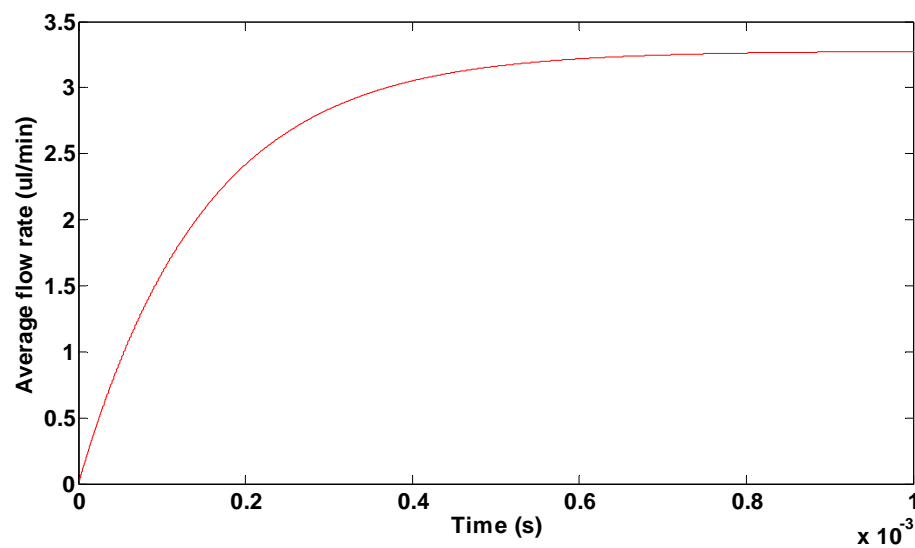
Fig. 3.15. Plot of the simulated time-averaged flow rate of the liquid column as a function of time.

Figure 3.16 shows the time-averaged flow rate of the liquid column as a function of applied voltage predicted by Equation 3.47. The simulated flow rates are symmetric with respect to both positive and negative voltages. The flow rate simply rises as a function of voltage and reaches approximately 0.24 μl/min at ± 50 V. However, the flow rate initially begins at a relatively low value and increases monotonically and slowly till about 20 V, reaching almost 24 nl/min.
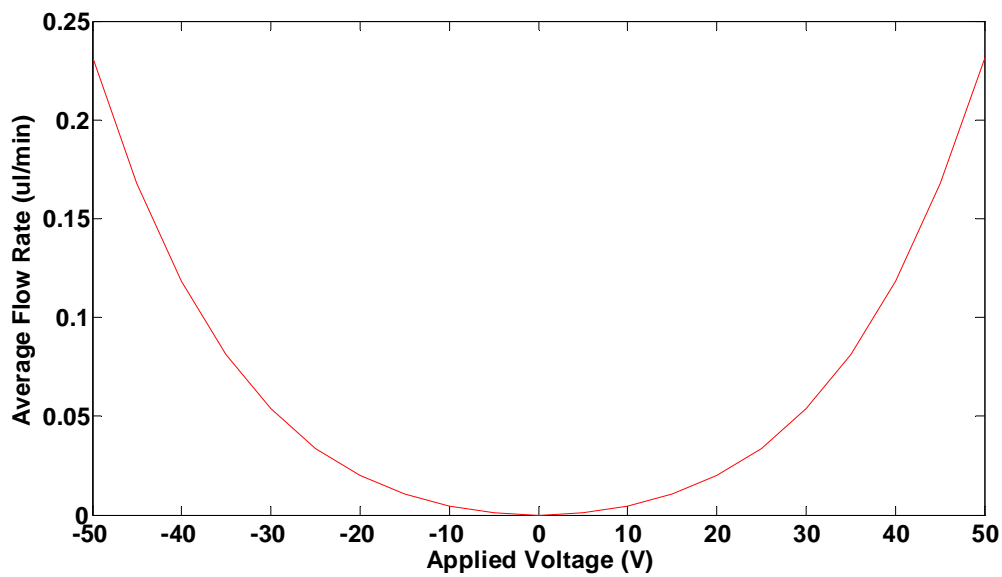
Fig. 3.16. Plot of the simulated time-averaged flow rate of the liquid column as a function of applied voltage.

The time-averaged x-directional velocity of liquid column as a function of the dependence factor f is plotted in Figure 3.17. Among all the parameters in f, only voltage is adjustable while the others (dielectric constant, dielectric thickness, surface tension of liquid- vapor, surface roughness, etc.) remain constant. Thus, the time-averaged x-directional velocity can be considered as a function of applied voltage in the plot of Figure 3.17. The tendency of the time-averaged x-directional velocity as a function of applied voltage is almost identical to that of the flow rate, shown in Figure 3.16 and 3.17. Since the electrostatic force is a function of applied voltage (Eq. 3.13),

which is only manipulatable among the parameters of the dependence factor f, the plot in Figure 3.17 demonstrates the average flow rate as a function of the electrostatic force. Hence, the effect of the electrostatic force on the velocity and flow rate of the liquid column is depicted based on the investigations of their functions of the dependence facto f, i.e., the cosine function of contact angle.
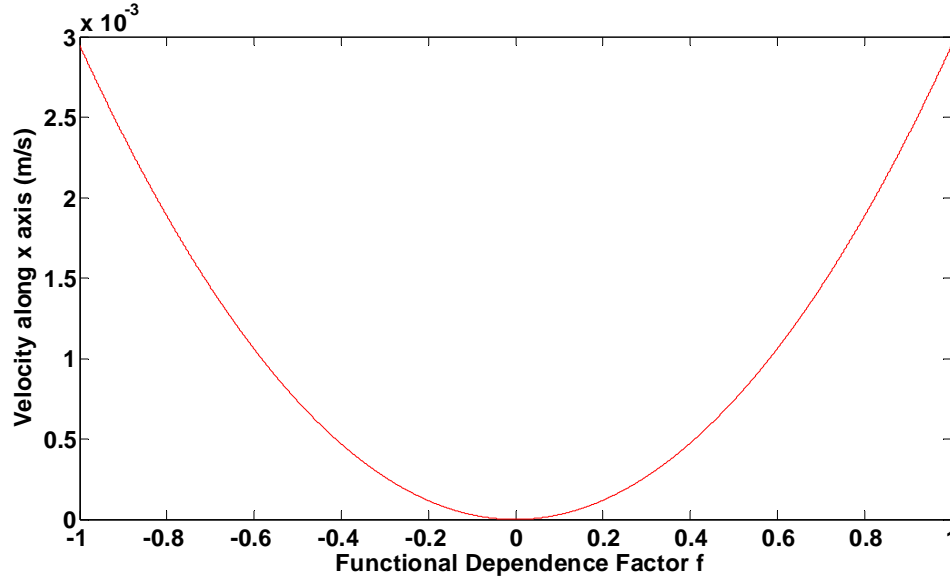
Fig. 3.17. Plot of the time-averaged x-directional velocity of liquid column as a function of the dependence factor f.

The simulation results of the time-averaged flow rate as a function of applied voltage based on our model will be compared with experimental measurements in Chapter 5.

3.5 Proof-of-concept EWOD Device

A proof-of-concept device was fabricated with relative large feature sizes, see Figure 3.18. Chrome and gold electrodes were deposited and patterned on silicon chip. The electrodes were then electrically connected to a power supply. Cytop™ fluoropolymer, acting as the hydrophobic dielectric layer was manually coated with brush

(approximately 5um thick) to cover the electrodes. A double-sided tape was used in order to bond the glass chip and the silicon chip together, and to form a capillary channel (200 μm width and 50 μm height). At the bottom of channel, the Cytop™ coated electrodes were exposed to air. Figure 3.18 shows a series of snapshots taken when the device was delivering water.

Firstly, water column rapidly propagated with low contact angle from the left (entrance) into the channel due to capillary effect (Figure 3.18a). It stopped at the hydrophobic dielectric area (marked red) and the contact angle became higher (Figure 3.18b). Once applying voltage of 30 V, the meniscus slightly changed (Figure 3.18c) and the liquid column started propagating again to pass through the channel with low contact angle again (Figure 3.18d).

(a)

(b)

(c)

(d)
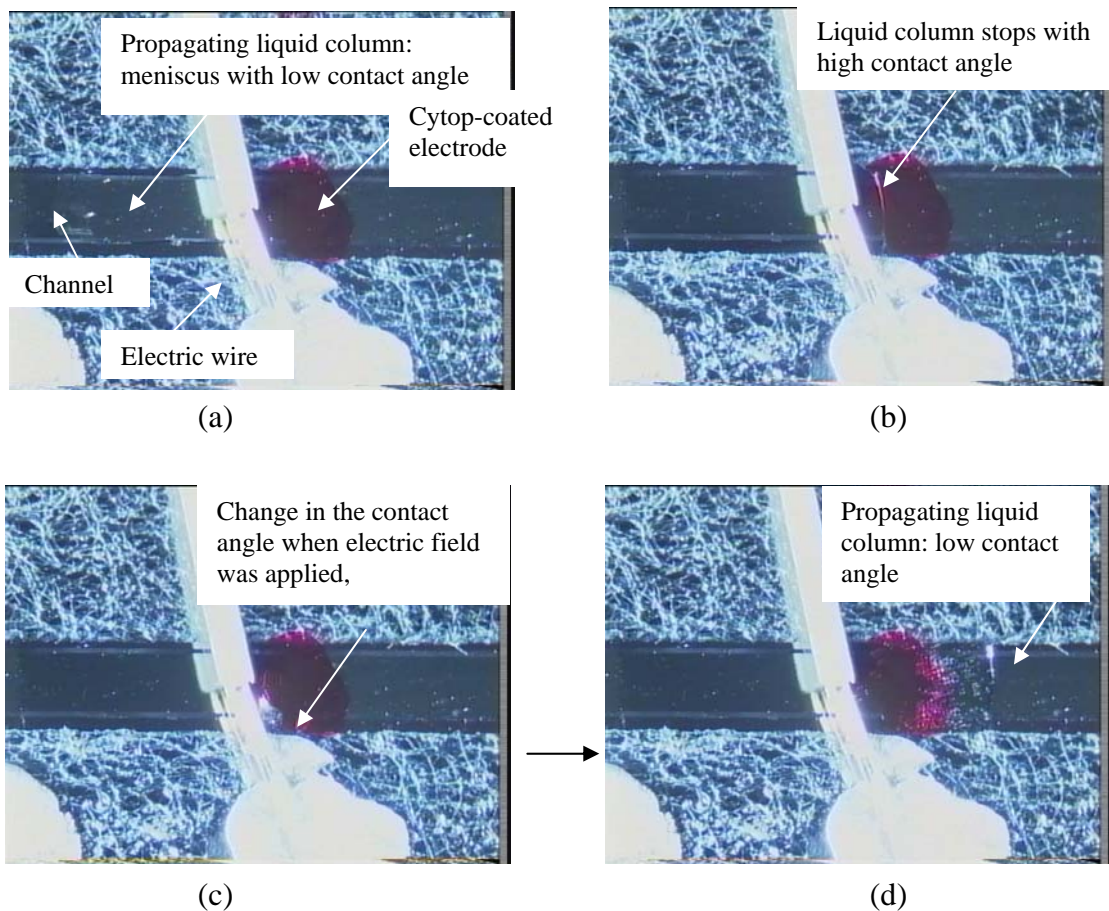
Fig. 3.18. The snapshots of dispensing sequences of proof-of-concept device.

In this prototype, the response time of the water column to achieve a change of contact angle in initializing a propagation was in the order of several seconds due to a relative thick dielectric layer. A relatively low voltage (above 30 V) was required to initiate the actuation. A further miniaturized device is capable to dispense nano liter volume at a low voltage and low power consumption.

CHAPTER 4

DEVICE REALIZATION

Based on the preliminary tests on the dependence of contact angle on various dielectric materials and the proof-of-concept prototype discussed in the previous two chapters, a miniaturized device based on EWOD principle was fabricated using microfabrication technologies involving silicon, glass and polymer materials. The detailed fabrication process of each essential part of the device and the assembly process are described in the following sections of this chapter.

4.1 Bottom Plate Fabrication

4-inch bare silicon (100) wafers were cleaned by following the standard cleaning process. The process flow is shown in Appendix B1. A thin layer of silicon dioxide was thermally grown on these silicon wafers and its thickness was controlled at around 500nm.

Then, the silicon wafers were immediately spin-coated with the photoresist of Shipley SPR220-3.5, which was a multi-wavelength compatible photoresist to cover a wide range of film thickness (1-10 μm) with good uniformity. The thickness was measured to be 3.5 μm at 2500 rpm. Then, the wafers were soft-baked at 115°C for 90 s on a contact hotplate. Before photolithography process, the wafers were immersed

into Shipley's Microposit® MF CD-26 developer for 10 s to harden the photoresist surface. It greatly improved the lift-off process to achieve almost vertical side wall with under cut. Then, the wafers were cleaned with running DI water and blown dry with nitrogen.

The UV-exposure was carried out using a Karl Suss MA6 mask aligner. The exposure time was set at 22.5 s with a constant intensity of 11.5 mW/cm^2 (365nm). After that, post-exposure bake was carried out at 115°C for 90 s on a contact hotplate followed by developing for 60 s in the developer of MF CD-26. At this moment, the window for electrode deposition was open while the other area was still covered by photoresist as shown in Appendix B1(a). Subsequently, the chrome (Cr) / gold (Au) (100 Å / 2500 Å) was sputter-deposited and patterned by lift –off process as shown in Appendix B 1(b) and (c) respectively. So far, the electrode pads were formed on the silicon wafers together with alignment marks.

Cytop (CTL-809A) was spin-coated on the silicon wafers at 3000 rpm for 40 s with a ramp rate of 500 rpm. CTL-809A has a good adhesion to silicon without using any adhesion promoter. Then, it was cured preferably at a temperature of 180°C for 10 min on a contact hotplate followed by spin-coating of a layer of thick photoresist of AZ4620. Its thickness was measured at about 700 nm at 5000 rpm. Then the wafers were soft-baked at 90°C for 1 min on a hotplate followed by exposure for 4.5 s at 11.5 mW/cm^2. After that, the photoresist was post-based at 100°C for 1 min and developed in AZ developer for 50 s. Hard baking was implemented at 120°C for 1 min. Thus, the window was open for removal of the residual Cytop as shown in Appendix B 1(d). Subsequently, oxygen plasma was used to etch the residual Cytop while Cytop dielectric layer was protected by AZ4620 photoresist as a masking layer. The residual

Cytop was completely etched away in 90 s with a power of 150 mW and an oxygen flow of 20 sccm. Then, the photoresist was stripped and wafers were cleaned with DI water and blown dry as shown in Appendix B1(e). Figure 4.1 shows the SEM picture of Cytop-coated electrodes.
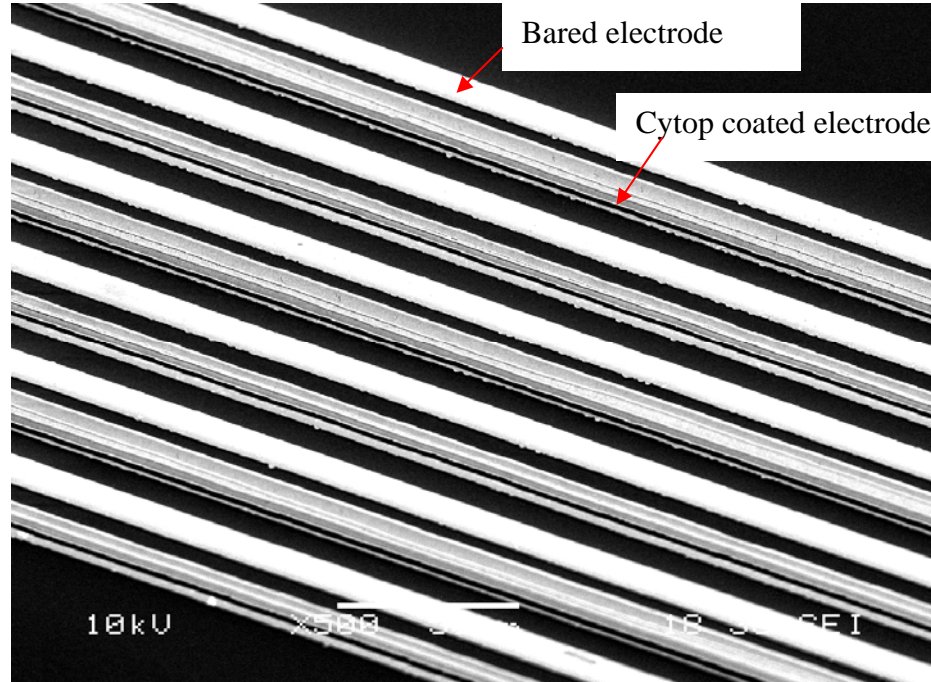
Fig. 4.1 SEM photo of Cytop-coated electrodes.

Nano™ SU-8 2050 negative photoresist (Micro Chem) diluted with cyclopentanone (C_5H_8O, Sigma Aldrich) was spin-coated on to the wafers at 3000rpm and soft baked by two steps (65°C for 3 min followed by 95°C for 6 min) to achieve a measured thickness of 20.2 μm. Then it was exposed (365nm) for 50 s and post-baked also at two steps (65°C for 1 min followed by 95°C for 1 min) to minimized the stress resulted from readily cross-link. Rapid cooling after post baking should be avoided. After that, it was developed by SU-8 developer for about 4 min followed by rinsing with IPA. Finally, the microchannel (100 μm wide and 20.2 μm high) was formed by SU-8, on bottom of which the Cytop dielectrics and electrodes were exposed to air as shown in Appendix B1(f).

4.2 Top Plate Fabrication

4-inch Pyrex$^{®}$ glass wafers were cleaned using the standard process which is identical to the process for silicon, which is described in previous section. The process of metal electrodes using chrome and gold is the same as it of silicon. The process flow is shown in Appendix B2. Cr / Au (100 Å / 2500 Å) were deposited by sputtering and patterned by lift-off process followed by spin coating of Cytop™ as shown in Appendix B2(a)-(c). Indium-tin-oxide (ITO) was used later on order to facilitate viewing. Photoresist AZ4620 was spin-coated on top of Cytop™ and patterned as a masking layer as shown in Appendix B2(d). Oxygen plasmas etching was utilized to remove the residual Cytop™ with the same parameters for silicon wafers, shown in Appendix B2(e). Thus, a dielectric layer of Cytop™ was made on top of the electrodes.

4.3 Device Bonding

Two through holes of a diameter of 2 mm were manually drilled with the diamond drill on glass plate for fluid connection. Then, both the top and bottom plate were cleaned respectively for the bonding process. As shown in Figure 5.2, the bottom plate was placed on a heater with a center hole connected to a vacuum pump to supply vacuum pressure. The top plate with patterned structures facing downward was held by vacuum pressure, applied by a vacuum pump. The vertical and horizontal displacement of this metal tubing could be mechanically manipulated for alignment purpose through a x-y stage.
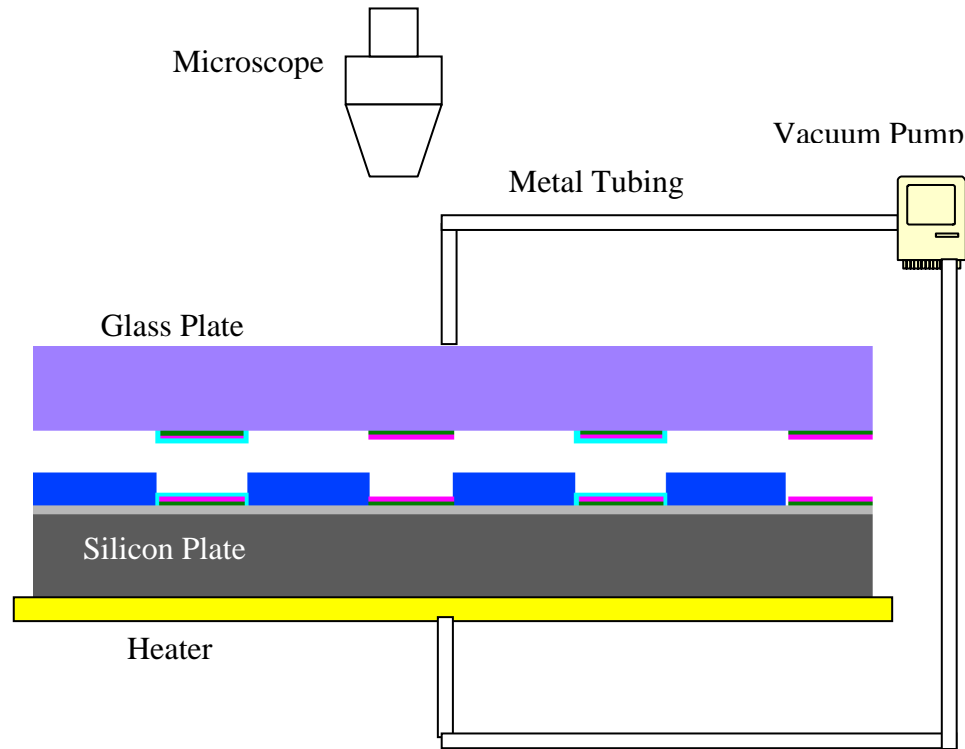
Fig. 4.2. Experimental set-up for device bonding.

A microscope was used to observe the alignment marks of the top and bottom plate, through the transparent top plate. The position of the top plate was adjusted by a xyz transportation stage while the bottom plate could be rotated by a rotation stage. The top plate was moved down and stayed at about 0.2-0.3 mm on top of the bottom plate. Then, the positions of both plates were adjusted to align properly. Subsequently, the top plate was moved down till it touched the bottom plate. After that, the top plate was continuously tuned a little bit further down to apply a pressure acting on the bottom plate. The heater was heated up to 150°C and after about 30 min the device was uniformly bonded.

Then, the bonded device was attached to a PCB chip by epoxy and the electrode pads of the device were electrically connected to the PCB by wire bonding. Finally,

electrical wires were manually soldered to connect with the PCB. The completed device is shown in Figure 4.3.
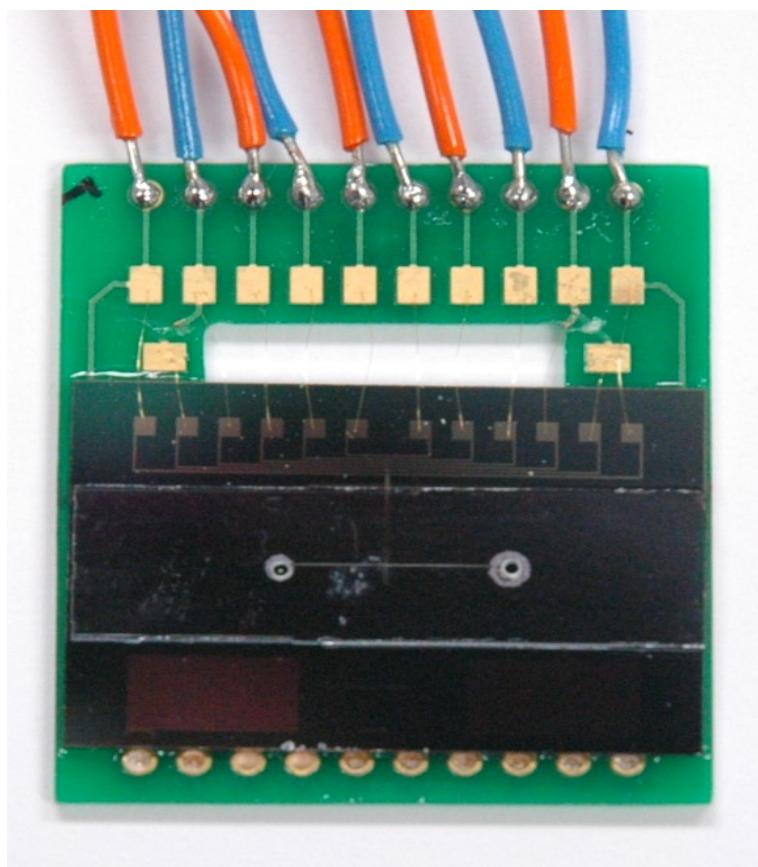
Fig. 4.3. The completed hydrophobicity-controlled microfluidic dispenser.

4.4 PDMS Bonding Technology

4.4.1 Introduction

In recent years, many more scientific and industrial attentions have been paid to the polymer-based microfluidic systems and devices which become increasingly important in environmental monitoring, diagnostic and biological applications [273-6]. The miniaturized polymer-based systems and devices provide a powerful and multifunctional platform for biological assays because of many advantages over the

traditional systems based on semiconductor materials [277-8]. The criteria which should be taken into account to design these devices and systems includes the material property and cost, fabrication expense and chemical and biological compatibility. Thus, to meet these requirements, the conventional semiconductor materials, like silicon and glass, are not as competitive as polymer substrate in fluid handling applications.

However, one of the key steps in developing the functional polymer-based systems and devices is bonding of the polymer substrates. For practical concern, it requires a reliable and reproducible bonding process which does not change the components properties and performance. In addition, the deformation and distortion of the micron and nanometer sized structures between the substrates must be tolerable after the bonding process. Unfortunately, the existing polymer-to-polymer substrates bonding methods including ultrasonic, thermal, gluing by epoxy, are not precise enough and induce much geometrical deformation of the structures. Therefore, temperature control and material properties are very critical to the success of bonding process.

Polydimethylsiloxane (PDMS), an elastomeric polymer, has become very popular as one of the structure materials in fabrication of MEMS/microfluidic devices because of its significant material properties [279-82]. It is transparent to offer optical alignment for the multi-layer device fabrication. It is also biocompatible and relatively inert. Furthermore, the fabrication processes, like micro-molding processes are simple and fast and the cost is low. So far, the techniques for bonding PDMS to polished silicon and glass wafers have been reported by many researchers [273, 275, 283-5]. However, there is no published paper or patent about the PDMS bonding with unpolished silicon. PDMS can be a potential material to replace the glass as the top

substrate for the microfluidic dispenser presented in this study. It needs to be bonded with unpolished Si or glass, which is cheaper than polished Si or glass for mass production.

4.4.2 Bonding Procedure

We are going to develop a bonding technology using oxygen plasma treatment for PDMS surface activation, which can be used to bond PDMS with glass, polished or unpolished silicon surface and PDMS itself. The bonding strength, anti-leakage performance and surface property should be acceptable for the biochip from an industrial company for the biomedical applications.

The bonding process started with the preparation of PDMS substrates. A curing agent and PDMS prepolymer were mixed at the ratio of 1:10 by weight. Then, the prepolymer mixture was degassed in a 30Hgmm vacuum oven for 1 hour to remove air bubbles to obtain a completely mixing of the two parts. The aluminum master was uniformly coated with a thin layer of polymer in order to reduce the adhesion between the master and the cured PDMS. Then the mixed PDMS was poured into the aluminum master and cured for 4 hours at 80°C on a hotplate. After curing, the thin PDMS replicas were peeled off from the master. The glass, polished and unpolished silicon and PDMS layers were diced in the same size of the PDMS replicas (25mm x 25mm).

Oxygen plasma treatment for PDMS surface activation was carried out using a parallel-plate reactor reactive ion etching (RIE) system (Oxford RIE system) with sample located on the water-cooled cathodes. The glass, polished and unpolished silicon and PDMS layers were also cleaned by oxygen plasma. A special fixture was fabricated to protect the cavity area of PDMS replicas from the plasma etching during the process. Within 5 min after RIE process, the plasma-treated samples were immediately aligned under a microscope and the activated surfaces were bonded

together applying certain pressure and heat uniformly in a vacuum oven. The bonded samples are shown in Figure 4.4.

(a)PDMS –to-unpolished Si
(55mm x 55mm)
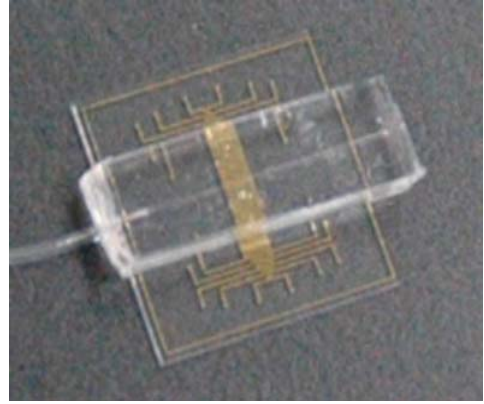
(b)PDMS–to-glass (Pyrex) with Au electrodes (a microchannel formed in PDMS)
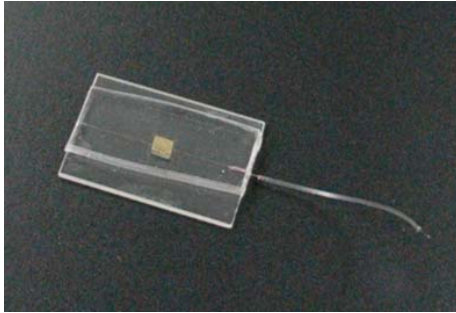
(c) PDMS–to-glass (lasfn9) with Au electrodes (a microchannel formed in PDMS)
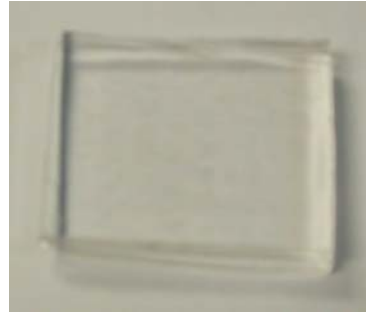
(d) PDMS-to-PDMS

Fig. 4.4. PDMS bonding with several different substrates.

4.4.3 Testing Results

Tensile Strength Test

The tensile strength test was performed by using Instron tensile strength machine. The test set up is shown in Figure 4.5.

Araldite glue was used to attach the top and bottom surfaces of the samples to the substrate holders. It was about 2.24 MPa between glass and PDMS as shown in Figure 4.6. For silicon-PDMS sample, as the surface property of PDMS was highly hydrophobic, either super glue or Araldite® epoxy was not able to attach PDMS to the

substrate holder firmly. Therefore, when the pulling force applied, the interface between the holder and the PDMS surface peeled off at the strength of 0.288MPa shown in Figure 4.7 before obtaining the bonding strength of polished/unpolished silicon-PDMS. The bond interface remained as usual, which is shown in Figure 4.8.
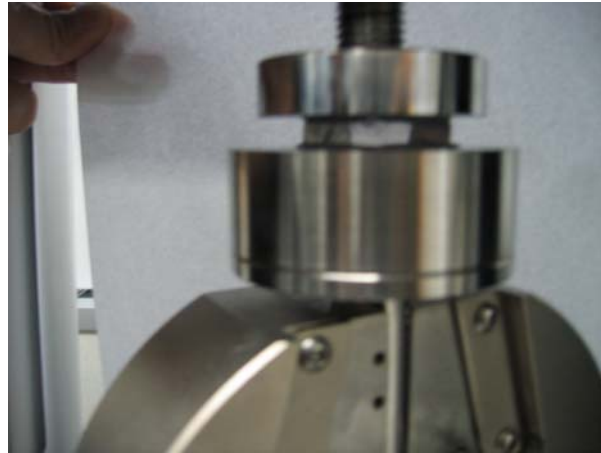
Fig. 4.5. The tensile strength test set up.
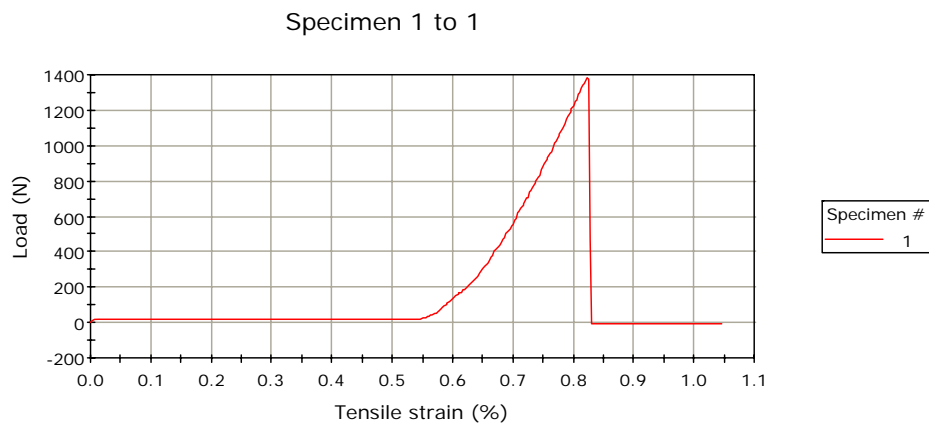
Fig. 4.6 The bonding strength of glass-PDMS.

Specimen 1 to 1
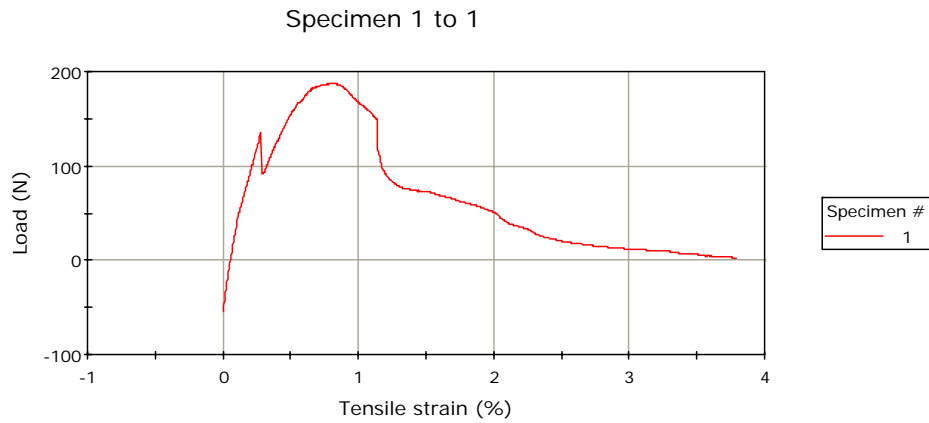
Fig. 4.7. The interface between the glue and the holder peeled off before obtaining the bonding strength of polished/unpolished silicon-PDMS.
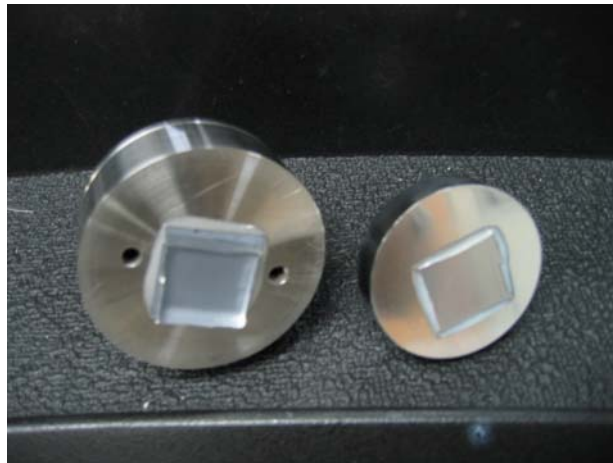
Fig. 4.8. The bond interface of silicon-PDMS remained.

Leakage Test

The most common concern about the performance of microfluidic system is the leakage problem. Many existing polymer-to-polymer substrate bonding methods such as gluing by epoxy will induce the unevenness and leakage along bond interface of the device. Thus, leakage testing was carried out for evaluate this bonding technique. The testing setup and schematics are shown in Figure 4.9(a) and (b) respectively.
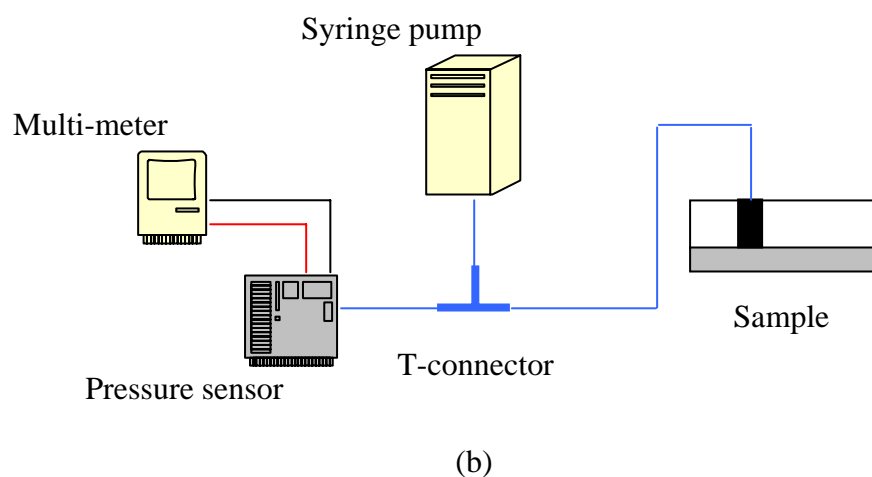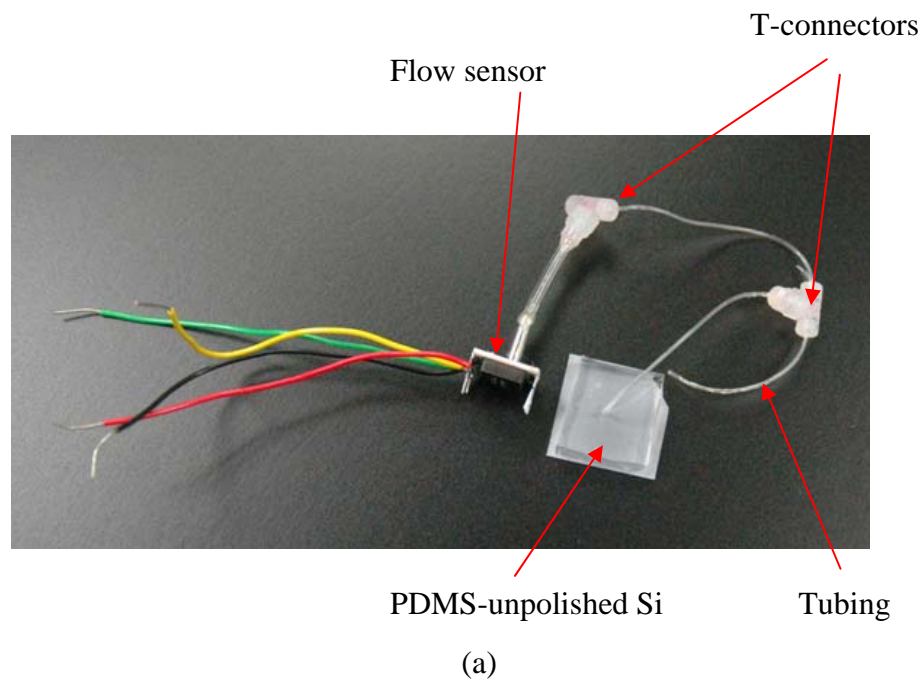
Fig. 4.9. The leakage testing setup, (a) the components; (b) the schematics.

A syringe pump was used to generate the flow pressure. It was connected through T connector to the pressure sensor (SM5612, Silicon Microstructures Inc., CA) and the flow channel to form a closed system. The flow channel was made through the PDMS layer till the silicon/glass surface. The pressure sensor was calibrated before the testing to convert the voltage readings to the pressure (Psi). It was

observed that there is no leakage between the interfaces when the pressure was measured to reach about 70 Psi.

4.4.4 Conclusions

A low temperature bonding technique for bonding PDMS with glass, polished or unpolished glass, and PDMS itself has been successfully developed to achieve reliable bonding strength, precise control of surface property of bonding interfacial layer. A biochip from an industrial company was successfully fabricated by this technique. The bonding technique, using cured PDMS which surface was activated by oxygen plasma, shows a low temperature (<120°C) and bonding strength of 2.24MPa in glass-to-PDMS interface and well above 0.288MPa in PDMS-to-unpolished Si interface. The substrates were bonded to achieve precise-control of surface property to be compatible with biofluids and without any global geometrical deformation. The substrates were tested with tensile strength and leakage test. Results of the tensile strength test showed that the bonding quality was satisfactory for the biomedical applications. No leakage was observed under the pressure of 70 Psi in a closed microfluidic system. We have demonstrated an effective and low temperature bonding technique to bond PDMS to glass, polished or unpolished silicon and PDMS itself.

A US patent application titled "Bonding of polymer to silicon, glass, another Polymer or other Materials" (inventors: Saman Dharmatilleke, Liu Hong) was file on 23 June 2006 with an ETPL (Exploit Technologies Pte Ltd) reference no. of IMR/P/04061/00/US.

CHAPTER 5

TESTING AND DISCUSSIONS

A hydrophobicity-controlled microfluidic dispenser with an inbuilt metering feature was microfabricated as described in the previous chapter. This chapter presents the following experimental study to characterize dynamics of the functional device. We firstly describe the experimental setup and techniques for determining the liquid velocity. This is followed by discussions on some significant issues on the difficulties and limitations encountered during the experiments, and how these issues influence the obtained experimental results. Finally, the experimental results are presented to illustrate the behaviour of liquid hydrodynamic.

5.1 Experimental Methods

5.1.1 Experimental Setup

The experimental setup used for testing the electrowetting based microfluidic dispenser is shown in Figure 5.1. Firstly, the device was mounted onto the glass stage of a zoom stereo microscope (Olympus SZ1145TRF) by polyimide tapes. Then the electrolyte (pure water) was typically dispensed onto the inlet of the chip to serve as a

liquid reservoir using a micropipette after positioning the chip. The positive terminal of a dual-channel DC power supply which is able to output a 60-V was connected to the electrical wire which was in contact with the Cytop-coated electrode while the negative terminal was connected to the bare electrode and fixed by the tape.

Fig. 5.1. The photograph of the experimental setup.

Experiment was videorecorded through an Olympus microscope and a 3 CCD color video camera (Sony 390P) into a VHS videocassette by a JVC video cassette recorder for further analysis. Later, the video was converted into a movie file compatible with Microsoft Media Player and the image or frame could be captured by Microsoft Windows Movie Maker in a 2.80 GHz Pentium 4 desktop computer. A TV was connected to the CCD camera to synchronically display the experimental video of the device. Figure 5.2 shows the diagram of the experimental setup.
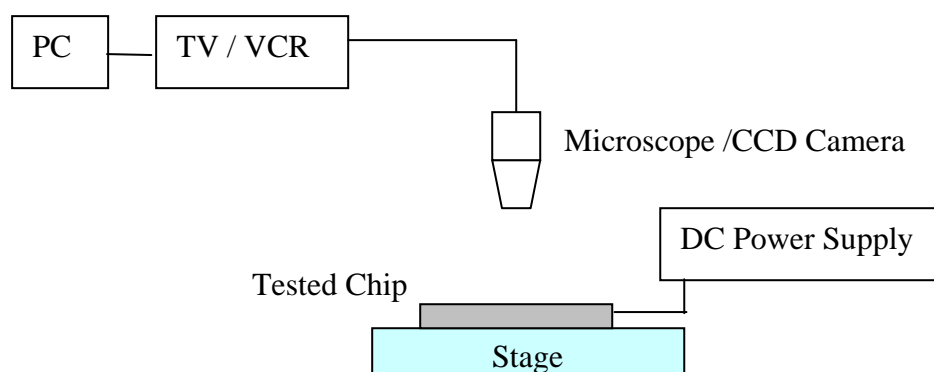
Fig. 5.2. Diagram of the experimental setup.

Before starting the experiment, it is predictable that the maximum liquid velocity depends on the following experimental or operational factors: the rise time of applied potential, the switching time to apply potential. The output voltage rise time was measured to be approximately less than 10 μs over the range of 0-60 V. In this investigation, we manually applied voltage between the bare and Cytop-coated electrodes. Improvement can be made in the future to automate this process by using electronic circuit and control algorithm of a multiplexer. Once the liquid column passed the first Cytop-coated electrode and stopped by the 2nd Cytop-coated electrode, the electrical wires have to be switched to connect the neighbouring electrical pads to provide the voltage potential to actuate the sequential fluid motion. This switching time was estimated to be about 0.1-0.2 s. To initiate a propagation of the fluid to pass through the first Cytop-coated electrode, the voltage was slowly increased from 0 V at a step size of 2.5 V till the propagation was observable. Subsequently, the actuation potential was applied in the following actuations. This approach was helpful to prevent the dielectric breakdown and minimize the power consumption. The manual switching time could be minimized to the range of micro seconds using a multiplexer controlled by an algorithm embedded in a computer.

5.1.2 Liquid Velocity Measurement

One of the fundamental specifications of interest to design and operate the microfluidic device is the maximum flow rate at which an amount of fluid volume is generated at a unit time. The characterization of this maximum flow rate was an essential objective in this study of the device.

Video Frame Analysis Approach

Liquid column movement along the microchannel was video recorded, which could be used to determine the liquid velocity with a moderate accuracy. The video frames were captured at a speed of 30 frames/s. Additionally, the distance between the initial and end position of the leading edge of the moving liquid column could be calculated through the scale with respect to the magnification of the microscope. Hence, the liquid column velocity could be obtained by counting the video frames between the initial and end position of the leading edge of the liquid column. Due to the limited accuracy in the positioning of the leading edge of liquid column, this approach was suitable for measurement of relatively low liquid velocities.

Fluid Volume Measurement Approach

The fluid velocity can be obtained indirectly by measuring the delivered fluid volume at a unit time, which is very commonly used for microfluidic device testing. The outlet of the device was connected through small tubing to a container placed in a weighing balance. By calculating the time interval between the first and last liquid droplet dropped into the container and the mass difference, an average volume flow rate with a unit of micro/nanoliters could be obtained in consideration of the evaporation rate of liquid. The liquid moving velocity could be obtained if we further divided the volume flow rate by the cross section area of the microchannel. This

method is applicable for relative high velocities with a relative high accuracy when liquid evaporate rate is negligible.

In-built Digital Metering Approach

This device has an innovative feature of in-built digital metering over the other reported micropumps and actuators to precisely determine the liquid column volume. The number of Cytop-coated electrodes spaced by a constant pitch, which the liquid column passes through, is always controllable by a multiplexer which applies the potential to the electrodes. Therefore this device does not require an additional flow sensor for metering the liquid flow.

5.2 Liquid Transport Testing

The device was fabricated according to the fabrication process flow illustrated in Chapter 4. Figure 5.3 shows the main functional area of the completed device inspected under the microscope.
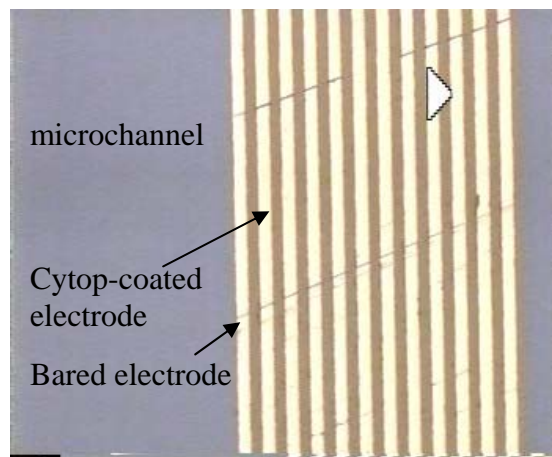
Fig. 5.3 The main functional area of the completed device
inspected under microscope.

The fluid path in this device consists of the following elements of different surface wetting characteristics, as schematically shown in Figure 5.4:
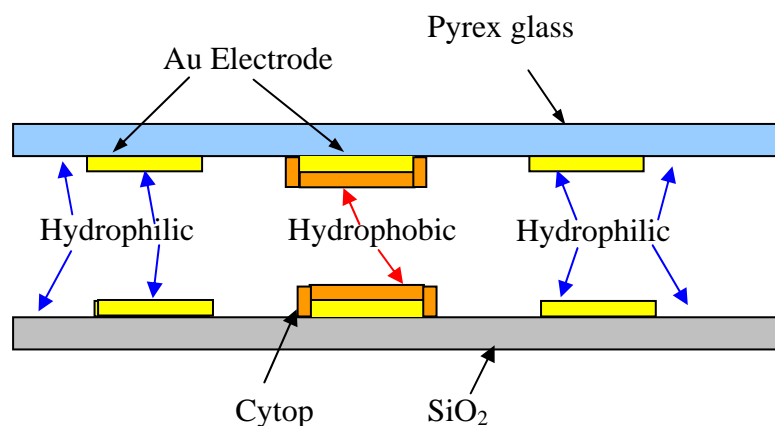
Fig. 5.4 The wetting characteristics along the fluid path
(the side wall is hydrophobic and not shown above).

- Top glass: hydrophilic

- Bottom silicon dioxide: hydrophilic

- Bare Au electrode (top and bottom): hydrophilic

- In-between electrode (top and bottom): hydrophilic

- Cytop-coated electrode (top and bottom): hydrophobic

- Side wall of microchannel (SU-8): hydrophobic (not shown in Figure 5.4)

Figure 5.5 shows the sequential images of the introduction, actuation and propagation of water column. Initially, water droplet was dispensed onto the entrance of the microchannel and subsequently propagated into the channel driven by capillary force. In the images, the propagating direction of water is from left to right. The electrodes in the order of odd numbers (the 1st electrode is in left hand side) were coated with Cytop™ while the even-numbered electrodes were bare. It was observed that the fluid propagated into the channel by capillary force (as shown in Figure 5.5(a)) till the liquid meniscus stopped with three-phase contact line at the 1st electrode and the leading edge of meniscus at the 2nd electrode as shown in Figure 5.5(b).
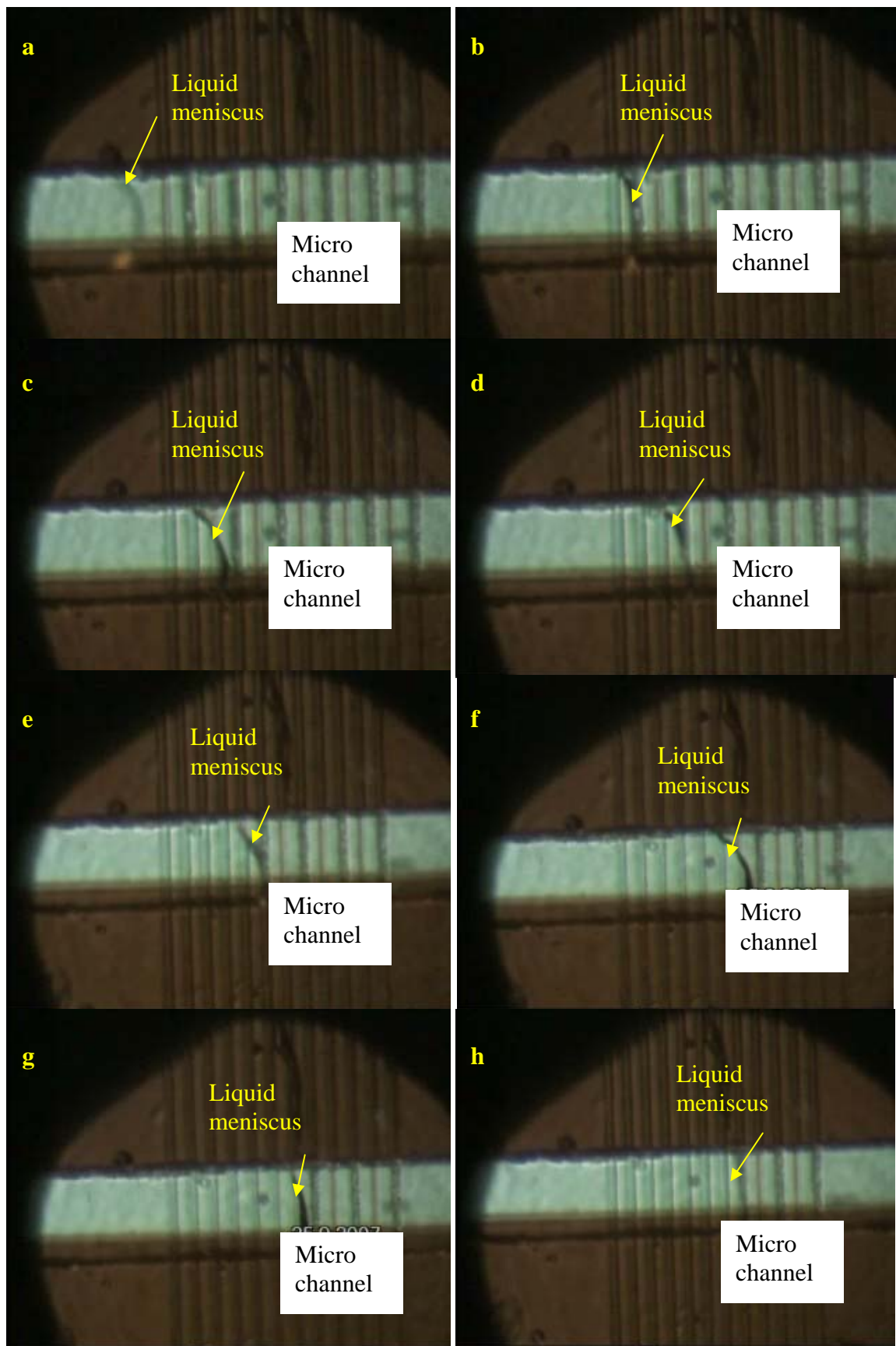
Fig. 5.5 The detailed motion of the EWOD actuated liquid column.

The displacement of the leading edge of meniscus along the fluid path was focused to analyze the fluid velocity as its behaviour was much more easily observable than that of three-phase contact line under this experimental condition. Then, we applied the potential voltage from 0 V with an interval of 2.5 V. When the potential voltage reached 20 V, EWOD effect was actuated and the liquid meniscus started propagating as shown in Figure 5.5(c) and stopped at the 4th electrode(as shown in Figure 5.5(d)). Upon applying the potential again, the liquid meniscus continued to propagate to clear the electrode gap as shown in Figure 5.5(e-g) till it stopped at the 8th electrode as shown in Figure 5.5(h). The experiments were implemented under the applied voltages from 20 V to 50 V at an interval of 5 V using the fabricated device. The liquid displacement images were video recorded at an interval of 30 frames per second in all experiments at room temperature.

Figure 5.6 shows the plot of both simulated (the solid line) and measured (the dashed line) time-averaged flow rate of liquid column as a function of applied voltage. The average flow rate is computed by calculating the time it takes for the liquid meniscus clear the length of the activated electrode pad and then averaging the fluid volume over that period. The agreement of our model with the experimental data is examined by the standard deviation, which is a measure of the spread of their values and given by:

$$\sigma_{sd} = \sqrt{\frac{1}{N}\sum_{i=1}^{N}\left(s_i - \bar{s}\right)^2} \qquad\qquad (5.1)$$

Here, σ_{sd} is the standard deviation, s_i is the shortest distance between any experimental point and the simulated model while $\bar{s}$ is the mean of summation of s_i. Hence, we obtain that the standard deviation σ is as small as about 0.009083 µl/min. It shows that

our model agrees well with our experimental results in both positive- and negative-voltage regime.
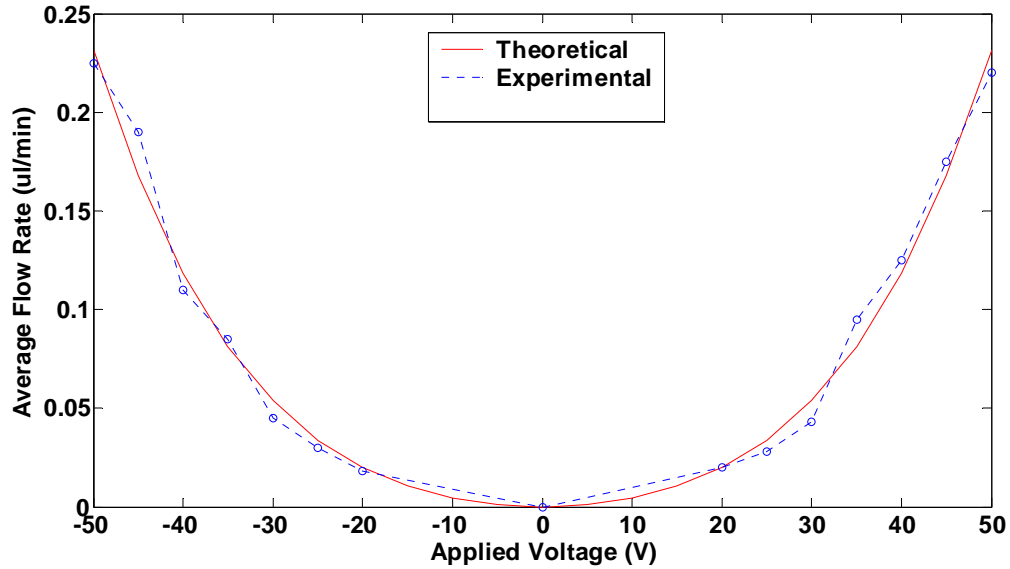
Fig. 5.6. Plot of the time-averaged flow rate of liquid column as a function of applied voltages. The experimental measurements are indicated by (o) and drawn by dashed line. The simulated results using our model are drawn by solid line.

It is also worth noting that the liquid column did not experimentally propagate with the applied voltage less than 20 V. It can be explained that the energy is consumed to overcome the fluid resistance. A minimum average flow rate (at 20 V) was measured approximately at 18 nl/min while its maximum value (at 50 V) was about 225 nl/min. It was also observed that the liquid column completely filled the channel during propagation and removed any particles inside the channel during the propagation.

Although no leftovers and visible alternations were observed on the surface of actuated Cytop™ after liquid pass through, separate research will be carried out for further investigation and characterization of surface properties of the dielectric. It is very helpful to study the reliability and stability of the dielectric to optimize the device design toward commercialization.

To analyze the accuracy of the volumetric dispensing rate, we firstly obtain the volume flow rate by

$$Q = \frac{W \cdot H \cdot L}{t} \qquad (5.2)$$

Here, Q is the volume flow rate, W is the width and H is the height of the channel, respectively. L is the displacement of the meniscus during the time interval t.

Then, we can obtain the logarithm of both sides of the equation by

$$\log Q = \log W + \log H + \log L - \log t \qquad (5.3)$$

Differentiating and obtaining the absolute value of each term in the equation, we can get the accuracy of the volume dispensing rate by

$$\left| d(\log Q) \right| = \left| d(\log W) \right| + \left| d(\log H) + \left| d(\log L) \right| \right| + \left| d(\log t) \right| \quad \Rightarrow$$
$$\left| \frac{dQ}{Q} \right| = \left| \frac{dW}{W} \right| + \left| \frac{dH}{H} \right| + \left| \frac{dL}{L} \right| + \left| \frac{dt}{t} \right| \qquad (5.4)$$

where, dQ/Q denotes the relative accuracy of the volumetric dispensing rate, dW/W and dH/H denote the relative accuracy of the channel width and depth, respectively, dL/L denotes the relative accuracy of the displacement of the meniscus, dt/t represents the relative accuracy of the time interval. dW/W and dH/H are normally determined by the photolithography process parameters such as spin coating speed, exposure power and time and photoresist develop time. Both of them can be controlled around $\pm$ 0.5%~$\pm$ 1% using the equipment and the recipes provided by Institute of Materials Research hand Engineering. dL/L was dependent on the accuracy of the image analysis software. Generally, high accuracy can be obtained when the picture of meniscus motion is taken under high magnification of the microscope. As the pictures in the experiment were taken under low magnification of 5 and 10, the accuracy offered by the image analysis software was about $\pm$ 5% based on the specification of the software. dt/t was dependent on the accuracy of the camera recording the video frames at the

speed of 30 frames/s. The accuracy is less than $\pm$ 0.1% according to the specification of the camera. Therefore, we can get the accuracy of the volumetric dispensing rate at

$$\left|\frac{dQ}{Q}\right| = \left|\frac{dW}{W}\right| + \left|\frac{dH}{H}\right| + \left|\frac{dL}{L}\right| + \left|\frac{dt}{t}\right| = 1\% + 1\% + 5\% + 0.1\% = 7.1\% \qquad (5.5)$$

Thus, the accuracy of the volume dispensation of this dispenser is about $\pm$ 7.1% at 20 V.

5.3 Power Dissipation Analysis

Power dissipation is an essential performance indicator for microfluidic devices and integrated systems. The sensitivity of 1°C or even less for temperature control in some biological applications may be compulsory. In other less sensitive microfluidic applications, thermal dissipation or heat gradient will determine the system or device operational limit. To analyze the power dissipation of our device, we assumed that the liquid was actuated and driven by electrostatic force on the dielectric surface. The liquid driven by capillary force in between the electrodes was ignored. It is assumed that the initial water volume is 1 μl actuated and driven under 20 V. Figure 5.7 shows the equivalent electrical circuit of the simplified model system in which the liquid is actuated and driven along the Cytop™-coated electrode.
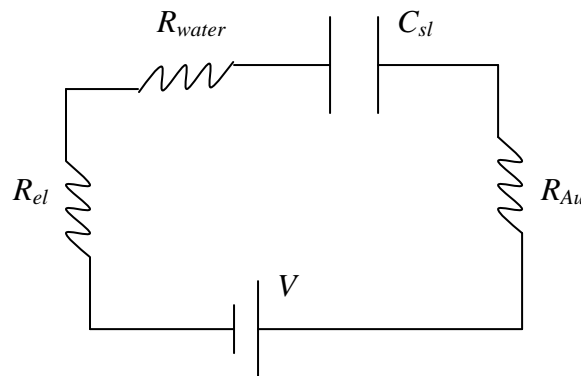
Fig. 5.7 The equivalent electric circuit of the system model.

When the liquid fully covers the charged electrode, the capacitance (C_{sl}) between the liquid and the charge electrode is approximated to 20 pF, calculated by Verheijen *et al.* [286]. The other resistances in series with the liquid-solid capacitor consists of the resistance R_{el} caused by the electrical wire connection (50 Ω), resistance of water R_{water} (1 MΩ) and resistance of gold pad R_{Au} (10 Ω) as shown in Figure 5.7.

The current delivered to the solid-liquid capacitor is obtained by:

$$I(t) = \frac{dq}{dt} = V(t)\frac{dC}{dt} + C(t)\frac{dV}{dt} \tag{5.6}$$

Here, q is the electrical charges, $C(t)$ and $V(t)$ is the time-varying capacitance and voltage respectively, and t is the time. The instantaneous power delivered to time-varying capacitance can be obtained by neglecting the voltage time-dependence which is very small:

$$P = \int V_0^2 \cdot Cdt = V_0^2 \cdot C_t \tag{5.7}$$

Here P is the instantaneous power, V_0 is the applied voltage (20 V) and C_t is the instantaneous capacitance (20 pF). Thus, for the model described above the average power dissipation with a moving period of 1 s is approximately 8 mW and the corresponding energy consumption is about 8 μJ.

In addition, the electrical power is also dissipated inside the liquid to overcome the fluid resistance for liquid motion. The total energy dissipated resistively in the liquid can be obtained by

$$P_{res} = V_0^2 C_t \frac{R_{water}}{R_{total}} \tag{5.8}$$

Here R_{total} is the total series resistance and P_{res} is the electrical power dissipated resistively in the model. In this case, as the total resistance almost equals to the water resistance, the total energy is approximately 8 μJ and the average electrical power

dissipation inside the liquid is 8 mW due to the high resistance of water. We assume that all the dissipated energy inside the liquid is completely converted into heat and there is no heat transfer between the liquid and the environment because the time interval (less than nano second) is too small for heat transfer in practice.

5.4 Experimental Limitations

5.4.1 Liquid Evaporation at Microscale

All the above-mentioned approaches to measure the liquid column velocity are influenced by evaporation of liquid (pure water) in air in terms of accuracy, precise control and liquid volume maintenance. Moreover, evaporation of liquid varies ion concentration in the liquid due to the escape of liquid (pure water) molecules, which accounts for slight modifications of certain properties such as surface tension / energy as well. This effect is much greater at microscale than at macroscale. Therefore, the issue of liquid evaporation of microfluidics was preliminarily studied to evaluate its importance and to determine an optimized time scale for conducting experiments and operating devices.

A simple experiment was performed using pure water under room temperature of 20°C and humidity of 40 %. Water droplets were manually dispensed by a micro pipette onto a Cytop™ surface and the inlet of the microchannel of a fabricated device then driven into the channel by capillary force respectively. Both testing samples were exposed to evaporate in air. Subsequently, the water volume as a function of time was investigated. A weighting balance (Mettler Toledo TA261) with a readability of 0.01 mg working together with a data acquisition system in a connect PC was used to collect the data of weight loss instead of volume loss of water droplets. Microdroplets

of water with initial volumes of various nominal values of 1.0 µl, 3.0 µl, 5.0 µl, and 10.0 µl were tested under both exposed and unexposed conditions mentioned above. The smallest and largest nominal volume represent the typical volumes for device pumping experiment while the medium volumes stand for the typical volumes for contact angle measurement. Note that there is an inaccuracy of ± 2.5-12 % in the sub-microliter with the micro pipette (Eppendorf Reference$^{®}$) to manually dispense droplets according to its technical specifications. The water droplet volume normalized with respect to the initial measurement, as a function of time is plotted in Figure 5.8. A maximum suitable or applicable experimental period should be approximated when the tested liquid volume is sensitive in air.
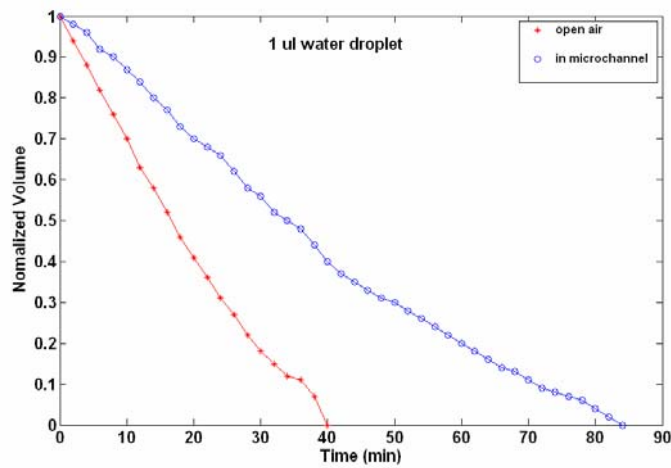
(a)
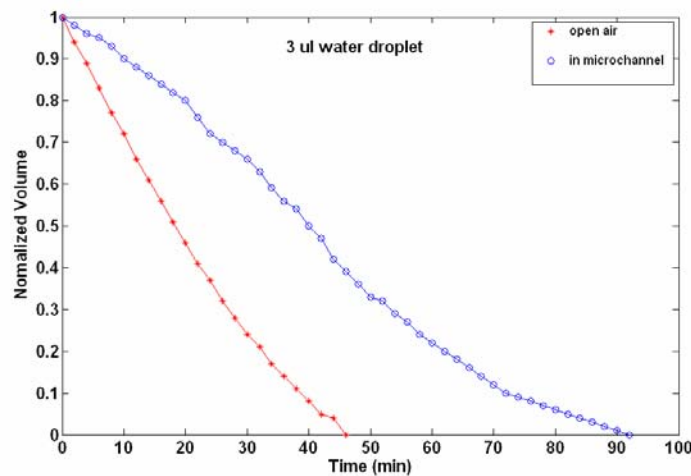
(b)
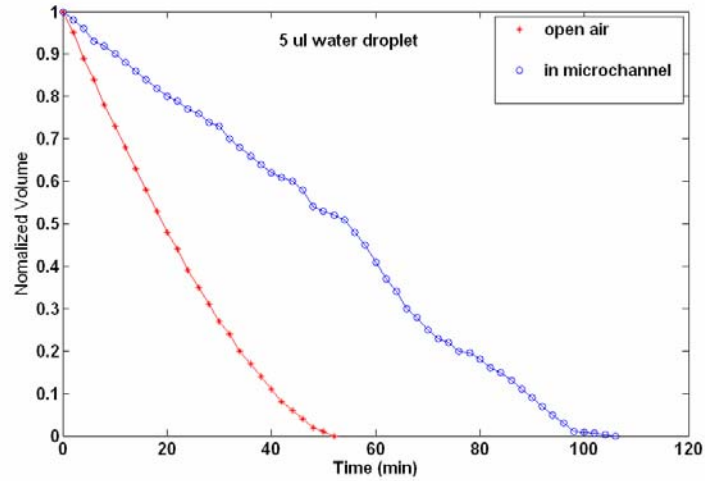
(c)
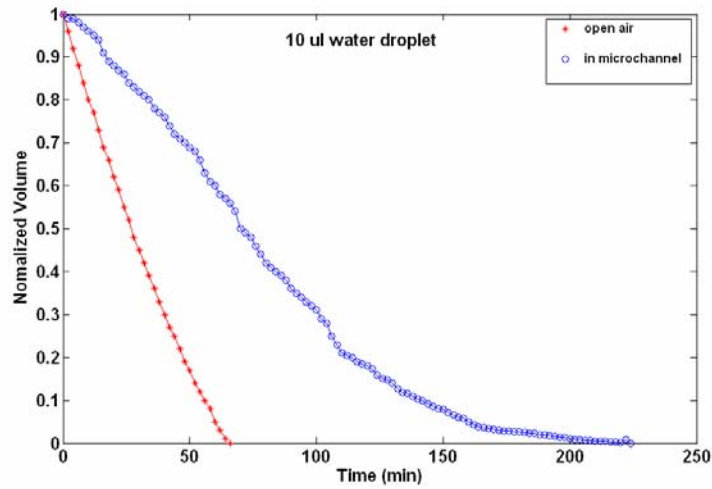
(d)

Fig. 5.8 Evaporation as a function of time for water droplet of 1.0, 3.0, 5.0 and 10.0 μl placed on Cytop™ surface in air and fabricated microchannel, respectively.

When exposed to open air, the smallest 1.0 μl water droplets sharply evaporate 10 % of their volume within 3 minutes while the largest 10 μl water droplets lose 10 % of their volume within 10 minutes. The typical sizes of water droplets 3μl and 5μl for contact angle measurement experiment lose their 10 % volume within 4-5 minutes. Based on this, the time duration for a single contact angle measurement experiment described in Chapter 2 was controlled within 1-2 minutes.

On the other hand, when these water droplets are dispensed into the fabricated microchannel, their evaporation rates are significantly reduced. To compare it by evaporating 10 % of volume, it takes about 10, 12, 15 and 20 minutes for 1, 3, 5 and 10 μl water droplets, respectively. It indicates that the device performance has a poor dependence on evaporation. Therefore, proper design and methods should be implemented to minimize the evaporation effect in microfluidic systems and devices. However, evaporation effect makes it difficult to achieve precise control of liquid volume at micro- or even submicro-meter scale.

5.4.2 Dielectric Degradation

The stability and reliability of dielectric (Cytop™) raised another experimental concern during the course of experiment. The degradation of dielectric was sometimes observable to produce surface tension variations across the interface solid-liquid in the microchannel. Figure 5.9 shows the detailed images of sequential receding procedure of water column, which was resulted from Cytop™ dielectric degradation.

It was found that the liquid column sometimes tended to recede several tens seconds to minutes after breaking the apply of potential. The leading edge of water column stopped at the 11th electrode under an applied voltage of 20 V as shown in Figure 5.9(a). Having removed the voltage apply for several tens seconds to minutes, the liquid column started continuously receding as shown in Figure 5.9(b) and (c) until a new equilibrium balance reached and it stopped again. Visibly, the leading edge of meniscus receded toward to the 8th electrode as shown in Figure 5.9(d).

(a)   (b)

(c)   (d)
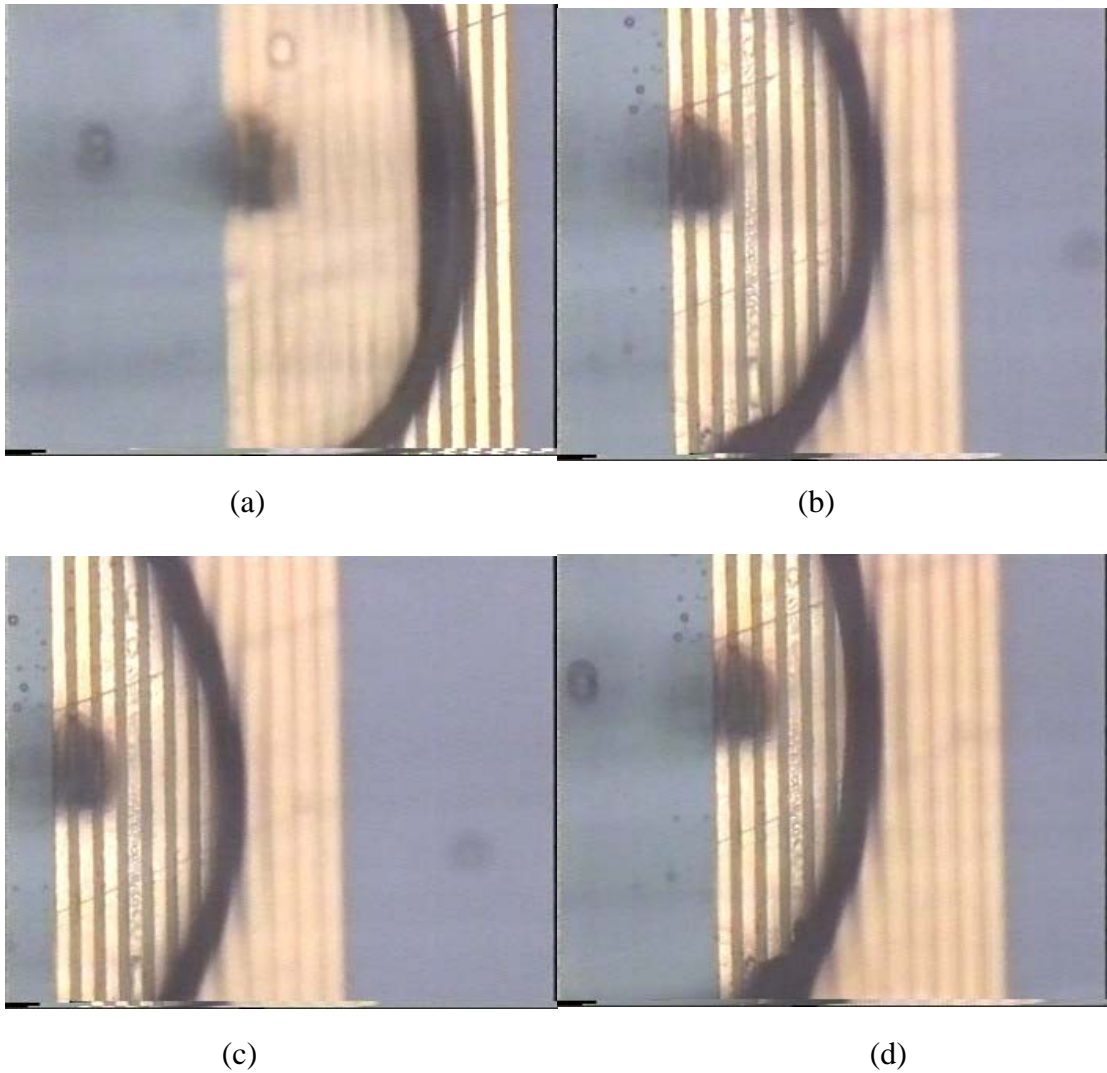
Fig. 5.9 The dielectric degradation effect to make the liquid column receding.

Manipulation of the dielectric thickness, ion concentration of water, magnitude time of applied voltage has no observable impact on changing the geometrical location or magnitude of this dielectric degradation effect. It clearly indicates that this effect is due to the electrical insulation or dielectric degradation. We were not able to further distinguish the physics of the degradation phenomenon whether it originated from trapped charges or modification of chemical property of Cytop™ surface, which was beyond the project scope. As mentioned in Section 5.2, the actuated Cytop™ surface property should be further characterized, which can be helpful for understanding and explaining the degradation effect.

5.4.3 Curve Shape of Meniscus

Firstly, during the course of experiment, the liquid meniscus was observed to have a curve shape upon potential actuation of the dielectric layer. This phenomenon was resulted from the capillary force at the side wall of the channel, the material of which was SU 8 photoresist. Referring to Figure 5.5, the liquid column stops at the hydrophobic coated electrodes locating on the top and bottom of the channel. However, the side wall material was directly in contact with the liquid all along the channel. Once the meniscus was electrically activated to propagate, the capillary force from the side wall will force the meniscus to form a curve shape, the curvature of which was dependent on the magnitude of the capillary force.

To incorporate this side wall effect into the develop model (Equation 3.34 and 3.35), a functional dependence factor f (Equation 3.17) was introduced into the mathematic model derived from the Navier-Stokes equation and Young-Lippmann equation. However, the Young-Lippmann equation was over simplified so that many factors such as surface roughness etc., which may affect the functional dependence of contact angle change in some aspects, was assumed negligible. In this case, the side wall effect from the SU 8 photoresist, surface roughness of the channel together with other materials properties of substrate and liquid itself were considered as a combined contribution to determine the exact functional dependence of contact angle on applied potential. Hence, this side wall effect on the curve-shape of the liquid meniscus could be reflected from this functional dependence factor f. Based on the experimental results of the flow rate (in volume), a standard deviation of less than 10 nl/min was obtained, which was acceptable for this device. Away from the side wall, it can be seen from Figure. 5.5 that the meniscus is straight as we would expect.

The above comments apply to a well-fabricated device where the thickness of the Cytop layer was large enough to achieve hydrophobicity. For Figure 5.9, it was observed that at locations far away from the wall, the meniscus not straight as it should be. The reason for this could be the cytop layer was too thin. In the plasma etching process, the residual Cytop was supposed to be removed by oxygen plasma (RIE) followed by photoresist striping to form the patterned Cytop layer. The desirable thickness of the Cytop was about 700 nm, shown in Figure 5.10(a).
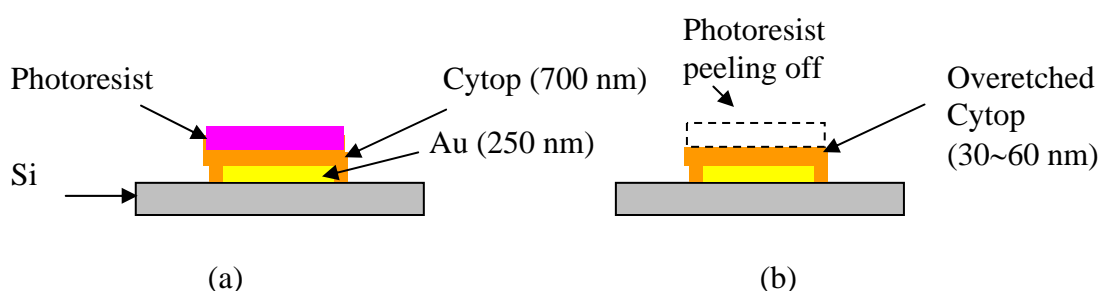
Fig. 5.10. The patterning process of Cytop layer. (a) the desirable thickness of Cytop is about 700 nm after plasma etching of residual Cytop and photoresist stripping; (b) Due to the adhesion problem of photoresist (AZ4620) with Cytop, the masking layer of AZ4620 peeled off causing the overetch of Cytop layer during the plasma etching process.

However, due to the hydrophobic surface of Cytop, the adhesion between the photoresist AZ4620 and Cytop was not very stable and the photoresist could peel off during the plasma etching process, as shown in Figure 5.10(b). The thickness of the overetched Cytop in several fabricated chips was measured at only 30~60 nm using profilemeter.

To clarify this issue, a new device was fabricated to study the thickness effect of dielectric (Cytop) on the curve shape of the liquid meniscus. Referring to the fabrication process in Appendix B, after process B1(e), REI process was used again to etch the Cytop layer to obtain a thickness in the range of 30~60 nm. The thickness range was confirmed by measurement using a profilemeter. Then the fabricated device

was tested under the same conditions mentioned in Section 5.2. Figure 5.11 shows

snap shots of the motion of the meniscus in the newly fabricated device, in which the

Cytop thickness is as thin as 30~60 nm.

(a)   (b)

(c)   (d)
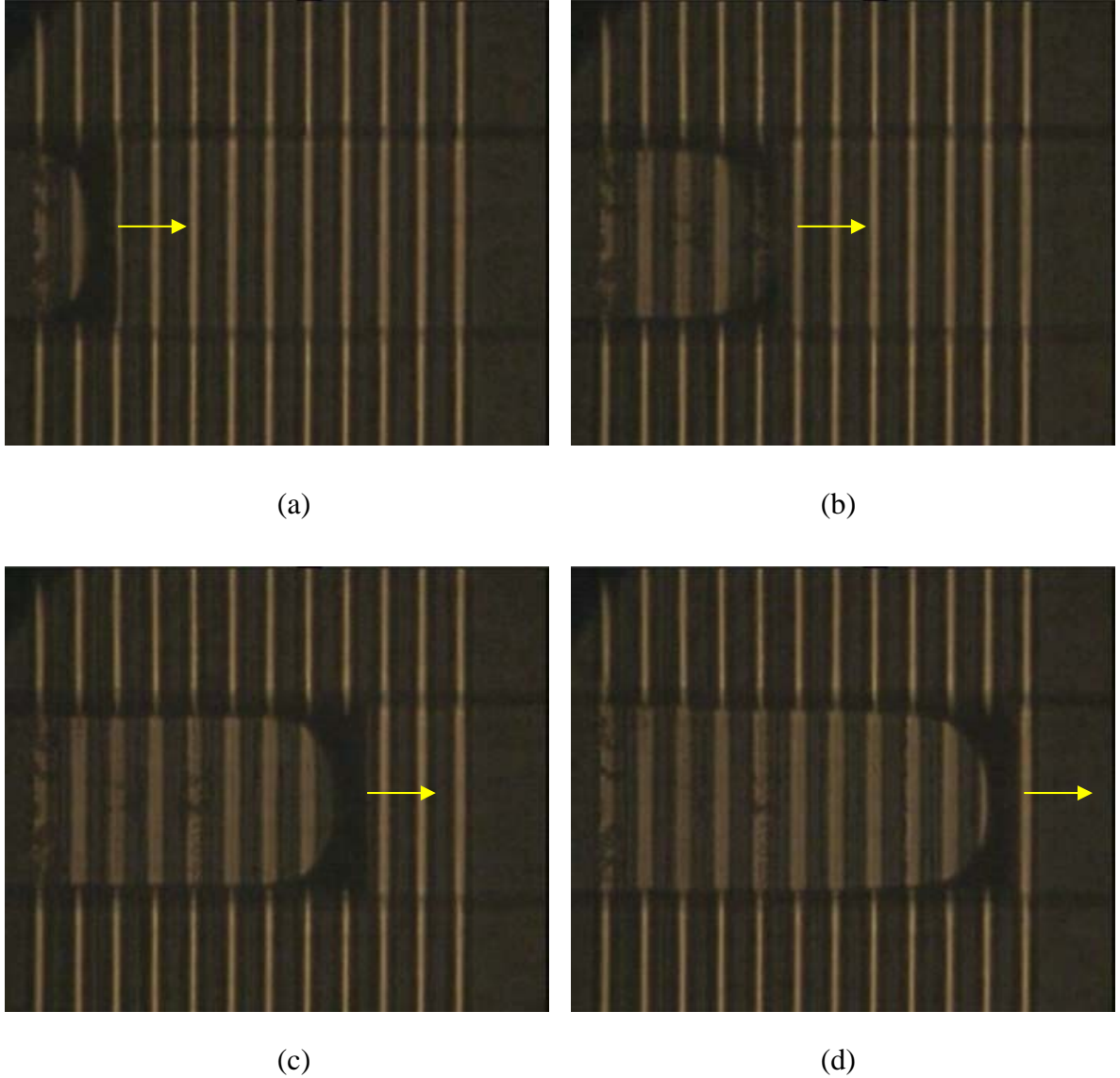
Fig. 5.11. The snap shots of the liquid motion (from left to right) using the newly fabricated device for verification of the curve shape of the meniscus. The channel width is 100 µm. The electrodes in the order of odd numbers (the 1st electrode is in left hand side) were coated with Cytop™ while the even-numbered electrodes were bare.

As can be seen from Figure 5.11, the liquid propagated into the channel and

stopped at the 1st electrode, which was coated by Cytop. A curve shape of the liquid

meniscus was observed, as shown in Figure 5.11(a). After electrical actuation, the

liquid propagated again and stopped at the 3rd electrode (coated by Cytop) as shown in Figure 5.11(b). Figures 5.11(c) and (d) show the liquid stopping at the 7th and 9th electrode coated by Cytop, respectively. A curve shape of the meniscus was observed during the experiment.

From this experiment, it is verified that the curve shape of liquid meniscus was due to the small thickness (30 – 60 nm) of the Cytop layer in the devices fabricated using the old process. As the thickness (30 ~60 nm) was much smaller than the desired thickness (700 nm), the Cytop-coated electrode was not able to eliminate the curve shape of the liquid meniscus. To eliminate the problem, the time for hard baking of photoresist was increased from 10 minutes to about 30 minutes.

5.5 Competitiveness

Based on the testing results illustrated above, the specifications and features of this innovatively developed microfluidic dispenser are compared with the well-recognized electrowetting-on-dielectric based actuator and micropump developed by Prof. C.-J. Kim's Micromanufacturing Lab at UCLA and Prof. R. B. Fair' Digital Microfluidics research group at Duke University, as listed in Table 5.1. This table is useful to assess the performance of this device since all that required to convert the dispenser into a pump is to connect it to a source of air pressure.

The employment of liquid metal (mercury) by the EWOD actuated micropump developed by C.-J. Kim etc. [194] inherently exposes severe problems for fabrication process and application due to its material toxicity. Although it can be operated at the lowest voltage, a slightly higher voltage will induce a severe damage to the device causing electrolysis and liquid metal split. It is very difficult to control the applied

voltage. Hence, the development of this micropump is still at lab stage and far from

commercialization.

Table 5.1 The Comparisons between the presented dispensing device and
other well-known EWOD based actuator and micropump.

Specs. Authors	Voltage / Power	Flow Rate	Actuated Fluid Type	Reliability	Features
C.-J. Kim, etc. [194]	2.3 V / 170 mW	70 μl/min	Continuous liquid (pushed by liquid metal)	20 hrs or 2×10^6 cycles at 2.3 V and 25 Hz	• Low power consumption and low voltage • Continuous liquid flow • Fabrication complexity and materials toxicity for commercialization. • Higher voltage (2.3-3 V) causes performance degradation , electrolysis and liquid metal (mercury) split. • Patented
R. B. Fair, etc. [139,231]	15-150 V (DC)	10 cm/s at 60 V nano-microliter / min	Liquid droplets	10^5 cycles	• Manipulation of aqueous droplets ranging from nanoliters to microliters in volume. • Instability due to higher voltage on the liquid-oil film, which leads to adsorption for protein onto Teflon. • Patented
D. Saman & H. Liu [265]	20 V / 8 mW	18 nl/min (0.15mm/s at 20 V)	Continuous liquid column or droplets	Under investigation	• In-built metering feature • Continuous liquid / droplets manipulation in nano/pico/femto liter range. • Dielectric degradation observable. • Low power consumption and low voltage • Patented and towards commercialization.

The EWOD-based actuator for digital microfluidic application developed by R.

B. Fair etc. [139,231] is only able to manipulate liquid droplets surrounded by silicone

oil instead of continuous liquids. This device employs Parylene C as the primary

dielectric and a thin layer of Teflon® AF 1600 to provide an adequately-hydrophobic

surface. The device performance greatly depends on this combination of the

dielectrics, which require moderate or very high driving voltage (15-150V) and limit

the working cycles (10^5) and exhibit instability due to adsorption of protein by Teflon under high voltage.

The microfluidic dispenser in this project utilizing Cytop™ as dielectric has an in-built metering feature to manipulate continuous liquids in air. EWOD manipulation of liquids in air is more challenging than in silicon oil environment. The lower angle and higher contact angle hysteresis in air make the manipulation more difficult than in an immiscible liquid [232]. Hence, it will be more useful to operate EWOD in air in terms of liquid manipulation and suitability for any biomedical applications. Our device is operable under low voltage (20 V) and low power dissipation (8 mW) to generate nano or even pico liter range of fluid volume, which only depends on the lithography technology. Although dielectric degradation is observable, the desirable stability and reliability for commercialized products can be achieved by several methods, such as precise control of applied voltage, employment of a separate hydrophobic layer while Cytop as the primary dielectric etc.. In combination with a pneumatic pump, the liquid volume can be manipulated / controlled precisely in the range of sub-micro liter to pico liter.

CHAPTER 6

CONCLUSIONS AND FUTURE WORKS

A self-priming and hydrophobicity controlled microfluidic dispenser having in-built metering feature for dispensing varying liquid column based on EWOD was developed in this dissertation. A PCT patent application with respect to this technology was filed and published on November 2, 2006 with an international publication no. WO 2006/115464 A1. This chapter concludes the project studies on the aspects of literature reviews, dielectric materials experimental study, device design and theoretical and numerical study, and testing results.

6.1 Conclusions

Surface tension is a dominant force over than other forces for liquid handling and actuation in microscale. The literature review on the development of the micropump technology clearly show the limitations of traditional micropumps, which are difficult to be implemented in the remote environmental monitoring systems, implantable medical devices and chemical analysis system, where low power consumption and low driving force are critical issues. Furthermore, very few microfluidic intellectual properties so far relates to any of the commercially-available products. Therefore, this project has been motivated to study the dispensing behavior of a hydrophobicity

controlled microfluidic dispenser, in which the liquid volume can be manipulated by EWOD. This microfluidic dispenser with an in-built metering feature can be integrated into a lab-on-a-chip performing specific chemical analysis, clinical diagnostic and environmental morning

The performance of the electrowetting-on-dielectric (EWOD) device depends heavily on the dielectric or the insulation layer properties rather than that of fluid or electrode. Theoretically, there are no dielectric materials which exhibit both high dielectric strength and high dielectric constant, and compromise is needed to meet the practical requirements. The dielectric breakdown analysis demonstrates that 35° of contact angle variation of Cytop™ can be achieved at as low as 65 V to actuate EWOD, which is the most competitive among the dielectrics reported and employed in EWOD. Good reversibility of Cytop™ based on the contact angle measurement results indicates that EWOD performance can be greatly improved by incorporating this material in the device. The results of contact angle measurement are in good agreement with the theoretical prediction by Young-Lippmann equation and the results from other researchers.

The conceptual design and working principle of this microfluidic dispenser are demonstrated and successfully verified by a proof-of-concept device. The conceptual design is totally new in the micro/nano fluidic device design and application. Additionally, the low power consumption and low voltage make it very attractive for applications which require an ultra miniature metering microfluidic device.

The governing equation with respect to the redistribution of surface charge density is presented to demonstrate the hydrodynamics of liquid-solid interfacial tension. Upon applying the voltage potentials, a free charge distribution is built-up at the liquid-solid interface to generate an electrostatic force acting on the tri-phase

contact lines to pull the liquid column forward. The interfacial charge density accounts for the generation of non-uniform electric field and potential distribution. The surface charge and electric field distribution are obtained through the finite-element simulation, by solving the corresponding partial differential equations using FlexPDE.

Consequently, the electrostatic force resulted from the redistribution of free surface charges induced by the non-uniform electrical field is modeled to show its dependence of the magnitude and direction on the electric field distribution as a geometrical function of the liquid. It can be decomposed into a horizontal component and a vertical component. The horizontal electrostatic force is independent of contact angle while the vertical component increases reversely with contact angle. It potentially provides a new contribution to explain contact angle saturation phenomenon. The obtained expression of horizontal force is identical to the results achieved by other researchers using different methods.

Based on the above analysis, a new hydrodynamic mathematical model of the time-averaged liquid column velocity governed by the Navier-Stokes equation is developed to compute the velocity profile. The average flow rate and principle radius of liquid meniscus as a function of time are predicted respectively. The electrostatic force, which affects the dependence factor $f(\cos\theta)$, is considered as a function of the average flow rate. Finally, we present the numerical and analytical solutions to demonstrate the physics of EWOD.

The proposed hydrophobicity-controlled microfluidic dispenser was fabricated using MEMS microfabrication technology and tested to evaluate its feasibility and applicability for the implementation of environmental monitoring and biomedical systems. Based on the video frame analysis, the experimental data of a standard deviation of less than 0.01 μl/min agrees well with our model of the simulated time-

averaged flow rate. The fluid flow can be electrically actuated to propagate at a flow rate of 18 nl/min under a voltage of as low as 20 V. The proper device design significantly reduces the evaporation effect. The controlled hydrophobicity actuation fully utilizes the surface tension as the driving force in the micro/nano/pico scale. This microfluidic device does not require a dedicated actuator for dispensing. Furthermore, it has an inbuilt metering feature which can be used to delivering a measured volume of liquid in the range of a few milliliters to a few picoliters.

Although dielectric degradation effect was observed after removing the applied voltage, the device performs well under driving voltage and no leftovers were found on top of dielectric layer. It is convincing that the stability and reliability of this device are absolutely better than that of reported EWOD device. By comparisons with other well-known developed and patented EWOD based micropumps and actuators, the presented microfluidic dispenser has great significances and potentials in terms of applications.

6.2 Future Works

Overlooking the future works of this project, there are many challenging issues and directions ahead for further development of this technology. The physics behind electrowetting and electrowetting-on-dielectric (EWOD) and wetting kinetics are the most stringent job for fundamental study. Particularly, it requires further investigation on the instabilities of wetting line and contact angle saturation effect under high electric field. It also needs more elaborative theoretical illustration of the electrohydrodynamics of the three-phase contact line to clarify the EWOD origination, which will enable the development of tangible and valuable model for liquid transport. Nevertheless, the liquid behaviours under electrical field should be further studied to provide more methods for manipulation and build wider range of applications.

Materials issues, particularly the dielectrics, become another focused and interesting topic of future research. The dielectric layer should be able to accommodate a high-performance EWOD device with insulating, electrowetting, liquid compatibility and stability simultaneously. This issue is still being investigated by EWOD researchers. We explored the feasibility of using a metal oxynitride thin film as dielectric material. However, its hydrophobicity was not adequately satisfactory. The degradation of Cytop™ may induce a severe problem, which limits the reliability of the device performance. Approaches should be explored to minimize its magnitude of effect through further characterization to understand its physics. An additional hydrophobic layer on top of Cytop™ could be a potential solution to this problem.

Future work at the device level should be focused on structural optimization and characterization of operations. The devices with other featured dimensions should be tested to obtain the optimized parameters for device design and operation at low driving voltage and power consumption. On the other hand, physical integration of a EWOD system with a multiplexer controlled by an embedded algorithm will offer a better way to achieve precise and fast control for next-generation system.

Biocompatibility testing using biological or physiological fluids is another key issue in ensuring its transportability for biomedical applications. These biological fluids contain proteins which tend to adsorb by any surface in contact. For instance, the adsorption of protein to Cytop™ should be investigated and characterized to establish the compatibility of such fluids with EWOD systems.

Bibliography

[1]   Andrew E. K., Proliferation of Microfluidics in Literature and Intellectual Property, *Lab Chip*, Vol. 4, 16-20, 2004.

[2]   Burns MA, Johnson BN, Brahmasandra SN, Handique K, Webster JR, *et al*., An Integrated Nanoliter DNA Analysis Device. *Science,* Vol. 282,484–487, 1998.

[3]   Knight JB, Vishwanath A, Brody JP, Austin R.H., Hydrodynamic Focusing on A Silicon Chip: Mixing Nanoliters In Microseconds. *Phys. Rev. Lett.* 80:3863–6, 1998.

[4]   Clark RA, Ewing AG., Experimenting in Picoliter Microvials, *Chemtech.,* 28(2):20–25, 1998.

[5]   Crofcheck CL, Grosvenor AL, Anderson KW, Lumpp JK, Scott DL, Daunert S., Detecting Biomolecules in Picoliter Vials Using Aequorin Bioluminescence, *Anal. Chem.* 69(23):4768–72, 1997.

[6]   C.-M. Ho, Fluidics – The Link Between Micro and Nano Sciences and Technologies, *IEEE International Conference on MEMS*, Interlaken, Switzerland, pp.375-384, 2001.

[7]   Heller C., Principles of DNA Separation with Capillary Electrophoresis, *Electrophoresis*, Vol. 22, pp.629-43, 2001.

[8]   Rech I., Cova S., Restelli A., Ghioni M., Chiari M. and Cretich M., Microchips and Single-photon Avalanche Diodes for DNA Separation with High Sensitivity, *Electrophoresis*, 2006, 27, pp.3797-3804.

[9]   S.H. Chiou, M.F. Huang and H.T. Chang, Separation of Double-stranded DNA Fragments by Capillary Electrophoresis: Impacts Of Poly(ethyleneoxide), Gold Nanoparticles, Ethidium Bromide, and pH, *Electrophoresis*, 2004, 25, pp.2186-2192.

[10]   Y.N. Shi, DNA Sequencing and Multiplex STR Analysis on Plastic Microfluidic Devices, *Electrophoresis*, 2006, 27, pp.3703-3711.

[11]   L.G. Song, D.H. Liang, Z.J. Chen, D.F. Fang and B. Chu, DNA Sequencing by Capillary Electrophoresis Using Mixtures of Polyacrylamide and Poly(N,N-dimethylacrylamide), *Journal of Chromatography A,* Volume 915, Issues 1-2, 27 April 2001, Pages 231-239.

[12]   Brian M Paegel, Robert G Blazej and Richard A Mathies, Microfluidic Devices for DNA Sequencing: Sample Preparation and Electrophoretic Analysis, *Current Opinion in Biotechnology,* Volume 14, Issue 1, February 2003, Pages 42-50.

[13]   M. U. Kopp, A. J. D. Mello and A. Manz, Chemical Amplification: Continuous-Flow PCR on A Chip, *Science*, Vol. 280, pp.1046-1048, 1998.

[14]   S. H. Wang, J. K. Wen, *et al*., Identification and Characterization of Bacillus Anthracis by Multiplex PCR on DNA Chip, *Biosensors and Bioelectronics,* Volume 20, Issue 4, 1 November 2004, Pages 807-813.

[15]   Hang Lu, Martin A. Schmidt and Klavs F. Jensen, A Microfluidic Electroporation Device for Cell Lysis, *Lab Chip*, 2005, Vol. 5, pp.23 – 29.

[16]   Dino Di Carlo, Cristian Ionescu-Zanetti, Yolanda Zhang, Paul Hung and Luke P. Lee, On-chip Cell Lysis by Local Hydroxide Generation, *Lab Chip*, 2005, Vol. 5, pp.171 – 178.

[17]   Sang-Wook Lee and Yu-Chong Tai, A Micro Cell Lysis Device, *Sensors and Actuators A: Physical*, Volume 73, Issues 1-2, 9 March 1999, Pages 74-79.

[18]   Hatch, A.; Garcia, E.; Yager, P., Diffusion-based Analysis of Molecular Interactions in Microfluidic Devices, *Proceedings of IEEE*, Volume 92, Issue 1, Jan 2004, Page(s):126 – 139.

[19]   James P. Brody and Paul Yager, Diffusion-based Extraction in A Microfabricated Device, *Sensors and Actuators A: Physical,* Vol. 58**,** 1997, pp.13-18.

[20]   Suzuki H., Chih-Ming Ho, Kasagi N., A Chaotic Mixer for Magnetic Bead-based Micro Cell Sorter, *J. MEMS*, Volume 13, Issue 5, Oct. 2004 Page(s):779 – 790.

[21]   Deval J., Tabeling P., Chih-Ming Ho; A Dielectrophoretic Chaotic Mixer, *Proceedings of The Fifteenth International Conference on Micro Electro Mechanical Systems*, 20-24 Jan., 2002, Page(s):36 – 39.

[22]   Gooding, J.J. Electrochemical DNA Hybridization Biosensor, *Electroanalysis*, 14, pp.1149-1156, 2002.

[23]   T. Gregory D., M. G. Hill, J. K. Barton, Electrochemical DNA Sensors, *Nature Biotechnology*, Vol. 21, No. 10, Oct. 2003, pp. 1192-1199.

[24]   van Lintel, H. T. G., van den Pol, F. C. M., and Bouwstra, S., 1988, A Piezoelectric Micropump Based on Micromachining in Silicon, *Sens. Actuators*, 15, pp. 153–167.

[25]   van den Pol, F. C. M., van Lintel, H. T. G., Elwonspoek, M., and Fluitman, J. H. J., 1990, A Thermopneumatic Micropump Based on Micro-Engineering Techniques, *Sens. Actuators A*, 21–23, pp.198–202.

[26]   Zengerle, R., Kluge, S., Richter, M., and Richter, A., 1995, A Bi-Directional Silicon Micropump, *IEEE 8th Int. Workshop on MEMS-MEMS'95*, pp. 19–24.

[27]   Benard, W. L., Kahn, H., Heuer, A. H., and Huff, M. A., 1998, Thin Film Shape-Memory Alloy Actuated Micropumps, *Journal of MEMS*, **7**, No. 2, pp. 245–251.

[28]   Grosjean, C., and Tai, Y. C., 1999, A Thermopneumatic Peristaltic Micropump, *Inter. Conf. on Solid-State Sensors and Actuators (Transducers '99)*, pp.1776–1779.

[29]   Stemme, E., and Stemme, G., 1993, A Valveless Diffuser/Nozzle-Based Fluid Pump, *Sens. Actuators A*, 39, pp. 159–167.

[30]   Fuhr, G., Hagedorn, R., Mueller, T., Benecke, W., and Wagner, B., 1992, Microfabricated Electrohydrodynamic (EHD) Pumps for Liquids of Higher Conductivity, *Journal of MEMS*, 1, No. 3, pp. 141–145.

[31]   Harrison, D. J., Manz, A., and Glavina, P. G., 1991, Electroosmotic Pumping Within a Chemical Sensor System Integrated on Silicon, *Proc. of Inter. Conf. on Solid-State Sensors and Actuators Transducers'91*, pp. 792–795.

[32]   Takagi, H., Maeda, R., Ozaki, K., Parameswaran, M., and Mehta, M., 1994, Phase Transformation Type Micropump, *Proc. of Micro Mechatronics and Human Sciences 94*, pp. 199–202.

[33]   Yanagisawa K, Kuwano H. and Tapo A., 1993, An Electromagnetically Driven Microvalve, *Proc. Transducers'93,* pp.102–5.

[34]   Fu C, Rummler Z. and Chomburg W., 2003, Magnetically Driven Micro Ball Valves Fabricated by Multilayer Adhesive Film Bonding, *J. Micromech. Microeng.,* 13**,** S96–102.

[35] Yobas L, Huff M. A., Lisy F. J. and Durand D. M., 2001, A Novel Bulk Micromachined Electrostatic Microvalve with A Curved-compliant Structure Applicable for A Pneumatic Tactile Display, *J. Microelectromech. Syst.,* 10, pp.187–96.

[36] Li H. Q., Roberts D. C., Steyn J. L., Turner K. T., Yaglioglu O., Hagood N. W., Spearing S. M. and Schmidt M. A., 2004, Fabrication of A High Frequency Piezoelectric Microvalve, *Sensors Actuators A*, 111**,** pp.51–6.

[37] Ho C-M, Yang X, Grosjean C. and Tai Y-C., 1998, A MEMS Thermopneumatic Silicone Rubber Membrane Valve, *Sensors Actuators* A, 64**,** pp.101–8.

[38] Yang X, Grosjean C. and Tai Y-C, 1999, Design, Fabrication, and Testing of Micromachined Silicone Rubber Membrane Valves, *J. Microelectromech. Syst.,* 8**,** pp.393–402.

[39] C. Ye and D. Li, Electrophoretic Motion of Two Particles in A Rectangular Microchannel, *Microfluidics and Nanofluidics*, 2004, 1, 52–61.

[40] Guangyi Shi, Qiang Huang, Li W. J., *et al.*, Micro Channel Fabrication in PMMA Substrates Using CO/Sub 2/ Laser and Sacrificial Mask Process, *Proceedings of International Conference on Information Acquisition*, 21-25, June 2004, Page(s):116 – 121.

[41] Kendra V. Sharp, Ronald J. Adrian, et. al., Chapter 6, Liquid Flows in Microchannel, In *The MEMS Handbooks*, edited by Mohamed Gad-el-Hak, pp 6-1—6-38, 2001.

[42] K. B. Li, L. W. Lin, Surface Micromachined Glass and Polysilicon Microchannels Using MUMPs for BioMEMS Applications, *Sensors and Actuators A*, 2004, 111, pp.44-50.

[43] Melin J. and G. Giménez, *et al.*, A Fast Passive and Planar Liquid Sample Micromixer, *Lab on a Chip,* 2004, *Vol.* 4, 214-219**.**

[44] Miyake R. *et al.,* Micro Mixer with Fast Diffusion, *Proc. MEMS'93, 6th IEEE Int. Workshop MicroElectromechanical System (San Diego, CA), 1993,* pp. 248–53.

[45] Voldman J., Gray M. L. and Schmidt M. A., An Integrated Liquid Mixer/Valve, *J. Microelectromech. Syst.,* 2000*,* 9**,** pp.295–302.

[46] Hong C. C., Choi J. W. and Ahn C. H., A Novel In-plane Microfluidic Mixer with Modified Tesla Structures, *Lab on a Chip,* 2004, 4**,** pp.109–13.

[47] Liu R. H. *et al.,* Passive Mixing in A Three-dimensional Serpentine Microchannel, *J. Microelectromech. Syst., 2000,* 9, pp.190–7.

[48] Petersen K. and Brown J., High-precision, High-performance mass-flow Sensor with Integrated Laminar Flow Micro-channels, *Proceedings of Trnasducer'85*, 1985, pp.361-363.

[49] Lammerink T. S. J., Tas N. R., Elwenspoek M. and Fluitman J. H. J., Micro-liquid Flow Sensor, *Sensors and Actuators A*, 1993, 37/38, pp.45-50.

[50] Stemme G., A CMOS Integrated Silicon Gas-flow Sensor with Pulse-modulated Output, *Sensors and Actuators A*, 1988, 14, pp.293-303.

[51] Van Der Wiel J., Linder C. and De Rooij N. F., Liquid Velocity Sensor Based on the Hot-wire Principle, *Sensors and Actuators A*, 1993, 37/38, pp.693-697.

[52] Christopher J. Morris *et al.,* Self-assembly and Characterization of Marangoni Microfluidic Actuators, 2006, *J. Micromech. Microeng.,* 16, pp.972-980.

[53] Svetlana M. Mitrovski and Ralph G. Nuzzo, An Electrochemically Driven Poly(dimethylsiloxane) Microfluidic Actuator: Oxygen Sensing And Programmable Flows and pH Gradients, *Lab Chip*, 2005, 5, pp.634 – 645.

[54] M.E. Harmon, M. Tang, C.W. Frank, A Microfluidic Actuator Based on Thermoresponsive Hydrogels, *Polymer,* 44(16), pp.4547-4556, 2003.

[55] Park, J., *et al.*, 2001, Development of A Compact Displacement Accumulation Actuator Device for Both Large Force and Large Displacement, *Sensors and Actuators, A: Physical*, A 90, pg. 191-202.

[56] Chen, F., Xie, H. and Fedder, G.K., 2001, A MEMS-Based Monolithic Electrostatic Microactuator for Ultra-Low Magnetic Disk Head Fly Height Control, *IEEE Transactions on Magnetics*, 37 (4), pg. 1915-1918.

[57] Chong, J. M. and MacDonald, N.C., 1998, Suspended Moving Channels and Channel Actuators for Microfluidic Applications, *American Society of Mechanical Engineers, Dynamic Systems and Control Division*, 66, *Micro-Electro-Mechanical Systems (MEMS)*, pp.433-438.

[58] Bergamasco, M., Dario, P. and Salsedo, F., 1990, Shape Memory Alloy Microactuators, *Sensors and Actuators, A: Physical,* 21 (1-3), pp.253-257.

[59] Krulevitch, P., *et al.*, 1996, Thin Film Shape Memory Alloy Microactuators, *Journal of Microelectromechanical Systems*, 5 (4), pg. 270-282.

[60] M. A. Northrup, M. T. Ching, R. M. White, and R. T. Watson, DNA Amplification with A Microfabricated Reaction Chamber, in *Proc. 1993 IEEE Int. Conf. Solid-State Sens. Actuators,* pp.924–926, 1993.

[61] M. A. Bucaro, J. M. Calvert, A. S. Rudolph, B. Spargo, and R. Kapur, Photolithography as A Tool to Fabricate Polymeric Flow Chambers for I*n-vitro C*ellular Applications," in *Proc. IEEE South. Biomed. Eng. Conf.,* 1997, pp. 217–219.

[62] M. D. O'Neill, Sequencers Benefit from Solid-state Detectors, *Laser Focus World,* vol. 10, pp. 135–142, 1995.

[63] J. B. Lamture, K. L. Beattie, *et al.*, Direct Detection of Nucleic Acid Hybridization on the Surface of A Charge Coupled Device, *Nucl. Acids Res.,* vol. 22, pp. 2121–2125, 1994.

[64] S. N. Brahmasandra, B. N. Johnson, *et al.*, On-chip DNA Band Detection in Microfabricated Separation Systems, in *Proc. 1998 SPIE Microfluidic Devices,* Santa Clara, CA, *Proc. SPIE*, Vol. 3515, p. 242-251.

[65] Jin-Woo Choi, Puntambekar, A., *et al.*, A Disposable Plastic Biochip Cartridge with On-chip Power Sources for Blood Analysis, *IEEE The Sixteenth Annual International Conference on Micro Electro Mechanical Systems, MEMS-03 Kyoto,* 19-23 Jan. 2003 Page(s):447 – 450.

[66] Thomas Cubaud, Mahidhar Tatineni, Xiaolin Zhong, and Chih-Ming Ho, Bubble Dispenser in Microfluidic Devices, *Phys. Rev. E,* Vol. 72, 037302 , 2005.

[67] Yamada M, Seki M., Nanoliter-sized Liquid Dispenser Array for Multiple Biochemical Analysis in Microfluidic Devices, *Anal Chem.* 2004, Feb 15, 76(4), pp.895-9.

[68] D. J. Beebe, G. A. Mensing, and G. M. Walker, Physics and Applications of Microfluidics in Biology, *Annu. Rev. Biomed. Eng.* 2002, vol. 4, pp.261-86.

[69] Shoffner M, Cheng J, Hvichia G, Kricka L, Wilding P., Chip PCR. I. Surface Passivation of Microfabricated Silicon-glass Chips for PCR. *Nucleic Acids Res.*, 1996, 24, pp.375–79.

[70] Cheng J, Shoffner M, Hvichia G, Kricka L, Wilding P., Chip PCR. II. Investigation of Different PCR Amplification Systems in Microfabricated Silicon-glass Chips., *Nucleic Acids Res.*, 1996 24, pp.380–85.

[71]   Taylor T, Winn-Deen E, Picozza E, Woudenberg T, Albin M. 1997. Optimization of The Performance of The Polymerase Chain Reaction in Silicon-based Micro-structures, *Nucleic Acids Res.,* 1997, 25, pp.3164–68.

[72]   Kopp M, de Mello A, Manz A., Chemical Amplification: Continuous-flow PCR on A Chip, *Science,* 1998, 280, pp.1046–48.

[73]   Giordano B, Ferrance J, Swedberg S, Huhmer A, Landers J., 2001. Polymerase Chain Reaction in Polymeric Microchips: DNA Amplification in Less Than 240 seconds, *Anal. Biochem.*, 291, pp.124–32.

[74]   Wilding P., Kricka L., Cheng J., Hvichia G., Shoffner M., Fortina P., 1998. Integrated Cell Isolation and Polymerase Chain Reaction Analysis Using Silicon Microfilter Chambers, *Anal. Biochem.,* 257, pp.95–100.

[75]   Hong J., Fujii T., Seki M., Yamamoto T., Endo I. 2000., PDMS (polydimethylsiloxane)-glass Hybrid Microchip for Gene Amplification, *Annu. IEEE EMBS Conf. Microtechnology Med. Biol.*, *1st*, Lyon, Fr., pp. 407–10.

[76]   Jacobson S, Ramsey J., 1996, Integrated Microdevice for DNA Restriction Fragment Analysis, *Anal. Chem.* 68, pp.720–23.

[77]   Yuen P, Kricka L, Fortina P, Panaro N, Sakazume T, Wilding P., 2001, Microchip Module for Blood Sample Preparation and Nucleic Acid Amplification Reactions, *Genome Res.,* 11, pp.405–12.

[78]   Waters L, Jacobson S, Kroutchinina N, Khandurina J, Foote R, Ramsey J., 1998, Microchip Device for Cell Lysis, Multiplex PCR, Amplification, and Electrophoretic Sizing, *Anal. Chem.*, 70, pp.158–62.

[79]   Woolley A., Hadley D., Landre P., de Mello A., Mathies R., Northrup M., 1996, Functional Integration of PCR Amplification and Capillary Electrophoresis in A Microfabricated DNA Analysis Device, *Anal. Chem.*, 68, pp. 4081–86.

[80]   Anderson R, Su X, Bogdan G, Fenton J., 2000, A Miniature Integrated Device for Automated Multistep Genetic Assays, *Nucleic Acids Res.*, 28, e60:i–vi.

[81]   Meldrum D., 2000, Automation for Genomics, Part Two: Sequencers, Microarrays, and Future Trends, *Genome Res.*, 10, pp.1288–303.

[82]   Burke D, Burns M, Mastrangelo C., 1997, Microfabrication Technologies for Integrated Nucleic Acid Analysis, *Genome Res.*, 7, pp.189–97.

[83]   Krishnan M, Namasivayam V, Lin R, Pal R, Burns M., 2001, Microfabricated Reaction and Separation Systems, *Curr. Opin. Biotechnol.*, 12, pp.92–98.

[84]   Ehrlich D, Matsudaira P., 1999, Microfluidic Devices for DNA Analysis, *Trends Biotechnol,.* 17, pp. 315–19.

[85]   Sanders G, Manz A. 2000. Chip-based Microsystems for Genomic and Proteomic Analysis, *Trends Anal. Chem.*, 19, pp.364–78.

[86]   Moser I, Jobst G, Svasek P, Varahram M, Urban G., 1997, Rapid Liver Enzyme Assay with Miniaturized Liquid Handling System Comprising Thin Film Biosensor Array, *Sens. Actuators B,* 44, pp.377–80.

[87]   Hadd A, Raymond D, Halliwell J, Jacobson S, Ramsey J. 1997. Microchip Device for Performing Enzyme Assays, *Anal. Chem.,* 69, pp.3407–12.

[88]   Cohen CB, Chin-Dixon E, Jeong S, Nikiforov T., 1999, A Microchip-based Enzyme Assay for Protein Kinase A., *Anal. Biochem.,* 273, pp.89–97.

[89]   Hadd A, Jacobson S, Ramsey J., 1999, Microfluidic Assays of Acetylcholinesterase Inhibitors, *Anal. Chem.,* 71, pp.5206–12.

[90]   Duffy D, Gillis H, Lin J, Sheppard N, Kellogg G., 1999, Microfabricated Centrifugal Microfluidic Systems: Characterization and Multiple Enzymatic Assays, *Anal. Chem.,* 71, pp.4669–78.

[91]   Schilling E, Kamholz A, Yager P. 2001, Cell Lysis and Protein Extraction in A Microfluidic Device with Detection by A Fluorogenic Enzyme Assay, In *Micro Total Analysis Systems*, 2001, edited by Ramsey J, van den Berg A., Boston, Kluwer Acad., pp.265–67.

[92]   Sever J., Application of A Microtechnique to Viral Serological Investigations, *J. Immunol.,* 1962*,* 88, pp.320–29.

[93]   Koutny L, Schmalzing D, Taylor T, Fuchs M., 1996, Microchip Electrophoretic Immunoassay for Serum Cortisol., *Anal. Chem.,* 1996*,* 68, pp.18–22.

[94]   Heeren F, Verpoorte E, Manz A, Thormann W. 1996, Micellar Electrokinetic Chromatography Separations and Analyses of Biological Samples on A Cyclic Planar Microstructure, *Anal. Chem.,* 68, pp.2044–53.

[95]   Chiem N, Harrison D., 1997, Microchipbased Capillary Electrophoresis for Immunoassays: Analysis of Monoclonal Antibodies and Theophylline, *Anal. Chem.,* 69, pp.373–78.

[96]   Schmalzing D, Koutny L, Taylor T, NashabehW, Fuchs M., 1997, Immunoassay for Thyroxine (T4) in Serum Using Capillary Electrophoresis and Micromachined Devices., *J. Chromatogr. B,* 697, pp.175–80.

[97]   Bernard A, Michel B, Delamarche E., 2001, Micromosaic Immunoassays, A*nal. Chem.* 73, pp.8–12.

[98]   Yang T, Jung S, Mao H, Cremer P., 2001, Fabrication of Phospholipid Bilayercoated Microchannels for On-chip Immunoassays, *Anal. Chem.,* 73, pp.165–69.

[99]   Eteshola E, Leckband D. 2001. Development and Characterization of An ELISA Assay in PDMS Microfluidic Channels, *Sens. Actuators B,* 72, pp.129–33.

[100]   Dodge A, Fluri K, Verpoorte E, de Rooij N., 2001, Electrokinetically Driven Microfluidic Chips with Surface-modified Chambers for Heterogeneous Immunoassays, *Anal. Chem.,* 73, pp.3400–9.

[101]   Stokes D, Griffin G,Vo-Dinh T., 2001, Detection of E. Coli Using A Microfluidics-based Antibody Biochip Detection System, *Fresenius J. Anal. Chem.* 369, pp.295–301.

[102]   Sato K, Tokeshi M, Odake T, Kimura H, Ooi T, *et al*., 2000, Integration of An Immunosorbent Assay System: Analysis of Secretory Human Immunoglobulin A on Polystyrene Beads in A microchip, *Anal. Chem.* 72, pp.1144–47.

[103]   Cheng S, Skinner C, Taylor J, Attiya S, Lee W, *et al*., 2001, Development of A Multichannel Microfluidic Analysis System Employing Affinity Capillary Electrophoresis for Immunoassay, *Anal. Chem.,* 73, pp.1472–79.

[104]   Chiem N, Harrison D., 1998, Microchip Systems for Immunoassay: An Integrated Immunoreactor with Electrophoretic Separation for Serum Theophylline Determination, *Clin. Chem.,* 44, pp.591–98.

[105]   Carlson R, Gabel C, Chan S, Austin R, Brody J,Winkelman J. 1997, Self-sorting of White Blood Cells in A Lattice, *Phys. Rev. Lett.,* 79, pp.2149–52.

[106]   Fiedler S, Shirley S, Schnelle T, Fuhr G., 1998, Dielectrophoretic Sorting of Particles and Cells in A Microsystem, *Anal. Chem.,* 70, pp.1909–15.

[107]   Li P, Harrison D., 1997, Transport, Manipulation, and Reaction of Biological Cells on-chip Using Electrokinetic Effects, *Anal. Chem.,* 69, pp.1564–68.

[108]   Sobek D, Senturia S, Gray M., 1994, Microfabricated Fused Silica Flow Chambers for Flow Cytometry, In *Tech. Dig. Solid-State Sensor Actuator Worksh., Hilton Head Island, SC*, pp. 260–63.

[109] Fu A, Spence C, Scherer A, Arnold F, Quake S., 1999, A Microfabricated Fluorescence-activated Cell Sorter, *Nat. Biotechnol.,* 17, pp.1109–11.

[110] Schrum D, Culbertson C, Jacobson S, Ramsey J., 1999, Microchip Flow Cytometry Using Electrokinetic Focusing, *Anal. Chem.,* 71, pp.4173–77.

[111] Ayliffe H, Frazier A, Rabbitt R. 1999, Electric Impedance Spectroscopy Using Microchannels with Integrated Metal Electrodes, *J. Microelectromech. Syst.,* 8, pp.50–57.

[112] Sohn L, Saleh O, Facer G, Beavis A, Allan R, Notterman D., 2000, Capacitance Cytometry: Measuring Biological Cells One by One, *Proc. Natl. Acad. Sci., USA,* 97, pp.10687–90.

[113] Facer G, Notterman D, Sohn L. 2001, Dielectric Spectroscopy for Bioanalysis: from 40 Hz to 26.5 GHz in A Microfabricated Wave Guide. *Appl. Phys. Lett. ,* 78, pp.996–98.

[114] Beebe D., 2000, Microfabricated Fluidic Devices for Single Cell Handling and Analysis, In *Emerging Tools for Single Cell Analysis: Advances in Optical Measurement Technologies*, ed. G Durack, J. Robinson, New York, Wiley.

[115] Sundberg S. 2000, High-throughput and Ultra-high-throughput Screening: Solution- and Cell-based Approaches, *Curr. Opin. Biotechnol.,* 11, pp.47–53.

[116] Pancrazio J, Whelan J, Borkholder D, Ma W, Stenger D., 1999, Development and Application of Cell-based Biosensors, *Ann. Biomed. Eng.,* 27, pp.697–711.

[117] Bousse L., 1996, Whole Cell Biosensors, *Sens. Actuators B,* 34, pp.270–75.

[118] Vo-Dinh T, Cullum B, Stokes D., 2001, Nanosensors and Biochips: Frontiers in Biomolecular Diagnostics, *Sens. Actuators B,* 74, pp.2–11.

[119] DeBusschere B, Kovacs G., 2001, Portable Cell-based Biosensor System Using Integrated CMOS Cell-cartridges, *Biosens. Bioelectron.,* 16, pp.543–56.

[120] Folch A, Toner M., 2000, Microengineering of Cellular Interactions, *Annu. Rev. Biomed. Eng.,* 2, pp.227–56.

[121] Takayama S, Ostuni E., LeDue P., Naruse K, Ingber D, Whitesides G., 2001, Laminar Flows: Subcellular Positioning of Small Molecules, *Nature,* 411, pp.1016.

[122] Inoue I, Wakamoto Y, Moriguchi H, Okano K, Yasuda K., 2001, On-chip Culture System for Observation of Isolated Individual Cells, *Lab Chip,* 1, pp.50–55.

[123] Raty S, Davis JA, Beebe DJ, Rodriguez-Zas SL, Wheeler M. B, 2001, Culture in Microchannels Enhances in Vitro Embryonic Development of Preimplantation Mouse Embryos, *Theriogenology,* 55, pp.241.

[124] Walker G, Ozers M, Beebe D., Insect Cell Culture in Microfluidic Channels, *Biomed. Microdev.,* Volume 4, Number 3, July, 2002, pp161-166.

[125] Johnson RD, Badr IHA, Barrett G, Lai S, Lu Y, *et al*., 2001, Development of A Fully Integrated Analysis System for Ions Based on Ion-selective Optodes and Centrifugal Microfluidics, *Anal. Chem.,* 73, pp.3940–46.

[126] Ahn, C. H., and Allen, M. G., 1995, Fluid Micropumps Based on Rotary Magnetic Actuators, *IEEE 8th Int. Workshop on MEMS (MEMS'95)*, pp. 408–412.

[127] Doepper, J., Clemens, M., *et al*., 1997, Micro Gear Pumps for Dosing of Viscous Fluids, *J. Micromech. Microeng*., 7, pp. 230–232.

[128] van den Pol, F. C. M., van Lintel, *et al*., 1990, A Thermopneumatic Micropump Based on Micro-Engineering Techniques, *Sens. Actuators A*, 21–23, pp. 198–202.

[129] Lammerink, T. S. J., Elwenspoek, M., and Fluitman, J. H. J., 1993, Integrated

Micro-Liquid Dosing System, *IEEE 6th Int. Workshop on MEM-MEMS'93*, pp. 254–259.

[130] Folta, J. A., Raley, N. F., and Hee, E. W., 1992, Design Fabrication and Testing of a Miniature Peristaltic Membrane Pump,'' *Tech. Dig. Solid-State Sensor and Actuator Workshop*, Hilton Head, pp. 186–189.

[131] Stemme, E., and Stemme, G., 1993, A Valveless Diffuser/Nozzle-Based Fluid Pump, *Sens. Actuators A*, 39, pp. 159–167.

[132] Moroney, R. M., White, R. M., and Howe, R. T., Ultrasonically Induced Microtransport, *IEEE 4th Int. Workshop on MEMS (MEMS'91)*, 1991, pp. 277–282.

[133] Miyazaki, S., Kawai, T., and Araragi, M., 1991, A Piezoelectric Pump Driven by A Flexural Progressive Wave, *IEEE 4th Int. Workshop on MEMS (MEMS'91)*, 1991, pp. 283–288.

[134] Kurosawa, M., Watanabe, T., and Higuchi, T., Surface Acoustic Wave Atomizer with Pumping Effect, *IEEE 8th Int. Workshop on MEMS (MEMS'95)*, 1995, pp. 25–30.

[135] Sammarco TS, Burns MA., 1999, Thermocapillary Pumping of Discrete Drops in Microfabricated Analysis Devices, *AIChE J.* 45, pp.350–66.

[136] Nam-Trung Nguyen, Wai Wah Pang *and* Xiaoyang Huang, Sample Transport with Thermocapillary Force for Microfluidics, *J. Phys.: Conf. Ser.,* 34, 2006, pp. 967-972.

[137] P S Glockner and G F Naterer, Thermocapillary Control of Microfluidic Transport with A Stationary Cyclic Heat Source, *J. Micromech. Microeng.,* 15, No. 12, December 2005, pp.2216-2229.

[138] Kataoka DE, Troian SM. 1999, Patterning Liquid Flow on The Microscopic Scale, *Nature,* 402, pp.794–97.

[139] Pollack MG, Fair RB, Shenderov AD., 2000, Electrowetting-based Actuation of Liquid Droplets for Microfluidic Applications, *Appl. Phys. Lett.,* 77, pp.1725–26.

[140] Prins M.W.J., Welters WJJ, Weekamp J.W., 2001, Fluid Control in Multichannel Structures by Electrocapillary Pressure, *Science,* 291, pp.277–80.

[141] Matsumoto, H., and Colgate, J. E., 1990, Preliminary Investigation of Micropumping Based on Electrical Control of Interfacial Tension, *IEEE 3rd Int. Workshop on MEMS (MEMS'90)*, pp. 105–110.

[142] Lee, J., and Kim, C. J., 1998, Liquid Micromotor Driven by Continuous Electrowetting, *IEEE 11th Int. Workshop on MEMS (MEMS'98)*, pp. 538–543.

[143] Gallardo BS, Gupta VK, Eagerton FD, Jong LI, Craig VS, *et al.*, 1999, Electrochemical Principles for Active Control of Liquids on Submillimeter Scales. *Science,* 283, pp.57–60.

[144] Boehm, S., Olthuis, W., and Bergveld, P., 2000, A Bi-Directional Electrochemically Driven Micro Liquid Dosing System With Integrated Sensor/ Actuator Electrodes, *IEEE 13th Int. Workshop on MEMS (MEMS'00)*, pp.92–95.

[145] Pei Yu Chiou, Hyejin Moon, *et al.*, Light Actuation of Liquid by Optoelectrowetting, *Sensors and Actuators A,* 104, 2003, pp.222–228.

[146] Yao S. H. and Santiago J. G., 2003, Porous Glass Electroosmotic Pumps: Theory, *J. Colloid Interface Sci.,* 268, pp.133–42.

[147] Yao S H, Hertzog D E, Zeng S L, Mikkelsen J. C. and Santiago J. G., 2003, Porous Glass Electroosmotic Pumps: Design and Experiments, *J. Colloid Interface Sci.,* 268, pp.143–53.

[148] Zeng S L, Chen C H, Mikkelsen J C and Santiago J. G., 2001, Fabrication and Characterization of Electroosmotic Micropumps, *Sensors Actuators* B, 79, pp.107–14.

[149] Laser D J, Goodson K E, Santiago J G and Kenny T. W., 2002, High-Frequency Actuation with Silicon Electroosmotic Micropumps, *Proc. 2002 Solid-State Sensor, Actuator, and Microsystems Workshop (Hilton Head Island, SC).*

[150] T. B. Jones, M. Gunji, M. Washizu and M. J. Feldman, Dielectrophoretic Liquid Actuation and Nanodroplet Formation, *J. Appl. Phys.*, 2001, 89, pp.1441.

[151] P. J. Burke, Nano-dielectrophoresis: Electronic Nanotweezers, *Encyclopedia of Nanoscience and Nanotechnology*, American Scientific Publishers, 2003.

[152] Vykoukal, J. Schwartz, F. Becker and P. Gascoyne, A Programmable Dielectrophoretic Fluid Processor for Droplet-based Chemistry, *Micro Total Analysis Systems 2001*, Kluwer Academic Publishers, 2001, pp.72.

[153] Bart, S. F., Tavrow, L. S., Mehregany, M., and Lang, J. H., 1990, Microfabricated Electrohydrodynamic Pumps, *Sens. Actuators A*, 21–23, pp. 193–197.

[154] Fuhr, G., Hagedom, R., Mueller, T., Benecke, W., and Wagner, B., 1992, Pumping of Water Solutions in Microfabricated Electrohydrodynamic Systems, *IEEE 5th Int. Workshop on MEMS (MEMS'92)*, pp. 25–30.

[155] Ahn, S. H., and Kim, Y. K., 1998, Fabrication and Experiment of A Planar Micro Ion Drag Pump, *Sens. Actuators A*, 70, pp. 1–5.

[156] Richter, A., and Sandmaier, H., 1990, An Electrohydrodynamic Micropump, *IEEE 3rd Int. Workshop on MEMS (MEMS'90)*, pp. 99–104.

[157] Richter, A., Plettner, A., Hofmann, K. A., and Sandmaier, H., 1991, A Micromachined Electrohydrodynamic (EHD) Pump, *Sens. Actuators A*, 29, pp.159–168.

[158] Jang J. S. and Lee S. S., 2000, Theoretical and Experimental Study of MHD (Magnetohydrodynamic) Micropump, *Sensors Actuators* A, 80**,** pp.84–9.

[159] Lemoff A. V. and Lee A. P., 2000, An AC Magnetohydrodynamic Micropump *Sensors Actuators* B, 63, pp.178–85.

[160] Huang L, Wang W, Murphy M C, Lian K. and Ling Z. G., 2000, LIGA Fabrication and Test of A DC Type Magnetohydrodynamic (MHD) Micropump, *Microsyst. Technol.,* 6, pp.235–40.

[161] Zhong J. H., Yi M. Q. and Bau H. H., 2002, Magnetohydrodynamic (MHD) Pump Fabricated with Ceramic Tapes, *Sensors Actuators* A, 96**,** pp.59–66.

[162] Steven Vogel, Life in Moving Fluids: The Physical Biology of Flow, 2nd edition, Princeton, N.J, Princeton University Press, 1994.

[163] W. S. N. Trimmer , Microrobots and Micromechanical Systems, *Sensors and Actuators*, Volume 19, Number 3, September 1989, pages 267 - 287

[164] S. Semal, C. Bauthier, *et al.*, Spontaneous Spreading of Liquid Droplets on Mixed Alkanethiol Monolayer: Dynamics of Wetting and Wetting Transition, *J. Phys. Chem. B*, 2000, 104, pp.6225-6232.

[165] J. H. Lee, K. S. Hwang, *et al*., Microstructure and Adhesion of Au Deposited on Parylene-c Substrate with Surface Modification for Potential Immunoassay Application, *IEEE Transactions on Plasma Science*, Volume 32, Issue 2, Part 1, April 2004, Page(s):505 – 509.

[166] Jun Zhang, W. X. Zhou, *et al.*, Argon Plasma Modification of SU-8 for Very High Aspect Ratio and Dense Copper Electroforming, *J. Electrochem. Soc.*, Volume 152, Issue 10, 2005, pp. C716-C721.

[167] http://www.agc.co.jp/english/chemicals/shinsei/cytop/cytop.htm.

[168] Thomas Young, An Essay on The Cohesion of Fluids, *Philosophical Transactions of The Royal Society of London*, Vol.95, 1805, pp.65-87.

[169] N. K. Adam, The Physics And Chemistry of Surfaces, Oxford University Press, London, 3rd ed., 1944.

[170] R. Craig, L. A. Nicholas, Active Control of Interfacial Properties, *Current Opinion in Colloid & Interface Science*, vol. 5, 2000, pp.81-87.

[171] K. Ichimura, S. K. Oh, M. Nakagawa, Light-Driven Motion of Liquids on A Photoresponsive Surface, *Science*, Vol. 288, 2000, pp.1624-1626.

[172] T. S. Sammarco and M. A. Burns, Heat-transfer Analysis of Microfabricated Thermocapillary Pumping and Reaction Devices, *J. Micromech. Microeng.*, Vol. 10, pp.42-45, 2000.

[173] Lippmann G., Relations entre les ph´enom`enes ´electriques et capillaries, *Ann. Chim. Phys.,* 1875, 5, pp.494.

[174] P. Gravesen, Jens Branebjerg, and Ole S∅ndergård Jensen, Microfluidics-A Review, *Journal of Micromechanics and Microengineering*, Vol 3, pp.168-182, 1993.

[175] M. A. Huff, M. S. Mettner, *et al.*, A Pressure-balanced Electrostatically-actuated Microvalve, *Solid-State Sensor and Actuator Workshop, 1990, 4th Technical Digest, IEEE*, 4-7 June 1990, Page(s):123 – 127.

[176] T. M. Squires and S. R. Quake, Microfluidics: Fluid Physics at The Nanoliter Scale, *Reviews of Modern Physics*, Vol. 77, July 2005, pp.977-1026.

[177] R. Zengerle and H. Sandmaier, Microfluidics, *Micro Machine and Human Science, 1996, Proceedings of the Seventh International Symposium*, 2-4 Oct. 1996, pp.13-20.

[178] N. T. Nguyen, X. Y. Huang and T. K. Chuan, MEMS--micropumps: A Review, *ASME Journal of Fluids Engineering*, Vol. 124, No. 2, pp 384 – 392, 2002.

[179] D. J. Laser and J. G. Santiago, A Review of Micropiumps, *Journal of Micromechanics and Microengineering*, Vol. 14, 2004, R35-R64.

[180] Nam-Trung Nguyen, Steven T. Wereley, Fundamentals and Applications of Microfluidics, *Artech House, Inc*., 2002.

[181] Richter A., Hofmann K.A., Plettner A., and Sandmaier H., The Electrohydrodynamic Micro Flow Meter, *Technical Digest IEEE Transducers'91*, San Francisco, CA, 1991, pp. 935-938.

[182] Richter A., Sandmaier H. and Plettner A., An Electrohydrodynamic Injection Pump—A Novel Actuator For Microsystem Technology, *Proceedings of Micro System Technologies 90*, Berlin 1990, pp.812-817.

[183] Furuya, A., *et al.*, Fabrication of Fluorinated Polyimide Microgrids Using Magnetically Controlled Reactive Ion Etching (MC-RIE) and Their Applications to An Ion Drag Integrated Micropump, *Journal of Micromechanics and Microengineering*, Vol. 6, 1996, pp.310-319.

[184] R. F. Probstein, Physicochemical Hydrodynamics: An Introduction, 2nd ed., New York: John Wiley & Sons, 1994.

[185] Liu S., and Dasgupta P. K., Flow-injection Analysis in The Capillary Format Using Electroosmotic Pumping, *Anal. Chim.Acta,* 268, 1992, pp.1–6.

[186] Manz A *et al.,* 1994, Electroosmotic Pumping and Electrophoretic Separations for Miniaturized Chemical-analysis Systems, *J. Micromech. Microeng.* 4, pp.257–65.

[187] Harrison D. J., *et al.,* 1993, Micromachining A Miniaturized Capillary Electrophoresis-based Chemical Analysis System on A Chip, *Science,* 261, pp.895–7.

[188] Jacobson S. C., Hergenroder R, Koutny L. B. and Ramsey J. M., 1994, Open-channel Electrochromatography on A Microchip, *Anal. Chem.,* 66, pp.2369–73.

[189] G. Beni and S. Hackwood, Electrto-wetting Displays, *Appl. Phys. Lett.*, Vol. 38 (4), pp.207-209, 1981.

[190] G. Beni and M. A. Tenan, Dynamics of Electrowetting Displays. *J. Appl. Phys.,* Vol. 52 (10), pp.6011-6015, 1981.

[191] G. Beni, S. Hackwood, and J. L. Jackel, Continuous Electrowetting Effect, *Appl. Phys. Lett.*, vol. 40, 1982, pp.912-914.

[192] J. L. Jackel, S. Hackwood and G. Beni, Electrowetting Optical Switch, *Appl. Phys. Lett.*, vol. 40, 1982, pp.4-5.

[193] J. L. Jackel, S. Hackwood, J. J. Veselka and G. Beni, Electrowetting Switch for Multimode Optical Fibers, Applied optics, Vol. 22, 1983, pp.1765-1770.

[194] J. Lee and C. J. Kim, Surface-tension-driven Microactuation Based on Continuous Electrowetting, *Journal of MEMS*, Vol. 9, 2000, pp.171-180.

[195] K. S. Yun, I. J. Cho, J. U. Bu, C. J. Kim and E. Yoon, A Surface-tension Driven Micropump for Low-voltage and Low-power Operations, *J. MEMS*, Vol. 11, 2002, pp.454-461.

[196] Berge B., 1993, Electrocapillarite et mouillage de films isolants par l'eau, *C. R. Acad. Sci.* II, vol. 317, pp.157-163.

[197] M. Vallet, B. Berge and L. Vovelle, Electrowetting of Water and Aqueous Solutions on Poly(ethylene terephthalate) Insulating Films, *Polymer*, Vol. 37(12), 1996, pp.2465-2470.

[198] V. Peykov, A. Quinn and J. Ralson, Electrowetting: A Model for Contact-angle Saturation, *Colloid Polym. Sci.*, Vol. 278, 2000, pp.157-163.

[199] H. J. J. Verheijen and M. W. J. Prins, Reversible Electrowetting and Trapping of Charge: Model and Experiments, *Langmuir*, Vol. 15, 1999, pp.6616-6620.

[200] T. D. Blake, A. Clarke, and E. H. Stattersfield, An Investigation of Electrostatic Assist in Dynamic Wetting , *Langmuir*, Vol.16, 2000, pp.2928-2935.

[201] M. Schneemilch, W. J. J. Welters, et al., Electrically Induced Changes in Dynamic Wettability, *Langmuir*, Vol. 16, 2000, pp.2924-2927.

[202] C. Quilliet, B. Berge, Investigation of Effective Interface Potential by Electrowetting, *Europhysics Letters*, Vol. 60 (1), 2002, pp.99-105.

[203] K. H. Kang, How Electrostatic Fields Change Contact Angle in Electrowetting, *Langmuir*, 2002, Vol 18, pp.10318-10322.

[204] A. Quinn, R. Sedev, and J. Ralston, Influence of The Electrical Layer In Electrowetting, *J. Phys. Chem. B*., 2003, Vol.17 pp.1163-1169.

[205] J. S. Kuo, P. S. Mihalic, *et al.*, Electrowetting-induced Droplet Movement in An Immiscible Medium, *Langmuir*, 2003, Vol. 19, pp.250-255.

[206] B. Janocha, H. Bauser, *et al.*, Competitive Electrowetting of Polymer Surfaces by Water and Decane, Langmuir, 2000, Vol.16, pp.3349-3354.

[207] C. Quilliet, B. Berge, Electrowetting: A Recent Outbreak, *Curr. Opin. Colloi. Interf. Sci.*, Vol.6 2001, pp.34-39.

[208] A. A. Darhuber and S. M. Troian, Principles of Microfluidic Actuation by Modulation of Surface Stresses, *Annu. Rev. Fluid Mech.*, 2005, Vol. 37, pp.425-455.

[209] F. Mugele and J. C. Barget, Electrowetting: From Basic To Applications, *J. Phys.: Condens. Matter*, 2005, Vol. 17, R705-R774.

[210] Sondag-Huethorst, J. A. M.; Fokkink, L. G. J., Electrical Double Layers on Thiol-modified Polycrystalline Gold Electrodes", *J. Electroanal. Chem.* 1994, Vol.*367*, pp.49-57.

[211] Sondag-Huethorst, J. A. M., Fokkink, L. G. J., P, Potential-dependent Wetting of Electroactive Ferrocene-terminated Alkanethiolate Monolayers on Gold, *Langmuir,* 1994, Vol.10, 4380-4387.

[212] W. J. J. Welters and L. G. J. Fokkink, Fast Electrically Switchable Capillary Effects, *Langmuir*, Vol. 14, 1998, pp.1535-1538.

[213] M.G. Pollack, A.D. Shenderov, and R. B. Fair, Electrowetting-based Actuation of Droplets for Integrated Microfluidics, *Lab Chip*, Vol. 2, 2002, pp.96-101.

[214] Belaubre P, Guirardel M, *et al.*, 2004, Cantilever-based Microsystem for Contact and Non-contact Deposition of Picoliter Biological Samples, *Sensors Actuators* A, Vol. 110, pp.130-135.

[215] Hoshino K, Triteyaprasert S, Matsumoto K and Shimoyama I., 2004, Electrowetting-based Pico-liter Liquid Actuation in A Glass-tube Microinjector, *Sensors Actuators* A, Vol. 114**,** pp.473-477.

[216] Yi U. C. and Kim C. J., 2004, Soft Printing of Droplets Pre-metered by Electrowetting, *Sensors Actuators* A, Vol.114, pp.347-354.

[217] Cheng J. Y. and Hsiung L. C., 2004, Electrowetting (EW)-based Valve Combined with Hydrophilic Teflon Microfluidic Guidance in Controlling Continuous Fluid Flow, *Biomed. Microdev.* Vol. 6, pp.341.

[218] M. Vallet, M. Vallade and B. Berge, Limiting Phenomena for The Spreading of Water on Polymer Films by Electrowetting, *Eur. Phys. J. B*, Vol. 11, 1999, pp.583-591.

[219] B. Shapiro B., Moon H., *et al.*, Equilibrium Behavior of Sessile Drops Under Surface Tension, Applied External Fields, And Material Variations, *J. Appl. Phys.*, Vol. 93, No.9, 2003, pp.5794-5811.

[220] Jones T. B, Fowler J. D., Chang Y. S. and Kim C. J., 2003, Frequency-based Relationship of Electrowetting and Dielectrophoretic Liquid Microactuation, *Langmuir,* Vol.19**,** pp.7646-7651.

[221] Han G., and Albert V. D. B., Micro- and Nanofluidic Devices for Environmental and Biomedical Applications, *Intern. J. Environ. Anal. Chem.*, Vol. 84, No. 11, pp.809-819, Sep. 15, 2004.

[222] Jong W. H., and Stephen R. Q., Integrated Nanoliter Systems, *Nature Biotechnology*, Volume 21, No. 10, October 2003.

[223] T. B. Jones and K. L. Wang, Frequency-Dependent Electromechanics of Aqueous Liquids: Electrowetting and Dielectrophoresis, *Langmuir*, Vol. 20, 2004, pp.2813-2818.

[224] F. Mugele, A. Klingner, *et al.*, Electrowetting: A Convenient Way To Switchable Wettability Patterns, *J. Phys. :Condens. Matter*, Vol.17, 2005, pp.S559-S576.

[225] F. Mugele and S. Herminghaus, Electrostatic Stabilization of Fluid Microstructures, *Appl. Phys. Lett.*, Vol. 81, 2002, pp.2303-2305.

[226] A. Klingner, J. Buehrle and F. Mugele, Capillary Bridges in Electric Fields, *Langmuir*, Vol.20, 2004, pp.6770-6777.

[227] M. Vallet, M. Vallade and B. Berge, Limiting Phenomena for The Spreading of Water on Polymer Films by Electrowetting, *Eur. Phys. J. B*, Vol. 11, 1999, pp.583-591.

[228] T. N. Krupenkin, J. A. Taylor, *et al.*, From Rolling Ball To Complete Wetting: The Dynamic Tuning of Liquids on Nanostructured Surfaces, *Langmuir*, Vol. 20, 2004, pp.3824-3827.

[229] J. Y. Yoon and R. L. Garrell, Preventing Biomolecular Adsorption in Electrowetting-Based Biofluidic Chips, *Anal. Chem.*, 2003, Vol. 75, pp.5097-5102.

[230] Aaron R. Wheeler, H. J. Moon, *et al.*, Electrowetting-Based Microfluidics for Analysis of Peptides and Proteins by Matrix-Assisted Laser Desorption/ Ionization Mass Spectrometry, *Anal. Chem.*, 2004, Vol. 76, pp.4833-4838.

[231] V. Srinivasan, V. K. Pamula, R. B. Fair, Droplet-based Microfluidic Lab-on-a-chip for Glucose Detection, *Anal. Chim. Acta*, Vol. 507, 2004, pp.145-150.

[232] S. K. Cho, H. Moon and C. J. Kim, Creating, Transporting, Cutting and Merging Liquid Droplets by Electrowetting-based Actuation for Digital Microfluidic Circuits, *J. MEMS*, Vol. 12, No. 1, 2003, pp.70-80.

[233] F. Saeki, J. Baum, et al., Electrowetting on Dielectrics (EWOD): Reducing Voltage Requirements for Microfluidics, *American Chemical Society National Meeting, Chicago, II*, August 2001.

[234] H. J. Moon, S. K. Cho, et al., Low Voltage Electrowetting-on-dielectric, *J. Appl. Phys.*, Vol. 92, No. 7, 2002, pp.4080-4087.

[235] K. L. Wang and T. B. Jones, Frequency-dependent Bifurcation in Electromechanical Microfluidic Structures, *J. Micromech. Microeng.*, Vol. 14, 2004, pp.761-768.

[236] V. Srinivasan, V. K. Pamula and R. B. Fair, An Integrated Digital Microfluidic Lab-on-a-chip for Clinical Diagnostic on Human Physiological Fluids, *Lab Chip*, 2004, Vol. 4, pp.310-315.

[237] W. J. J. Welters and L. G. J. Fokkink, Fast Electrically Switchable Capillary Effects, *Langmuir*, Vol. 14, 1998, pp.1535-1538.

[238] M. Bienia, C. Quilliet and M. Vallade, Modification of Drop Shape Controlled by Electrowetting, *Langmuir*, 2003, Vol. 19, pp.9328-9333.

[239] P. Mach, T. Krupenkin, *et al.*, Dynamic Tuning of Optical Waveguides with Electrowetting Pumps and Recirculating Fluid Channels, *Appl. Phys. Lett.*, Vol.81, 2002, pp.202-204.

[240] T. Krupenkin, S. Yang, and P. Mach, Tunable Liquid Microlens, *Appl. Phys. Lett.*, Vol. 82, 2003, pp. 316-318.

[241] U. C. Yi and C. J. Kim, Soft Printing of Droplets Digitized by Electrowetting, *12th International Conference on Transducers, Solid-State Sensors, Actuators and Microsystems*, Volume 2, 8-12 June 2003, Page(s):1804 – 1807.

[242] U. C. Yi, and C. J. Kim, Characterization of Electrowetting Actuation on Addressable Single-side Coplanar Electrodes, *J. Micromech. Microeng.*, Vol. 16, 2006, pp.2053-2059.

[243] B. R. Acharya, T. Krupenkin, *et al.*, Tunable Optical Fiber Devices Based on Broadband Long-period Gratings and Pumped Microfluidics, *Appl. Phys. Lett.*, Vol. 83, No. 24, 2003, pp.4912-4914.

[244] D. Huh, A. H. Tkaczyk, *et al.*, Reversible Switching of High-speed Air-liquid Two-phase Flows Using Electrowetting-assisted Flow Pattern Change, *J. AM. Chem. Soc.*, Vol. 125, 2003, pp.14678-14679.

[245] M. Bienia, F. Mugele, *et al.*, Droplets Profiles And Wetting Transition in Electric Fields, *Physica A*, Vol. 339, 2004, pp.72-79.

[246] H. Klauk, J. R. Huang, *et al.*, Ion-beam-deposited Ultrathin Transparent Metal Contacts, *Thin Solid Films*, 2000, Vol.366, pp.272-278.

[247] Hari Sinh Nalwa, ed., Handbook of Low and High Dielectric Constant Materials and Their Applications, San Diego, Calif., London, Academic, 1999.

[248] S. Yang, T. N. Krupenkin, et al., Tunable and Latchable Liquid Microlens with Photopolymerization Components, *Advanced Materials*, 2003, Vol. 15, No. 11, pp.940-943.

[249] Asahi Glass Co. Ltd., http://www.agc.co.jp/english/chemicals/shinsei/cytop/cytop.htm

[250] Bellex International Corp., Cytop™ Technical Information.

[251] R. R. Thomas, Wettability of Polished Silicon Oxide Surfaces, *J. Electrochem, Soc.*, Vol. 143, Nol. 1, 1996, pp.6430648.

[252] M. M. Sung, G. J. Kluth and R. Maboudian, Formation of Alkylsiloxane Self-assembled Monolayers on Si_3N_4, *A. Vac. Sci. Technol. A*, Vol. 16(2), 1999, pp.540-544.

[253] O. K. Tan, X. Y. Fang, *et al.*, Immobilization of Bovine Serum Albumin on Self-assembled Monolayer Modified Dielectric Film for Biosensor Application, *Sensors, 2005, IEEE*, 30 Oct.-3 Nov., Page(s):397-400.

[256] C. Y. Chang and S. M. Sze, editors, ULSI Technology, New York, McGraw-Hill Co. Inc., 1996.

[257] Y. Imanaka, T. Shioga and J. D. Baniecki, Decoupling Capacitor with Low Inductance for High-frequency Digital Applications, *Fujitsu Sci. Tech. J.*, Vol. 38, No. 1, 2002, pp.22-30.

[258] C. D. Bain, E. Barry, et al., Formation of Monolayer Films by The Spontaneous Assembly of Organic Thiols From Solution onto Gold, *J. Am. Chem. Soc.*, 1989, Vol. 111, pp.321-335.

[259] Y. W. Chang and D. Y. Kwok, Electrowetting on Dielectric: A Low Voltage Study on Self-Assembled Monolayers and Its Wetting Kinetics, *Proceedings of the 2004 International Conference on MEMS, NANO and Smart Systems (ICMENS'04)*.

[260] C. B. Gorman, H. A. Biebuyck and G. M. Whitesides, Control of the Shape of Liquid Lenses on A Modified Gold Surface Using An Applied Electrical Potential Across A Self-Assembled Monolayer, *Langmuir*, 1995, Vol. 11, pp.2242-2246.

[261] L. Minnema, H. A. Barneveld, and P. D. Rinkel, An Investigation in to The Mechanism of Water Treeing in Polyethylene High-voltage Cables, *IEEE Transactions on Electrical Insulation*, Vol. EI-15, 1980, pp.461-472.

[262] Dow Corning Corp., Information about Dow Corning® Brand Silicone Encapsulants.

[263] M. D. King, J. C. Yang and *et al.*, Evaporation of A Small Water Droplet Containing An Additive, *Proceedings of The ASME National Heat Transfer Conference*, Baltimore, August, 1997, pp.1-6.

[264] N. S. Bonn, S. Rafai and *et al.*, Evaporating Droplets, *Journal of Fluid Mechanics*, Vol. 549, 2006, pp.307-313.

[265] Saman Dharmatilleke and H. Liu, Systems and Methods for Pumping Continuous Liquid Columns Using Hydrophobicity Control Features in A Microchannel, 2006, International Publication No. WO2006115464 A1.

[266] Digilov, R., Charge-induced Modification of Contact Angle: The Secondary Electrocapillary Effect, Langmuir, 200, 16, pp6719-6723.

[267] T.B. Jones, On The Relationship of Dielectrophoresis and Electrowetting, Langmuir, 2002, 18, 4437-4443.

[268] J. Zeng and T. Korsmeyer, Principles of Droplet Electrohydrodynamics for Lab-on-a-chip, Lab-on-a-chip, 2004, 4 ,pp265-277.

[269] J. R. Melcher, Continuum Electromechanics, *the MIT press*, 1981, Section 3.7.

[270] Langbein D. W., Capillary Syrfaces: Shape-Stability-Dynamics, In Particular under Weighlessness, Springer, 2002, p. xviii.

[271] R. B. Bird, W. E. Stewart and E. N. Lightfoot, Transport Phenomena, New York, Wiley, 2nd ed., 2001.

[272] W. Huang, R. S. Bhullar and Y. C. Fung, The Surface-Tension-Driven Flow of Blood From a Droplet into A Capillary Tube, *Transaction of ASME*, 2001, Vo.123, pp.446-454.

[273] B. H. Jo., L. M. Van Lerberghe, K. M. Motsegood, and D. J. Beebe, Three-Dimensional Micro-Channel Fabrication in Polydimethylsiloxane (PDMS) Elastomer, *Journal of Microelectromechanical Systems*, Vol. 9, No. 1, pp.76-81, March 2000.

[274] J. C. McDonal, D. C. Duffy, J. R. Anderson, D., T. Chiu, H. Wu, O. J. A. Schueller, and G. M. Whitesides, Fabrication of Microfluidic Systems in Poly(dimethylsiloxane), *Electrophoresis*, 21, pp.27-40, 2000.

[275] S. F. Li, and S. C. Chen, Polydimethylsiloxane Fluidic Internects for Microfluidics Systems, *IEEE Transactions on Advanced Packaging*, Vol. 26, No. 3, pp.242-247, 2003.

[276] S. F. Li, P. N. Floriano, N. Christodoulides, D. Y. Fozdar, D. B. Shao, M. F. Ali, P. Dharshan, S. Mohanty, D. Neikirk, J. T. McDevitt, and S. C. Chen, Disposable Polydimethylsiloxane/Silicon Hybrid Chips for Protein Detection", *Biosensors and Bioelectronics*, Vol. 21, pp.574-584, 2005.

[277] Whitesides, G.M., Ostuni, E., Takayama, S., Jiang, X., Ingber, D.,Soft Lithography in Biology and Biochemistry, *Annu. Rev. Biomed. Eng.* 3, pp.335–373, 2001.

[278] Sia, S.K., Whitesides, G.M., Microfluidic Devices Fabricated in Poly(dimethylsiloxane) for Biological Studies. *Electrophoresis*, Vol.24, pp.3563–3576, 2003.

[279] Hosokawa, K., Maeda, R., A Pneumatically-Actuated Three-Way Microvalve Fabricated with Polydimethylsiloxane Using the Membrane Transfer Technique, *J. Micromech. Microeng.*, Vol.10, pp.415–420, 2000.

[280] Hosokawa, K., Sato, K., Ichikawa, N., Maeda, M., Power-free Poly(dimethylsiloxane) Microfluidic Devices for Gold Nano Particle Based DNA Analysis, *Lab-on-a-Chip*, Vol.4, pp.181–185, 2004.

[281] Marquette, C.A., Blum, L.J., Direct Immobilization in Poly(dimethylsiloxane) for DNA, Protein and Enzyme Fluidic Biochips, *Anal. Chim. Acta.*, 506, pp.127–132, 2004.

[282] Noerholm, M., Bruus, H., Jakobsen, M.H., Telleman, P., Ramsing, N.B., Polymer Microfluidic Chip for Online Monitoring of Microarray Hybridizations, *Lab-on-a-Chip*, Vol. 4, pp.28–37, 2004.

[283] S. Bhattacharya, A. Datta, J. M. Berg, and S. Gangopadhyay, Studies on Surface Wettability of Poly(Dimethyl) Siloxane (PDMS) and Glass Under Oxygen-Plasma Treatment and Correlation With Bond Strength, *J. MEMS*, Vol. 14, No. 3, pp.590-597, June 2005.

[284] M. J. Owen and P. J. Smith, Plasma Treatment of Poly (dimethyl) Siloxane, *J. Adhesion Sci. Technol.*, vol. 8, no. 10, pp. 1063–1075, 1994.

[285] J. Kim, M. K. Chaudhury,M. J. Owen, and T. Orbeck, The mechanisms   of hydrophobic recovery of polydimethylsiloxane elastomers exposed to partial electrical discharges, *J. Colloid Interface Sci.*, vol. 244, no. 1, pp.200–207, 2001.

[286] H. J. J. Verheijen and M. W. J. Prins, Contact Angles and Wetting Velocity Measured Electrically, *Review of Scientific Instrument*, Vol.70, No.9, 1999, pp.3668-3673.

Appendix A

FlexPDE 5 Programming Scripts

1. The distribution of electric field and electric potential in the absence of liquid

{Electric field simulation.}

TITLE 'Electric field'   { the problem identification }
COORDINATES cartesian2
VARIABLES
   U

DEFINITIONS
   um = 1e-6   {unit micron}
   d1 = 20 * um   {electrode width}
   d2 = 40 * um   {interelectrode width}
   L = 2 * d1   {free length}
   h = 20 * um   {channel depth}
   Uo = 20   {electrical potential, V}

   eps0 = 8.854e-12   {free space permittivity, Farad/m2}
   epsr
   eps = epsr * eps0

   E = grad(U)   {electric field}
   magE = magnitude(E)
   Ex = dx(U)   Ey = dy(U)

EQUATIONS
   div(eps*(-grad(U))) = 0{Laplace equation}

BOUNDARIES
 REGION "air"   epsr = 1
   start(0,-h/2)
   value(U) = 0   line to (d1,-h/2)
   natural(U) = 0 line to (d1+d2/2, -h/2)
   natural(U) = 0 line to (d1+d2/2, h/2)
   natural(U) = 0 line to (d1, h/2)
   value(U) = 0   line to (0, h/2)
   natural(U) = 0 line to (-L, h/2)
   value(U) = Uo line to (-L, -h/2)
   natural(U) = 0 line to close

PLOTS

```
        contour(U) as "Electrical potential"
        vector(E) as "Electrical field"
        contour(magE) painted as "Magnitude of electric field"
        contour(Ex) painted
        contour(Ey) painted


    END
```

2. The distribution of electric field and electric potential in the presence of liquid

```
    { Electric field simulation.}

    TITLE 'Electric field'     { the problem identification }
    COORDINATES cartesian2
    VARIABLES
        U

    DEFINITIONS
        um = 1e-6              {unit micron}
        d1 = 20 * um           {electrode width}
        d2 = 40 * um           {interelectrode width}
        L = 2 * d1             {free length}
        h = 20 * um            {channel depth}
        Uo = 20               {electrical potential, V}

        eps0 = 8.854e-12       {free space permittivity, Farad/m2}
        epsr                   {dielectric constant}
        eps = epsr * eps0      {permittivity}
        epsr_air = 1           {permittivity for air}
        epsr_liquid = 80.1     {permittivity for liquid}

        E = grad(U)            {electric field}
        magE = magnitude(E)
        Ex = dx(U)     Ey = dy(U)

    EQUATIONS
        div(eps*(-grad(U))) = 0{Laplace equation}

    BOUNDARIES
      REGION "air"    epsr = epsr_air
        start(0,-h/2)
        value(U) = 0   line to (d1,-h/2)
        natural(U) = 0 line to (d1+d2/2, -h/2)
        nobc(U)                line to (d1+d2/2, h/2)
        natural(U) = 0 line to (d1, h/2)
        value(U) = 0   line to (0, h/2)
```

```
        natural(U) = 0 line to (-L, h/2)
        value(U) = Uo line to (-L, -h/2)
        natural(U) = 0 line to close

   REGION "liquid"epsr = epsr_liquid
        start(0, -h/2)
        line to (-L, -h/2)
        line to (-L, h/2)
        line to (0, h/2)
        arc (radius = -2*L ) to close


    PLOTS
        contour(U) as "Electrical potential"
        vector(E) as "Electrical field"
        contour(magE) painted as "Magnitude of electric field"
        contour(Ex) painted
        contour(Ey) painted

    END
```

3. The distribution of electric field and electric potential of surface charges

```
    { Electric field simulation.}

    TITLE 'Electric field'     { the problem identification }
    COORDINATES cartesian2
    VARIABLES
        U                      {electrical potential}
        rho                    {free surface charge}

    DEFINITIONS
        ms = 1e-11             {milisecond}
        um = 1e-6              {unit micron}
        d1 = 20 * um           {electrode width}
        d2 = 40 * um           {interelectrode width}
        L = 2 * d1             {free length}
        h = 20 * um            {channel depth}
        Uo = 20                {electrical potential, V}

        eps0 = 8.854e-12       {free space permittivity, Farad/m}
        epsr                   {dielectric constant}
        eps = epsr * eps0      {permittivity}
        epsr_air = 1           {permittivity for air}
        epsr_liquid = 80.1     {permittivity for liquid}

        cond                   {conductivity}
```

```
    cond_air = 20e-15      {conductivity of air, S/m}
    cond_liquid = 5e-4     {conductivity of liquid, S/m}


    E = grad(U)            {electric field}
    magE = magnitude(E)

EQUATIONS
U:  div(cond*(-grad(U))) = -dt(rho)        {conservation of charge}
rho:        div(eps*(-grad(U))) = rho      {Gauss law}

BOUNDARIES
  REGION "air"    epsr = epsr_aircond = cond_air
    start(0,-h/2)
    value(U) = 0   line to (d1,-h/2)
    natural(U) = 0 line to (d1+d2/2, -h/2)
    nobc(U)                line to (d1+d2/2, h/2)
    natural(U) = 0 line to (d1, h/2)
    value(U) = 0   line to (0, h/2)
    natural(U) = 0 line to (-L, h/2)
    value(U) = Uo line to (-L, -h/2)
    natural(U) = 0 line to close

  REGION "liquid"epsr = epsr_liquid       cond = cond_liquid
    start "path" (0, -h/2)
    line to (-L, -h/2)
    line to (-L, h/2)
    line to (0, h/2)
    arc (radius = -2*L ) to close

TIME 0 TO 1*ms BY 0.1*ms

PLOTS
    FOR t = 0, 0.2*ms, 0.4*ms, 0.6*ms, 0.8*ms, 1*ms
    contour(U) as "Electrical potential"
    vector(E) as "Electrical field"
    contour(magE) painted as "Magnitude of electric field"
    vector(rho) painted
    elevation(rho) on "path"

END
```
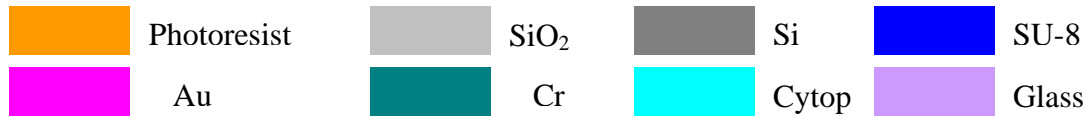
Appendix B

Fabrication Flow Process

1. Bottom Plate (Silicon) Fabrication

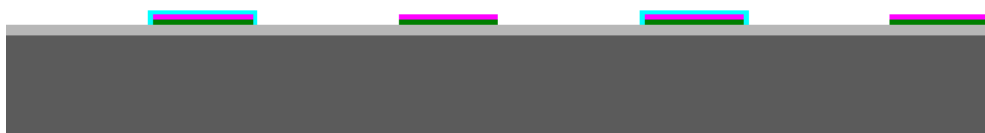|			
▮ Photoresist	▮ SiO$_2$	▮ Si	▮ SU-8
▮ Au	▮ Cr	▮ Cytop	▮ Glass

(a) Photoresist patterning

b) Chrome and gold sputtered-deposition

(c) Cr / Au lift-off

(d) Cytop coating and photoresist patterning for masking layer

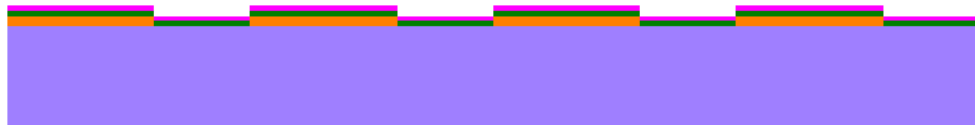(e) Plasma etching and photoresis stripping to form pattern dielectric layer

(f) SU-8 photoresist coating and patterning to form microchannel

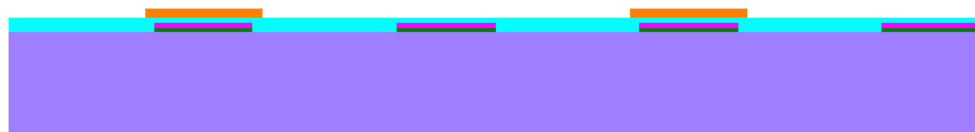## 2. Top Plate (Glass) Fabrication

(a) Photoresist patterning

(b) Chrome and gold sputtered-deposition

(c) Cr / Au lift-off

(d) Cytop coating and photoresist patterning for masking layer

(e) Plasma etching and photoresis stripping to form pattern dielectric layer